Retinal Layer Segmentation from Optical Coherence Tomography Images

A thesis submitted as partial fulfilment of the requirement of Doctor of Philosophy (Ph.D.)

Submitted by

Bashir Isa Dodo

Computer Science Department

Brunel University London

May 2020

Declaration

I, Bashir Isa Dodo, hereby declare I solely completed the work in this thesis. Some work in this report has been published previously, and that is stated in the text where relevant. Where I have consulted the works of others, the source of the materials have been properly acknowledged and references have been provided.

List of Publications Part of the work included in this research has been published earlier in the following articles:

1. Dodo, B.I., Li, Y., Eltayef, K. and Liu, X., 2018. Graph-Cut Segmentation of Retinal Layers from OCT Images. In BIOIMAGING (pp. 35-42).

2. Dodo, B.I., Li, Y. and Liu, X., 2017, June. Retinal OCT image segmentation using fuzzy histogram hyperbolization and continuous max-flow. In 2017 IEEE 30th International Symposium on Computer-Based Medical Systems (CBMS) (pp. 745-750). IEEE.

3. Dodo, B.I., Li, Y., Eltayef, K. and Liu, X., 2019. Automatic Annotation of Retinal Layers in Optical Coherence Tomography Images. Journal of medical systems, 43(12), p.336.

4. Dodo, B.I., Li, Y., Eltayef, K. and Liu, X., 2018, January. Min-Cut Segmentation of Retinal OCT Images. In International Joint Conference on Biomedical Engineering Systems and Technologies (pp. 86-99). Springer, Cham.

5. Dodo, B.; Li, Y.; Liu, X. and Dodo, M. (2019). Level Set Segmentation of Retinal OCT Images.In Proceedings of the 12th International Joint Conference on Biomedical Engineering Systems and Technologies - Volume 2: BIOIMAGING, ISBN 978-989-758-353-7, (pp 49-56).

6. Dodo, B.I., Li, Y., Tucker, A., Kaba, D. and Liu, X., 2019, June. Retinal oct segmentation using fuzzy region competition and level set methods. In 2019 IEEE 32nd International Symposium on Computer-Based Medical Systems (CBMS) (pp. 93-98). IEEE.

7. Dodo, B.I., Li, Y., Kaba, D. and Liu, X., 2019. Retinal Layer Segmentation in Optical Coherence Tomography Images. IEEE Access, 7, pp.152388-152398.

8. Dodo, B.I., Li, Y., Dodo, M.I. and Liu, X., 2019, February. Simultaneous Segmentation of Retinal OCT Images Using Level Set. In International Joint Conference on Biomedical Engineering Systems and Technologies (pp. 120-136). Springer, Cham.

The author has also made another publication during the PhD period, which is not included in this thesis.

1. Eltayef, K., Li, Y., Dodo, B.I. and Liu, X., 2017, October. Skin Cancer Detection in Dermoscopy Images Using Sub-Region Features. In International Symposium on Intelligent Data Analysis (pp. 75-86). Springer, Cham.

This thesis is dedicated to my late mother in-law, my parents, my wife and two sons.

Abstract

Three out of the four leading eye diseases affect the retina, causing irreversible blindness and various degrees of visual impairment. In the clinic, the effects of these diseases and other cardiovascular disorders are attributed to structural changes in the retinal structures. These changes are evaluated using various imaging techniques such as fundus imaging and optical coherence tomography (OCT). Consequently, the analysis of these images has become vital for diagnosing various ocular diseases in modern ophthalmology. Many computer-aided diagnostic (CAD) methods have been proposed to aid with the analysis due to the complexity of the retinal structures, the tediousness of manual segmentation and variation from different specialists. Besides, the commercially available systems focus on only a few layers of the retina, even though recent researches in the field of ophthalmology and neurology show that each layer might be affected individually. The reasons mentioned earlier urge for efficient intra-retinal layer segmentation methods. However, image artefacts such as speckle noise and inhomogeneity in pathological structures remain a challenge, with negative influence on the performance of segmentation algorithms.

This study investigates methods for image analysis, aiming to develop robust algorithms for segmenting retinal OCT images. Hence, this thesis presents four methods for extracting individual layer information from OCT to help with eye screening and management of various eye disorders, including glaucoma, diabetic retinopathy, age-related macular degeneration, among others. Distinctly, the first method is a comprehensive and fully automated method for annotation of retinal layers in OCT images, which comprises of fuzzy histogram hyperbolization for weight reassignment within adjacency matrices and graph-cut (shortest path) to segment seven (7) layers across eight (8) boundaries of the retina. Second, prior knowledge of the retinal architecture derived from the gradient information is embedded into the level set method to segment seven (7) layers of the retina. This method starts by establishing a region of interest (ROI), and then the refined gradient edges obtained from the ROI are used to initialise a level set function. Then, the understanding of layer topology is used in constraining the evolution process towards the actual layer boundaries.

Further, a third method capable of segmenting nine (9) retinal layers from OCT, that establishes a specific region of interest, similar to the previous method. Mainly, the method uses selected components from fuzzy C-Means clustering outcome to initialise a level set function. The clustering outcome from the initialisation stage is also used to guide the evolution of boundaries through a combination of Mumford-Shah (MS) selective region competition force and a Hamilton-Jacobi (HJ) balloon force. The method converges based on a HJ object indication function influenced by the fuzzy membership to prevent leakage at weak layer boundaries. Lastly, the fourth method is an efficient and computationally inexpensive method to segment five (5) retinal layers. The method also starts by establishing a specific ROI. Primarily, the method transforms the ROI, and then select components belonging to the hyperreflective layers to build data terms, which are integrated into a graph-cut continuous max-flow algorithm for optimisation. Promising experimental results were achieved, which demonstrates the tolerance and adaptability of the methods to contour variance and pathological inconsistency of the retinal structures. The use of prior knowledge of the OCT enables the methods to handle the incompleteness of OCT and reduce the likelihood of wrong segmentation, while the use of fuzzy image processing techniques aid in handling inhomogeneity.

Acknowledgements

All praise and gratitude are due to Allah (SWT) for extending my life and granting me good health to partake this research. Foremost, I would like to thank my supervisor, Dr Yongmin Li, for his advice, mentorship, unconditional support and encouragement throughout the PhD studies. Our discussions always gave me confidence in what I was doing, and his tolerance motivated me to keep on going amidst any challenge. I owe special thanks to Prof Xiaohui Liu, my second supervisor, for his encouraging comments and suggestions throughout this research. My profound gratitude to the examiners, Dr Miles Hansard and Dr Theodora Koulouri for their invaluable feedback on the initial theses, that has helped produced this final version.

My father, for his efforts and unending support. My mother, for her patience, advice, good upbringing, unceasing love and prayers. My wife and two sons, Bashir and Ahmad, for their unconditional love, patience and support when times were hard. My in-laws who have always supported my decisions in difficult times and their valuable advises. Also my little princess, fatima.

Special thanks to Dr Mona K Garvin for the permission to use images from her thesis, Umaru Musa Yar'adua University and Tertiary Education Trust fund (TETFUND) for sponsoring my PhD. My deep appreciation to the Computer Science Department for sponsoring all the conferences I attended during this research, and all the staffs of the department for their readiness to offer advice and support whenever the need arose. The Brunel student centre for financial support and the Brunel media services, especially, Tim Pilgrim and Joe Buchanunn, for helping with the dissemination of the research outcome.

I cannot end without thanking my colleagues in the Department of Computer Science whose support kept me going. In particular, Dr Djibril Kaba, Dr Chuang wan, Dr Khalid Eltayef, Dr Bilyaminu Auwal Romo, Najeeb A Gambo, Dr Izaz Rahman, whom I met at the beginning of my PhD and have assisted me in various capacities through discussion, sharing data and so on. Other colleagues whose discussions and advice have been instrumental to the progress of

this research including, Khalipha A Nuhu, Anas Alkasabeh, Nura Tijjani Abubakar, Mashael Al-Luhaybi, Weibo Liu and Shakirat Adesola amongst others.

Last but not the least, I thank family and friends for their support and understanding including Aminatu I. Dodo, Hadiza Muhammad Dodo, Hannatu I. Dodo, Ibrahim I. Dodo, Abbas Umar Masanawa, Fatima I. Dodo, Aisha I. Dodo Kamal Abdulsalam and all other family, friends and well-wishers not mentioned.

Contents

List of Figures

List of Tables

Acronyms

AMD Age-related Macular Degeneration

CAD Computer Aided Diagnosis

DB Diabetic Retinopathy

FHH Fuzzy Histogram Hyperbolization

GCL Ganglion Cell Layer

HJ Hamilton-Jacobi

ILM Internal Limiting Membrane

INL Inner Nuclear Layer

IPL Inner Plexiform Layer

IS Inner Segment

LSM Level Set Method

MAD Mean Absolute Deviation

MS Mumford-Shah

NFL Nerve Fibre Layer

OCT Optical Coherence Tomography

ONL Outer Nuclear Layer

OPL Outer Plexiform Layer

OS Outer Segment

RNFL Retinal Nerve Fibre Layer

RNFLT Retinal Nerve Fibre Layer Thickness

ROI Region of Interest

RPE Retinal Pigment Epithelium

RMSE Root Mean Squared Error

SD-OCT Spectral Domain Optical Coherence Tomography

TD-OCT Time Domain Optical Coherence Tomography

Chapter 1

Introduction

Medical images have an irrefutable role in health care by improving the process of diagnosing and treating a vast number of ailments. Notably, the field of ophthalmology has witnessed a revolution since the introduction of Optical Coherence Tomography (OCT) [77] imaging, which continues to make significant impact to date. This continuous impact of OCT is because the manifestation of major eye diseases is diagnosed and managed through the examination of retinal structures. Analysing these structures, which are acquired through various imaging techniques, such as fundus photography[1] and OCT, plays a significant role in the clinical eye examination. Mainly, retinal layer thicknesses provide useful diagnostic information that have been shown to correlate well with the measures of severity in several diseases, such as glaucoma, diabetic retinopathy, age-related macular degeneration and other cardiovascular disorders. Since manual segmentation of these layers is time-consuming and prone to bias, automatic segmentation methods are critical for full utilisation of the available technology [96]. For this reason, much research is carried out on retinal layer segmentation to help eye specialists in diagnosing and preventing the most common causes of vision loss in the developed world.

Furthermore, each layer might be affected differently by a disease. For example, a particular

[1] Photographing the back of the eye using specialised fundus cameras consisting of an intricate microscope attached to a flash enabled camera. The photography enables the visualisation of the retina, optic disk and macula.

layer may shrink as a result of neuron loss while another thickens as a result of oedema[2]. As such, it will be exemplary to be able to appraise the layer properties individually [53]. Thus, the urge and promising impact of retinal OCT segmentation methods are high, especially with the advancements in imaging techniques and the increase of image data availability to ophthalmologists. To appreciate the value of this research and its potential impact in monitoring eye diseases, it is important to understand the motivation behind retinal OCT analysis. Thus, an introduction to retinal layer analysis is provided in section 1.1. Section 1.2 highlights the aim and objectives of the research work, then followed by the contributions in Section 1.3. Finally, section 1.4 gives an overview of the thesis.

1.1 Retinal Layer Analysis

As stated earlier, it is essential to provide insight into retinal image analysis, to highlight the necessity of conducting this study. The four leading causes of blindness and visual impairment are cataract, diabetic retinopathy, glaucoma and Age-related Macular Degeneration (AMD). While cataract affects the front of the eye (clouding of the lens), the remaining three major eye-related diseases affect the retina and optic nerve head at the back of the eye. A notable difference between cataract and the other three eye diseases is that cataract is usually noticed by the patient early enough for adequate treatment, and the damages can be fully corrected with laser surgery successfully. While the early forms of AMD, glaucoma, and diabetic retinopathy are usually not noticed by the patient and gradually cause substantial damage to retinal tissues unless diagnosed early [54], which might lead to irreversible blindness. Also, a recent study shows the relation of the retina to the brain and how each layer is vital in the monitoring of ocular diseases [142], and occasionally an eye examination reveals a potentially life-threatening condition [2, 57, 101].

Furthermore, the amount of image generated by retinal imaging tools in ophthalmology is dramatically increasing, which overwhelms the ability of clinicians to evaluate diseases accurately. Additionally, manual image analysis by clinicians is time-consuming, cumbersome,

[2]Fluid retention at the macula due to leaky blood vessels in the eye.

prone to human error, and the results of the analysis are often dependent on the clinician's level of expertise. The main reason behind analysing these images is because early diagnosis and appropriate supervision of retinal diseases have been shown to prevent or curtail blindness [2, 20].

Moreover, a clinical non-invasive eye examination involves capturing images of the patient's retina with imaging tools, OCT in this case, and then using an automated image analysis algorithm to evaluate the images. The algorithm extracts retinal layers morphology from the images which provide vital information about the patient's eye condition. For example, the thickness of the central retina is an important marker for diagnosing diabetic macular oedema (DMO) [118], which is the most severe form of eye disease suffered by patients with diabetes. Also, structural changes in the retinal nerve fibre layer are essential for early diagnosis of glaucoma and monitoring treatment to prevent visual loss. Despite the evidence that early diagnosis and timely intervention reduces or prevents blindness, an increasing number of people with these diseases do not undergo any form of eye exam due to screening associated costs and the lack of more effective automated methods of diagnosis [122].

Therefore, there is an absolute necessity for reliable computerised techniques to aid in retinal image analysis. It is expected that these tools will improve the accuracy of results and reduce the time required for an eye examination. The automated methods can enable the use of teleophthalmology for screening and evaluating retinal diseases in remote areas globally [59]. Also, because eye screening and disease management can involve different processes, it is required that the methods be able to provide meaningful information for a variety of imaging tests. In brief, the urgency and potential impact of this thesis are high, with ever-increasing retina image data becoming available to clinicians to analyse.

1.2 Aim and Objectives

Retinal imaging technology has drastically evolved over the last few decades. This evolution is continuously making the tissues of the retina more visible to the specialists. Although the retinal tissues are visible on captured images of the retina, manually labelling the retinal layers

is time-consuming or even impossible. This has hindered the ability of ophthalmologists to efficiently distinguish minor changes to the retinal tissues, which is vital for diagnosis and timely intervention to prevent loss of vision.

As a result, many automated methods are proposed to aid ophthalmologists in extracting meaningful information regarding the diseases from retinal images. However, in applying these automated methods to actual retinal images, image artefacts pose challenges to the accurate delineation of the retinal structures. In particular, for OCT image analysis, intensity inhomogeneity, noise, and algorithmic complexity are the main stumbling blocks yet to be overcome by the automated retinal segmentation methods.

Consequently, this thesis aims to develop improved methods for robust segmentation of retinal layers from OCT images. These methods will enable the detection of retinal layer changes and extraction of useful information, which, in return, allow ophthalmologists to precisely diagnose diseases, especially in their early stages. The work proposed in this thesis is no way complete, but it presents the crucial knowledge in segmenting the retinal layers to enable the extensive use of retinal image analysis tools to everyday work in contemporary ophthalmology. The objectives of the PhD research can be summarised as follows:

1. **Developing fully automated retinal layer segmentation methods:** Develop plausible methods for extracting different intra-retinal layers from OCT macular images without the need for user initialisation, and evaluate performance of the methods using a dataset collected from Tongren Hospital, Beijing, China.

2. **Combining rigorously selected image processing techniques to improve performance of segmentation methods:** Thorough selection of image processing techniques by understanding the limitations of each method and handling those limitations for robust performance.

3. **Utilising prior knowledge of the retinal layers to improve segmentation accuracy:** Incorporate prior knowledge of the retinal structure into image segmentation frameworks to better model the segmentation problem.

4. **Improving homogeneity in retinal OCT image:** Propose an OCT enhancement technique to improve the homogeneity within individual layers using a mathematical image preprocessing technique.

5. **Preprocessing OCT images:** Establish a specific region of interest (ROI) containing only useful retinal layer information, by removing all other image background.

1.3 Thesis Contributions

In line with the aim and objectives of this thesis, it presents retinal layer segmentation methods by rigorously selecting and effectively combining image processing techniques that enable robust extraction of retinal layers from OCT images. Where appropriate, this study embeds prior works in image processing to inform the development of novel segmentation methods. More importantly, the highlights of the critical elements of the combination and what makes it appropriate for OCT segmentation are provided to guide further research in image analysis.

Prior knowledge of the retinal structure is incorporated into the graph cut and level set frameworks, to better model the segmentation problems. This improves the fidelity of the methods while considering the optimisability and time complexity. Embedding prior information into segmentation frameworks enables the methods to segment specific target features solely, which improves the accuracy and reliability of the results.

Furthermore, imaging artefacts such as intensity inhomogeneity and noise adversely affects the performance of segmentation methods. Hence, fuzzy histogram hyperbolisation is utilised to significantly suppress noise and handle intensity inhomogeneity to enhance the visibility of the retinal layers. This technique achieves the main aim of enhancing an image, which is to preserve image information (edges) without distorting or blurring the image as with the results seen with some mathematical image preprocessing techniques. The overall process allows for better segmentation of the target layers. It can also be used beyond OCT image preprocessing, as noise is prevalent in medical images.

Moreover, an OCT preprocessing technique has been developed to establish a specific ROI of interest containing the retinal layers solely, which ensures only the actual layer properties

affect the segmentation processes. This process is particularly useful as the convergence error rates are based entirely on the true retinal features. The contributions of this thesis can be summarised as follows:

1. This thesis has presented four innovative methods for reliable segmentation of retinal layers from OCT images.

2. Based on unique layer characteristics, the methods are designed to deal with inhomogeneity and incompleteness of the retinal layers.

3. An ideal OCT enhancement technique has been developed using fuzzy histogram hyperbolisation, which improves homogeneity and preserves image features.

4. A preprocessing technique to remove all image background, which promotes accurate segmentation of targeted layers.

From the contributions described in this thesis, the method to be described in chapter 3 has won the best student paper award, while the method in chapter 4 was a nominee for the best student paper award in the BIOIMAGING 2019 conference. As a whole, the research has won the best mature stage PhD in the Computer Science students PhD symposium held in 2018. Additionally, the contributions and potential impact of the research has been disseminated through conventional and social media media, including British Broadcasting Corporation and TVC News Nigeria to mention a few. Lastly, other online outreach mediums including Optometry Today, U.k and Punch news Nigeria, among others have published articles about the research contributions. Utilising these alternate dissemination mediums is to raise people's awareness of the prevalent eye diseases, which may improve the success of such technologies through awareness of the medical implications and research conducted towards curtailing major eye diseases.

1.4 Thesis Overview

This section provides a brief to each chapter within this thesis to visualise the overall structure. Each chapter is a full research work independently and taken together these chapters provide

an evolution of ideas that gradually manifest into a narrative of the use of computer-aided diagnosis in the current day eye examination. This thesis is composed of seven , and the remaining six (6) chapters are organised as follows:

- **Chapter 2** Revisits the literature to highlight background knowledge that is relevant to the scope of this research. Specifically, this chapter provides a brief introduction of the eye anatomy, including the anatomy of the retina. This is followed by a brief discussion of background and prevalence of the dominant eye diseases, including, glaucoma, age-related macular degeneration and diabetic retinopathy. Then it discusses the various imaging techniques used in acquiring images of the retina, and their values in diagnosing these diseases as a hint of the importance of OCT image segmentation and image analysis in general. Next, it elaborates on image segmentation algorithms, including methods utilised in this study. Finally, some major topics and challenges in OCT image analysis are discussed, which lays a background to serve as rationales for the contributions in the ensuing chapters of the thesis.

- **Chapter 3** presents a comprehensive and fully automatic method for annotation of retinal layers in OCT images, which is comprised of fuzzy histogram hyperbolisation for weight reassignment and graph cut methods to sequentially segment seven layers of the retina across eight boundaries. The method utilises the normalised vertical image gradient, and its inverse to represent image features in calculating two adjacency matrices. Because graph-cut methods depend on the assignment of appropriate weights, the method reassigns the weights to make edges along retinal boundaries have a low cost, which allows the method to identify the layer boundaries efficiently. Also, the method draws a vital point from the concept of perceptual grouping to improve the connectivity of edges within adjacent matrices, which contributes primarily to the success of the method. Part of this chapter has been presented at the BIOIMAGING 2018 [34], which has been published as an extended manuscript in the Communications in Computer and Information Science series [35]. Also, part of the chapter has been published as a journal article [36].

- **Chapter 4** presents a simultaneous method for segmenting retinal layers in OCT images

using a level set method. The method starts by establishing a specific region of interest as a preprocessing step to avoid the influence of background noise during the segmentation process. In the segmentation phase, prior knowledge of the retinal architecture is embedded into the level set method to segment seven layers of the retina. Specifically, refined edge information derived from smoothed gradient images is used as an initial curve for the layers, and the layering topology is used in constraining the evolution forces of the curves towards the actual layer boundaries. Part of this chapter has been presented at the BIOIMAGING 2019 [40] and [33]

- **Chapter 5** presents a robust method that is inspired by the concept of fuzzy region competition to segment nine layers of the retina. Similar to the method in chapter 4, this method establishes a specific region of interest. In contrast to chapter 4, this method use selected components from fuzzy C-Means (FCM) outcome to initialise a level set function. The clustering outcome is also used to guide the evolution through a combination of Mumford-Shah (MS) selective region competition force and a Hamilton-Jacobi (HJ) balloon force. The forces ensure evolution close to actual retinal boundaries. Finally, the convergence of the method is based on an improved HJ object indication function influenced by the fuzzy membership to prevent leakages at weak layer boundaries. Part of this chapter has been published in IEEE CBMS 2019 [39].

- **Chapter 6** presents a fully automated method for robust and simultaneous segmentation of five retinal layers from OCT images. Similar to the methods in chapters 4 and 5, it establishes a specific region of interest, for effective convergence and appropriate weight calculation. Notably, the method introduces an efficient and computationally inexpensive method by using fuzzy histogram hyperbolization for image enhancement technique. It then uses selected components from FCM belonging to the hyper-reflective layers to build data terms, which are effectively integrated into a continuous max-flow algorithm for segmentation. Additionally, this chapter contains performance evaluation of all the methods proposed in chapters 3,4,5 and 6 in segmenting the same five retinal layers while raising some challenges in comparing segmentation methods in general. This

chapter also unveils how other works in this thesis have streamlined to transform the first preliminary study of this research to the latest development. Part of this chapter has been published in IEEE CBMS 2017 [39], which was later extended to a journal article published in [38].

- **Chapter 7** presents an overview of the contributions of this thesis and how chapters 3 to 6 implement the individual objectives of the PhD project. Lastly, it provides concluding remarks concerning the proposed methods, including limitations and draws some potential dimensions for future work.

Chapter 2

Background

2.1 Introduction

Like most of the current research in computer science, this study brings together different fields including, image processing, image segmentation, ophthalmology, and data analysis to mention a few, all of which play essential roles in retinal OCT image analysis. The literature in each of these fields is vast and impossible to exhaust. Hence, this chapter reviews relevant works to provide insight into the literature to simplify the perspective from which this thesis addresses current challenges in retinal layer segmentation.

For easy visualisation of specific contents of this chapter, it is organised as follows. Section 2.2 introduces eye anatomy to understand the importance of vision and the retina. This is followed by a discussion of the major eye diseases in section 2.3, which is succeeded by a review of retinal imaging techniques in section 2.4. Section 2.5 discusses image segmentation algorithms by revisiting critical topics such as interactive and fully automated segmentation, use of prior knowledge and background of some of the methods used in this thesis. Lastly, reflections on retinal layer segmentation are reviewed in section 2.6, and then section 2.7 summarises the previous works and outlines the scope of this study.

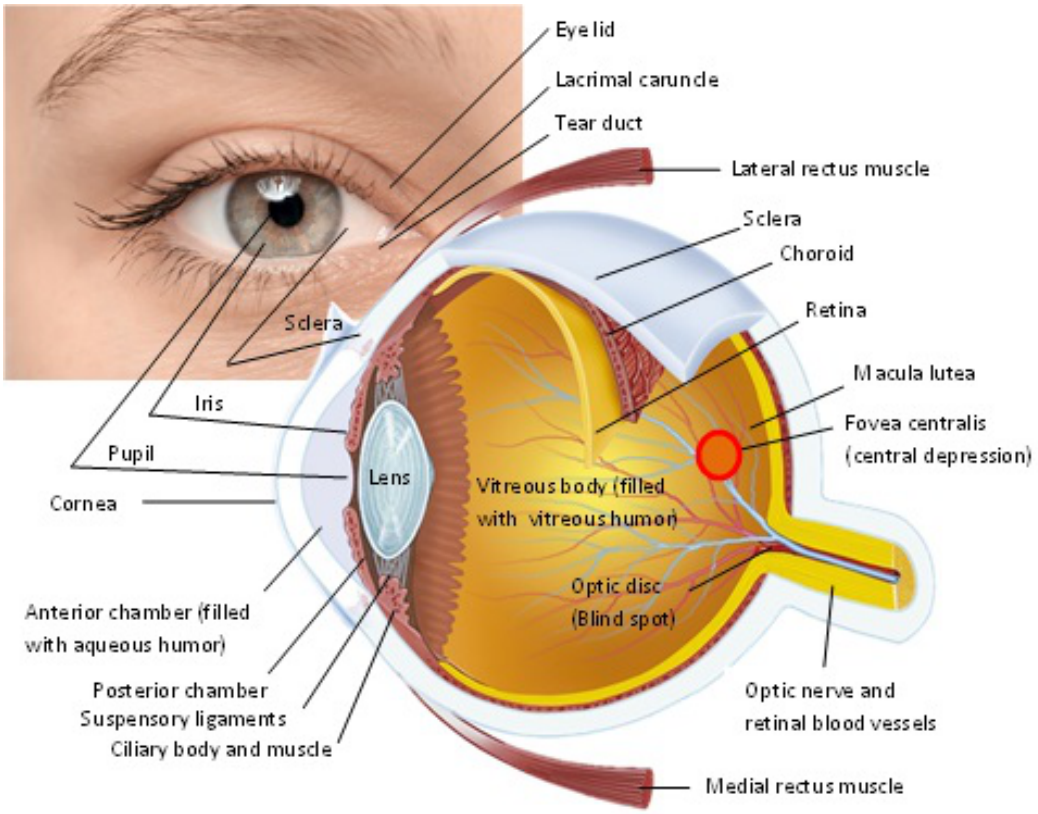

Figure 2.1: Schematic diagram of the cross-sectional view of the eye and its major structures (courtesy of [75]). The retina is the lining (indicated in yellow) at the back of the eye.

2.2 Eye Anatomy

The eye is a complex organ, and although it might be small, yet it provides the most vital of the five senses according to many people [71]. To be able to diagnose and monitor eye diseases, it is important to understand its structure and functions [123]. The eye operates similar to a camera, and Figure 2.1 shows a cross-sectional view of the eye and its significant structures that must work together to assure clear vision [75]. Distinctly looking at some of the structures, the sclera is the white part covering most of the eyeball, and It is a strong tissue that protects the eyeball. The coloured part of the eye, blue in figure 2.1, which can be brown, green, blue, or a mixture of these colours is called the Iris. The Iris surrounds and adjusts the size of the pupil to regulate incoming light into the eye. Over the Iris is a clear

dome referred to as the cornea, which transmits and focuses light onto the lens behind it. The curve of the cornea can indicate shortsightedness (myopia) or longsightedness (hypermetropia) as well as other visual impairments. Both myopia and hypermetropia can be easily corrected using concave and convex corrective laser surgery works, respectively [162]. The pupil is the black circular opening in the Iris through which light enters the eye.

Lying just behind the pupil and Iris is the lens, which functions similar to the lens of a camera by focusing light to the back of the eye. At the back of the eye is a lining made of specialised light-sensing cells collectively called the retina. Due to the relevance of retina in this study, it is discussed further in the next subsection 2.2.1. The retina contains photoreceptor cells that convert the incoming light into electrical impulses. The optic nerve transports these impulses to the brain, while the macula is an extra-sensitive area of the retina that is responsible for central vision. Last but not least is the choroid, which lies between the retina and the sclera and ensures oxygen and nourishments get to the retina. It also has a pigment that absorbs excess light to prevent the blurring of vision [71].

2.2.1 Anatomy of The Retina

The retina serves the same function as a film in a camera. As highlighted earlier, it is a light-sensitive layer that lines the inner part of the eye. It is composed of two sets of photoreceptor cells known as rods and cones. It is estimated that the retina contains about 125 million rods and about 6 to 7 million cones [71]. The rods are responsible for seeing in dim light, while the cones handle sharp, accurate light and colour.

When light is received, these photoreceptor cells convert the light into action potentials, which are transmitted to the ganglion cells by the bipolar neurons in the intermediate retinal layers. The optic nerve is formed by the axons of the ganglion cells that eventually exit the eye. Other cells in the retina that help in the processing of neural signal locally include horizontal and amacrine cells and interplexiform neurons. Also, support and structure in vision are additionally provided by neuroglial cells such as Muller cells [140] as illustrated by the light micrograph of the retina in figure 2.3. The retina is generally considered to have ten cellular layers [90, 140] as illustrated by the different views in figure 2.2. Taking the Berne et al. [90]

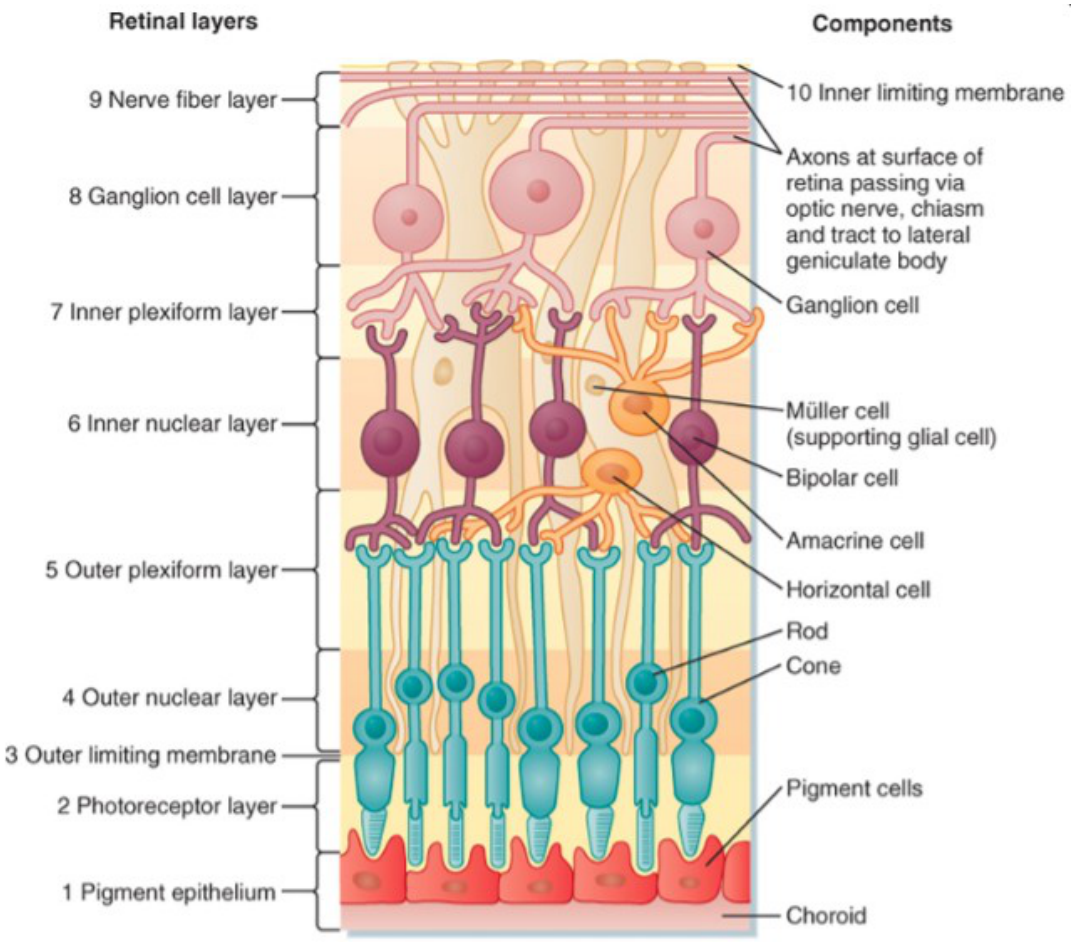

Figure 2.2: Illustration of ten layers of the retina (courtesy of [90]).

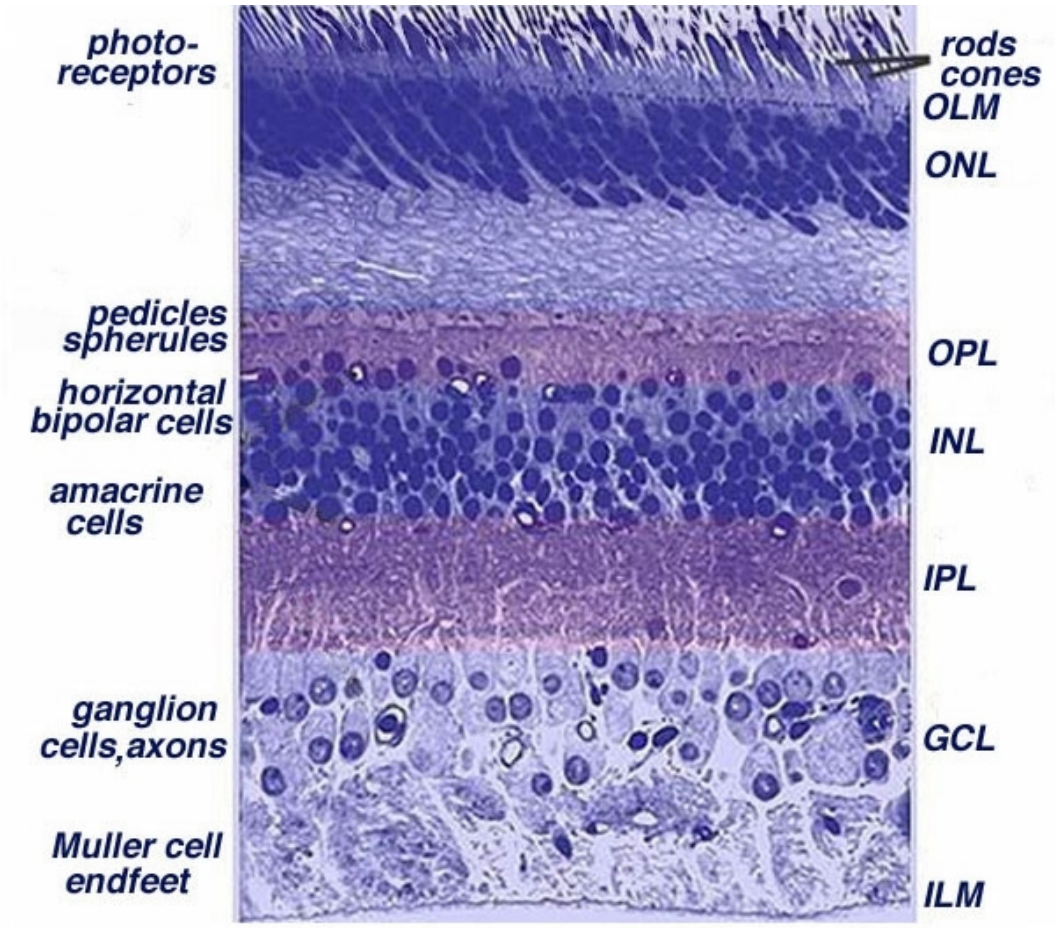

Figure 2.3: Light micrograph of a vertical section through central human retina (courtesy of [91]).

ordering, the layers are:

1. **The pigment epithelium (RPE):** a single layer of pigmented hexagonal cells that mainly serve to maintain image quality by absorbing the divergent light and preventing scatter.
2. **Photoreceptor layer:** the outer part contains the light-sensitive discs and the inner composed of photoreceptors, which receive light from a particular part of the visual field.
3. **The external (or outer) limiting membrane (ELM or OLM):** forms intercellular connections with the photoreceptors, Muller cells and photoreceptors, but not an actual membrane [53];
4. **The outer nuclear layer (ONL):** contains cell bodies of rods and cones;
5. **The outer plexiform layer (OPL):** formed of synapses between the photoreceptors and retinal horizontal and bipolar cells;
6. **The inner nuclear layer (INL):** made up of the nuclei, amacrine, bipolar, amacrine, and Muller cells and in addition to interplexiform neurons and misplaced ganglion cells.
7. **The inner plexiform layer (IPL):** the synaptic link between the ganglion cells dendrites and bipolar cells axons.
8. **The ganglion cell layer (GCL):** comprises mostly of ganglion cell bodies;
9. **The retinal nerve fibre layer (NFL):** formed mostly of axons of the ganglion cell axons.
10. **The inner limiting membrane (ILM):** it is the innermost membrane that separates the retina from the vitreous cortex.

The names of various cells can be noticed in the description of these retinal layers, which have specific jobs that help transmit incoming photons into action potentials that the brain's cortices process into vision. There are six different types of cells in the retina, which include [107]:

1. Rods
2. Cones
3. Retinal Ganglion cells
4. Bipolar cells
5. Horizontal cells
6. Amacrine cells

The number of cells within each layer is unknown, with the exception of rods and cones. Knowing the number of cells within each layer can allow for other segmentation methods, e.g. soft segmentation, to be utilised in OCT image segmentation with the aim of better understanding the changes caused by various diseases. Further details on the cells and their respective functions can be found in [107].

2.3 Major Retinal Diseases

Four eye diseases have become a threat to the vision of individuals in both developed and developing countries, i.e. cataract, glaucoma, age-related macular degeneration and diabetic retinopathy [172]. While cataract is the first cause of blindess and visual impairments, it affects the lens at the front of the eye; hence, it can be noticed early by the patient and also it can be reversed through surgery. The surgery for cataract is effective and can reverse the damage done by the disease. The three other diseases, namely glaucoma, diabetic retinopathy and age-related macular degeneration, affects the retina and cause gradual damage to the retina. A simulated view of patients with these diseases is shown in figure 2.4. These three diseases are discussed further in the next subsections to highlight the clinical motivation for analysing the retinal layers and why this thesis is motivated by the challenges posed by manual analysis of retinal layers.

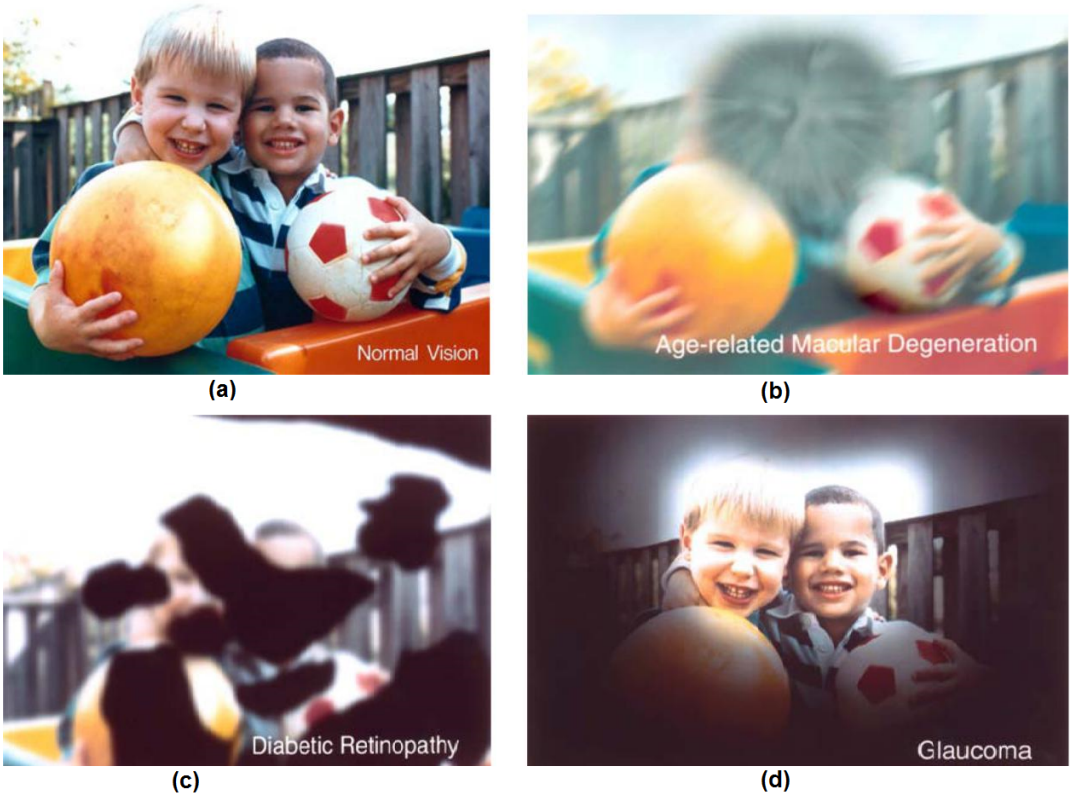

Figure 2.4: Simulated scenery view as may be perceived by patients with prevalent diseases. (a) Normal view. (b) View as perceived by patients with wet age-related macular degeneration. (c) View as percieved by patients with diabetic retinopathy. (d) View as percieved by patient with glaucoma.(courtesy of [53, 119, 120]).

2.3.1 Glaucoma

Glaucoma is the second major cause of permanent blindness. Recently, the concept and definitions of the disease have transformed from a single pathologic entity to a set of disorders with distinct clinical pictures [154]. These set of disorders damage the eye's optic nerve, which may lead to vision loss and or blindness [120]. To begin with, glaucoma does not usually cause noticeable symptoms. Instead, it develops gradually over time (usually years) and affects the edges of the peripheral vision at the early stage. Therefore, many people with the disease do not realise its presence. Consequently, this requires people having blurred vision, or seeing rainbow-coloured circles around bright lights to engage in routine tests because it is usually only detected with routine eye tests [74]. There are four main types of glaucoma: primary open-angle glaucoma, primary angle closure glaucoma, secondary glaucoma, developmental glaucoma (congenital glaucoma) [74].

Primary open-angle glaucoma - This is the most common type of glaucoma and develops very slowly [136]. It accounts for at least 90% of all glaucoma cases [47]

Angle-closure glaucoma - This is rare and can occur slowly (chronic) or may develop rapidly (acute) with a sudden, painful build-up of pressure in the eye. Although less common, people of Asian origin are more likely to develop this type of glaucoma in comparison to other ethnic groups [74, 120].

Secondary glaucoma - This occurs as a result of an eye injury or other eye condition. There are many forms of secondary glaucoma, for example, uveitic glaucoma, which results from the swelling and inflammation of the middle layer of the eye.

Developmental glaucoma (congenital glaucoma) -This is also a rare but severe type of glaucoma. It is usually present at birth or develops shortly after birth. An abnormality of incomplete development of the drainage canals in the eye during the prenatal period is the leading cause.

Furthermore, glaucoma often affects both eyes, although it may be worse in one. In England alone, about 480,000 people have chronic open-angle glaucoma. Among people of

European origin, the ratio of chronic open-angle glaucoma is about 1:50 and 1:10 for people over 40 and 75 years of age, respectively. Also, people of black-African or black-Caribbean origin are at higher risk of developing open-angle glaucoma.

The early detection and monitoring of glaucoma have been shown to reduce the risk of irreversible visual loss by glaucomatous damage [11, 69, 120]. Some common assessments for glaucoma include tonometry, perimetry, gonioscopy, and ophthalmoscope, among others. All these examinations manage glaucoma with Intraocular Pressure (IOP) lowering drops or through surgery in some refractory conditions. However, since the glaucomatous damage directly affects the structures of the retina, its damage can be assessed through structural analysis of the retinal tissues in an OCT image. This assessment can be done by direct measurement of the retinal RNFL thickness, which provides key structural changes of the RFNL by glaucomatous damage [2]. Further information about glaucoma can be found in [11, 136].

2.3.2 Age-related Macula Degeneration

Age-related macular degeneration is a progressive chronic disease of the central retina and a leading cause of vision loss worldwide [102]. This eye condition affects the macula, a small but critical area located at the centre of the retina and is responsible for clearly seeing fine details. AMD is a leading cause of visual impairment and blindness in adults aged 50 and over [49]. A patient with AMD loses the ability to see fine details, either close or distant. This affects only the central, and the peripheral (side) vision usually remains normal. For example, when people with AMD look at a clock, they can see the clock's outline but cannot tell what time it is; similarly, they gradually lose the ability to recognise people's faces [72].

The symptoms of AMD are the blurring of central vision, blind spots in the central field of vision and straight lines appear distorted or blurred. The symptoms and the deterioration of the retina occur more quickly in patients with wet AMD. Even though it remains unclear what causes AMD, age, diet, smoking, and family history are known to contribute. In the US only, over 11 million people live with AMD. AMD is the cause of vision loss to 54% of all blind people in America [49], and the risk of the AMD increases from 2% for adults ages (50-59)

to 30% for those over 75 of ages [121]. The cost of this chronic ocular disease is estimated at US343 billion globally, and its severity can reduce the possibility of employment by 61% and salary by over 39% [2]. There are two forms of AMD, which we briefly discuss in the following:

Dry AMD: refers to the early stage of AMD, and about 75% of patients have this form of AMD [72]. This is a form of AMD characterized by atrophy of the retinal pigment epithelium underlying the sensory retina, leading to the deterioration of the retina at the macula region. The dry AMD is the chronic and the slowly progressive form usually. A few among the patients with this disease progress to have late AMD.

Wet AMD: Also known as exudative AMD is the most typical type of late MAD representing the least cases of AMD but accounts for 90% of legal blindness. This form of AMD is characterised by ingrowth of abnormal blood vessels underneath the retina and at the final stages discoid fibrosis in the central part of the macula [4].In most cases of severe wet AMD, the patient is still able to see through the periphery of the retina. The late AMD caused by the thinning of the retina known as geographic atrophy can cause blindness through the loss of macular tissue without any bleeding of unhealthy blood vessels [72]. If Wet AMD is diagnosed too late and or left untreated, it rapidly progresses to cause major visual loss [54].

Furthermore, although dry AMD is by far the most common form, the wet type is responsible for most of severe visual impairment or blindness in AMD victims [181]. Both forms of AMD can be detected through a dilated eye exam, visual acuity test, and fundoscopy. While the dry AMD can be slowed through some dietary supplements [2], severe progress of wet AMD can be halted with intravitreal injections of anti-vascular (anti-VEGF) growth medicines [102].

2.3.3 Diabetic Retinopathy

Diabetes is a prolonged metabolic disease whereby blood sugar levels rise because the body produces a small inadequate amount of insulin, or the cells are unable to respond appropriately to it. In recent times, diabetes affects 387 million people globally, with an expected increase of 205 million by 2035, according to the International Diabetes Federation [63]. There are two

types of diabetes. In the first category, Type 1 diabetes, the immune system attacks the cells that produce insulin [7, 66]. Type 1 diabetes usually develops in children and young adults. Victims of this category need insulin injections daily to manage blood glucose levels, or the probability of death is high. The second category, Type 2 diabetes, accounts for 90% of cases [114]. The pancreas is unable to produce sufficient insulin to regulate blood glucose levels, or the body's cells are unable to react to it appropriately. Type 2 diabetes can occur at any age, but often, it is attributed to obesity. Because 8 out of 10 people who have had diabetes for 10 years or more have diabetic retinopathy [73], it is a significant concern for people with diabetes.

Moreover, diabetic retinopathy, i.e. damage to the retina, is a side effect of diabetes that gradually leads to blindness. In the first 2 decades of the disease, a vast majority of patients with Type 1 Diabetes and 60% of patients with Type 2 diabetes develop diabetic retinopathy [73]. The main symptoms of diabetic retinopathy are recurring blurred vision, double vision, difficulty reading, redness of the eye, shadows or veils across the field of vision and pain [114]. Excess blood-glucose as a result of diabetes cause damages to the blood vessels in the eye. This leads to two types of diabetic retinopathy, which are elaborated below [73]:

Diabetic macular oedema (DMO): In this type of DR, fluid leaks out from the damaged blood vessels into the back of the eye and accumulates in the macula. Eventually, this fluid causes the macula to swell, leading to blurred central vision, which affects patients ability to read or drive, but the vision to the side usually remains normal.

Proliferative diabetic retinopathy (PDR): In this type of DR, the retina is starved of blood due to the retinal blood vessels closing, which causes abnormal and highly vulnerable blood vessels to enlarge on the retinal surface. This leads to irreversible vision loss as a result of bleeding into the eye, retinal detachment, and retinal scarring.

Regular eye checks are necessary for all people with diabetes so that early signs of diabetic retinopathy can be detected to allow timely intervention. DMO might be treated with laser photocoagulation, which involves placing tiny laser burns in the area of retinal leakage, which slows the leakage of fluid and reduces the fluid in the eye. Although this process can help

stop vision from getting worse, it may not substantially improve vision for some patients. Other treatments are available and have been shown to benefit patients with DMO, including injections of anti-VEGF drugs such as bevacizumab and ranibizumab [73]. There is no direct cure for diabetic retinopathy, but laser surgery can reduce further damage, primarily if carried out before the retina is severely damaged. Also for PDR, surgical removal of the vitreous gel (vitrectomy) and anti- Vascular endothelial growth factor (VEGF) inactions or anti-inflammatory medications are effective in shrinking the new weakened blood vessels in the later proliferative stage.

The three eye diseases discussed above are usually managed by a combination of early diagnosis, medication, surgical treatment, and close follow-up [54]. More importantly, they are prevented through early diagnosis by non-invasive techniques [89, 101], as they cause irreversible blindness. These non-invasive techniques involve acquiring the images of the retina, and that is the discussion of the next subsection.

2.4 Retinal Imaging Techniques

The three eye diseases, i.e. glaucoma, age-related macular degeneration and diabetic retinopathy, mentioned in the previous section, are usually managed with a combination of early diagnosis, medical and surgical treatment, and close follow-up. There are various imaging modalities of the retina, including Magnetic Resonance Imaging (MRI) ultrasound, fundus photography, and optical coherence tomography (OCT). These imaging techniques allow the acquisition of anatomical structures of the retina in high resolution, with varying speed, resolution, strengths and weaknesses.

The field of ophthalmology was profoundly restructured in 1851 by Hermann von Helmholtz with the discovery of the ophthalmoscope because for the first time detailed diagnosis of the interior of the eye was made possible. Though ultrasound (stereo) biomicroscopy (UBM) can result in a subjective assessment of thickness differences of retinal structures, it is only with the emergence of scanning laser polarimetry, confocal Scanning laser ophthalmoscopy (SLO) and especially OCT, that objective measurements of the retinal structures thicknesses are now

clinically achievable [28]. More importantly, the evidence is now available that these objective measures are clinically relevant. We discuss two of the most relevant and essential imaging techniques below.

2.4.1 Fundus Photography (FP)

Fundus photography is an imaging technique that uses a specially designed camera to capture high-resolution colour images of the retina [138]. The fundus camera is set up with a low power microscope which provides a magnified view of the retina. Fundus images provide a 2-D representative image of the 3-D retina by using reflected light. The average width of the camera view ranges from 30 to 50 degrees, and the entire imaging process takes approximately 5 to 10 minutes [143]. The first fundus image was drawn by a Dutch ophthalmologist Van Trigt in 1853 [160] as shown in Figure 2.5. Fundus photography was invented in the 1920s and has been used widely since the 1960's [60], and remains one of the most widely used imaging tools in clinics.

Ophthalmologists use fundus images to diagnose various diseases that affect the eye, such as diabetic retinopathy and retinopathy of prematurity. Moreover, Nonmydriatic fundus photography (FP) has been a suboptimal tool for detecting age-related macular degeneration (AMD) changes [146]. Moreover, FP images are instrumental in diagnosing various diseases to support nonintrusive diagnosis in modern ophthalmology. This is because the morphology of the blood vessel and the optic disk are important indicators for eye diseases and other terminal illnesses, including hypertension [57, 144]. Additionally, fundus images are used to detect medical symptoms, such as haemorrhages exudates, cotton wool spots, and pigmentation.

2.4.2 Optical Coherence Tomography

Optical Coherence Tomography (OCT) imaging, also known as ultrasonography with light, is an emerging non-invasive optical imaging modality in biomedical optics and medicine. Since the introduction of OCT by Huang et al. in 1991 by [77], it has become increasingly used in the diagnosis and management of a variety of ocular diseases such as glaucoma, diabetic macular oedema, and age-related macular degeneration. It also allows the acquisition of morphologic

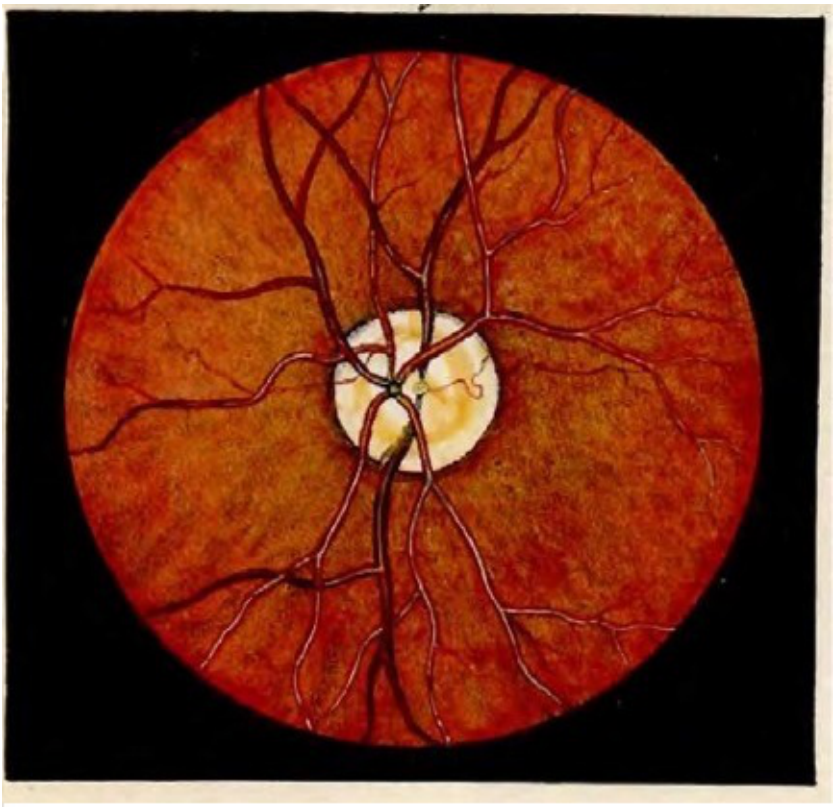

Figure 2.5: First human fundus photograph by Van Trigt in 1853 (courtesy of [160]).

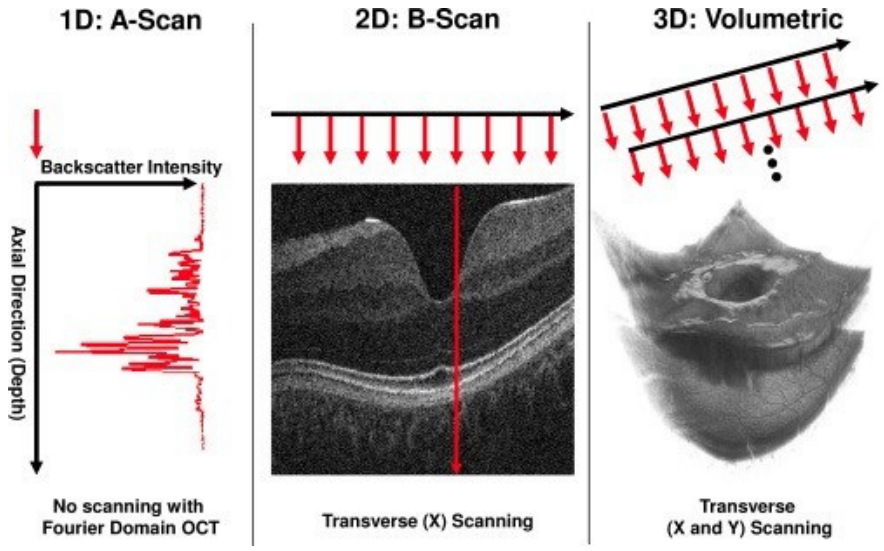

Figure 2.6: OCT scanner system schematic [95].From Left to right: A-scan. Backscattered intensity along the axial direction is measured and formed a single depth profile; B-scan. The OCT beam is measured in transverse direction; Volumetric image. Multiple B-scans are acquired and formed into a 3D volumetric image, respectively.

(anatomic) high-resolution cross-sectional views of the retina. From Left to right, figure 2.6 shows the type of information acquired using OCT:

Axial (A)-scan: An image obtained along the depth direction of the retina.

Brightness (B)-scan: The OCT beam is estimated in the transverse direction to form a 2D image.

3D-scan: A collection of B-scans in parallel.

The valuable information provided by the technology which enables quantitative thickness measurements of retinal structures is used in the identification of various disease states, determination of the cause of decreased vision and monitoring treatment. About a decade ago, all commercial systems were time-domain (TD) systems figure 2.7 (a). Now spectral-domain figure 2.7 (b), a type of OCT, which enables the acquisition of substantially more data, are also available. These two main types of OCT are briefly discussed in the next few subsections.

Figure 2.7: Example OCT scanner systems. (a) Stratus OCT-3 (time-domain system by Carl Zeiss Meditec, Inc., Dublin, CA). (b) Cirrus (spectral-domain system by Carl Zeiss Meditec, Inc., Dublin, CA). (courtesy of [53] with permission).

2.4.2.1 Time-Domain Optical Coherence Tomography (TD-OCT)

The Time domain Optical coherence tomography (TD-OCT) technique is commonly compared to the ultrasound due to the similarity of the two techniques. TD-OCT has around 10µm axial resolution, which is much higher than that of ultrasound at around 150µm. Generally, TD-OCT uses a backscattered echo time delay and light intensity levels to create a cross-sectional image. Also, TD-OCT is the earlier version of OCT. It uses a super-luminescent diode to direct low coherence light into the eye. The light beam is split into two parts by a beam splitter. One of the beams is directed into the eye and is reflected from the different layers of the retina, while a reference mirror reflects the other reference beam. As a result, a cross-sectional image or a B-scan, with a resolution of approximately 8-10 µm is captured by sequentially obtaining a series of A-scans [137]. A schematic illustration of the interferometry setup of TD-OCT is shown in figure 2.8. A typical TD-OCT image from a commercial scanner has a dimension of $6 \times 128 \times 1024$ pixels [53], although improvements have been made to the imaging technique. The two retinal regions routinely scanned are the macula and the peripapillary region (near the optic disc). Acquiring six linear radial scans in a "spoke pattern" centred at the fovea is one of the standard scanning protocol for acquiring macular scans (e.g., the Fast Macular protocol on the Stratus OCT-3). On the other hand, it is common to use several circular scans to acquire images surrounding the optic disc [53]. The Stratus OCT (Carl Zeiss Meditec

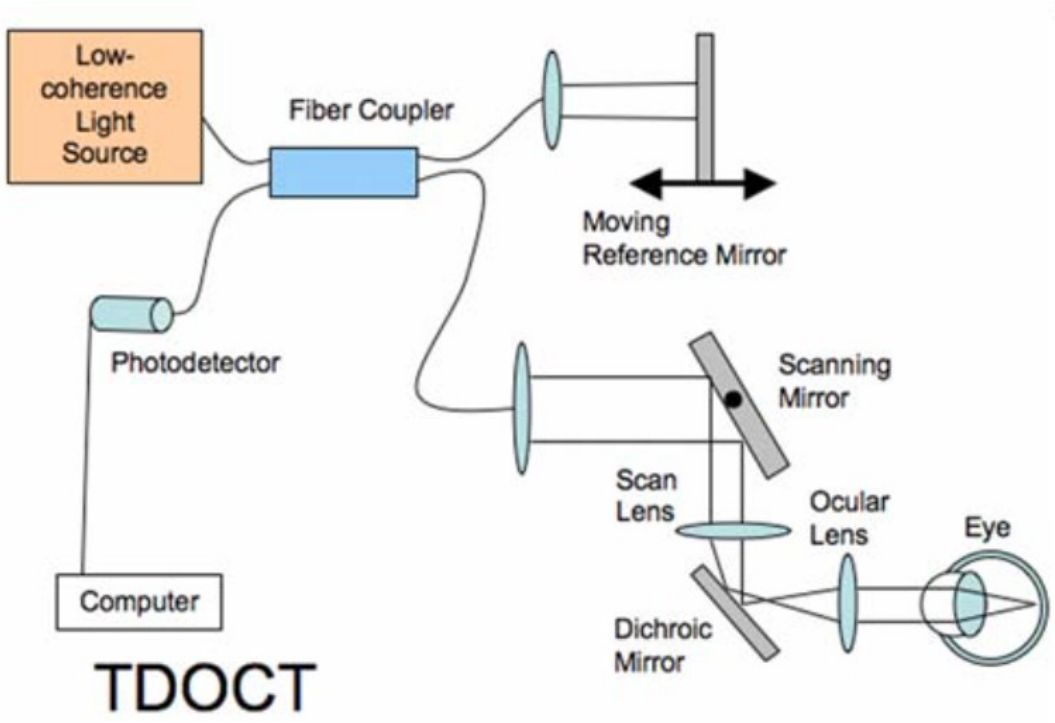

Figure 2.8: Schematic illustration of interferometry set-up in TD-OCT [147].

Inc., Dublin, CA, USA) figure 2.7 (a) is one of the most widely used TD-OCT devices in clinical applications, and it captures 400 A-scans per second with an axial resolution of 10 µm. TDOCT remains relevant in clinical practice. Clinics with SD-OCT device usually continue to use their TDOCT systems. The qualitative information and quantitative measurements of thickness changes over time obtained from TDOCT are reliable, which allows the provision of quality care for the majority of conditions regularly encountered by ophthalmologists [80].

2.4.2.2 Spectral-Domain Optical Coherence Tomography (SD-OCT)

Spectral Domain Optical Coherence Tomography (SD-OCT) is also referred to as the Fourier Domain OCT (FD-OCT) as its concept is based on fast Fourier transformation. It allows all reflections of light from the different retinal layers to be measured simultaneously, and the interference signal is a function of their wavelength. This eliminates the need for a moving reference mirror. The first retinal images with SD-OCT were reported in 2002, which became commercially available in 2006. The SD-OCT systems are approximately 40 to 110 times

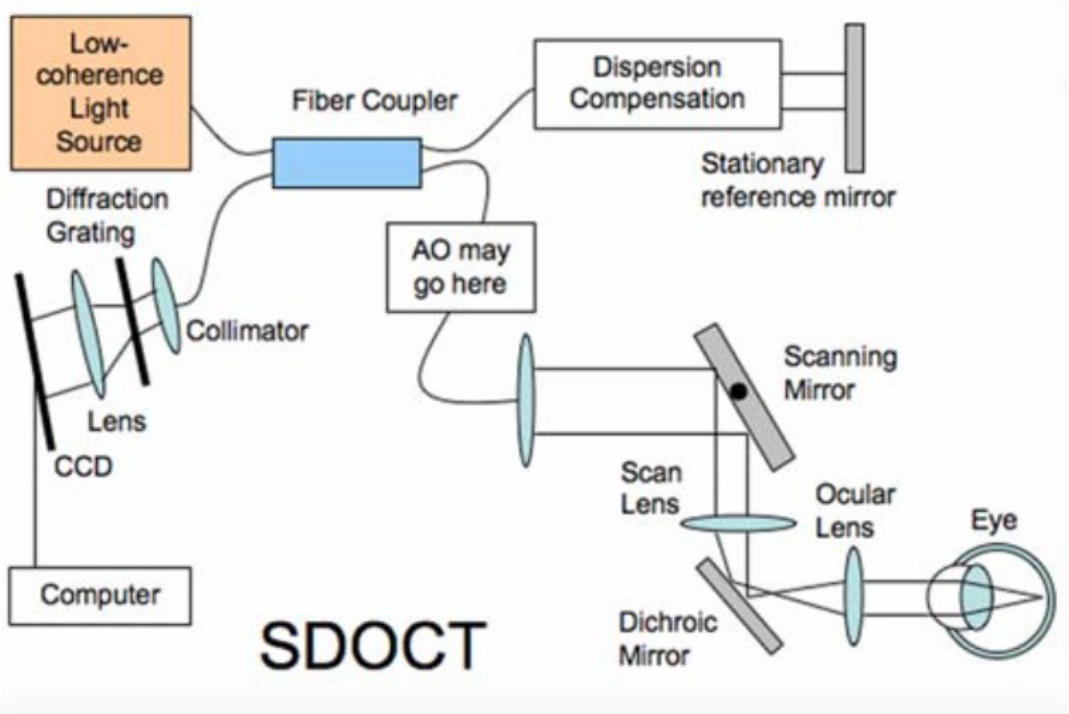

Figure 2.9: Schematic illustration of interferometry set-up in SD-OCT [147].

faster than TD-OCT systems [147] with an acquisition speed of about 25,000 A-scans per second having an axial image resolution of $\approx$ 5 to 7μm [80, 137]. Recent SD-OCT scanners can acquire up to 100,000 A-scans per second with an axial resolution of $\approx$ 3 to 5µm, a number which can increase to 250,000 A-scans per second with an axial resolution of 5 to 10µm [109].

Furthermore, although SD-OCT is fundamentally similar to TD-OCT, it has some significant variations. One of the main differences is that the reference mirror in SD-OCT is in a fixed position, unlike reference mirror adjustment in TD-OCT that is not efficient and limits both the speed and sensitivity of the scans. In SD-OCT specifically, the system acquires A-scans with a fixed reference path by measuring the spectral response of the interferometer [44]. It detects the interference between the sample and reference beams as a spectrum, and the interference pattern is split into its frequency components. Then all of these components are simultaneously detected via a charge-coupled device (CCD) camera. This CCD camera is sensitive to various frequencies. A schematic illustration of the interferometry setup of SD-OCT is shown is figure 2.9.

The enormous advantages of the SD-OCT imaging modalities are becoming apparent through research and experience, including faster image acquisition and improved resolution, which benefits both physicians and the patients [80]. Artefact from ocular movements has reduced significantly due to the improvements. The SD-OCT also overcome the TD-OCT in its ability to form better 3D maps of the retina and optic nerve [137]. However, it is noteworthy that image artefacts are present in all of the imaging modalities, which leads to misrepresentation of retinal structure thickness [80].

The ophthalmoscope and later the fundus camera remained the primary methods of ocular examination into the 1960s, while they are still standard tools with effectiveness and in use today, they are not without limitations, and both require trained users to operate and make diagnoses [31]. OCT is a relatively new technique that has dramatically advanced the understanding, diagnosis and management of ocular diseases. The introduction of spectral domain instruments has improved acquisition speeds and allows capturing high-resolution three-dimensional images of the retina. It can provide quantitative measurements of retinal structures with a high degree of reproducibility [137].

Moreover, fundus photography (FP) is like Google Earth, allowing the view of the wider picture, while OCT is like Google Street View, allowing the view of the fascinating and useful detail Gibson2015. OCT may have applications in other neurodegenerative conditions. Several groups have demonstrated RNFL thinning in Alzheimer's disease patients when compared with age-matched controls [137]. These changes occur early during the disease and correlate with the severity of cognitive impairment. Also, a significant reduction in inferotemporal peripapillary RNFL thickness in Parkinson's disease was demonstrated when compared with age-matched controls [79].

In summary, there are many imaging techniques to capture the anatomical details of the retina, which makes it possible to diagnose eye diseases and other ailments. However, due to difficulty, time and effort required, and in some cases impossibility of manual retinal image analysis, there is the need for computer-aided segmentation [55, 93, 149]. Also, although fundus is still widely used, this thesis focuses on analysing OCT images as they provide more details of the retina and enable the early diagnosis of the prevalent eye diseases.

2.5 Image Segmentation

The importance of image segmentation in technology cannot be overemphasised as it plays a crucial role in many medical imaging applications, by automating or facilitating the delineation of anatomical structures and other regions of interest [132]. Segmentation is a division of Computer Vision under Artificial intelligence that draws its principles from the concept of perceptual grouping. The concept of perceptual grouping dates back to nearly a century ago when it was proposed by Wertheimer [171], (first proposed in 1923 and this copy was made available online by [61]). This concept pointed out the importance of perceptual grouping and organisation in vision and mentioned several vital factors that influence the action, such as similarity, proximity, and good continuation of light level, which lead to visual grouping. The factors brought up by Wertheimer play a vital role in applications of vision [150]. We value these points because Computer Vision tends to map the function of the human brain. Therefore, like the majority of system or process automation, its main principles are derived and governed by the real-life situation. This makes the use of prior knowledge inevitable in image analysis techniques.

Segmentation is an image analysis technique, which in simple terms could mean a technique for partitioning or grouping an image into multiple regions with similar characteristics for better comprehension, organisation and visualisation. In computer science, there are basically three sets of operations that can be performed on a digital (binary, coloured, grayscale) image, i.e. Image Processing; Image Analysis; and Computer Vision [10]. While authors in [31] groups the operations into four based on function or usage, although this classification gives only subsections of the main classes considering that analysis and manipulation could fit into one class as analysis Operations in the main classification.

Starting with image processing, it is also called and usually used as a preprocessing step, and there are various techniques of performing such. It is a low-level operation carried out on images, with the primary goal of setting the image to a particular state and ready for further usage. Operations under this category include; image enhancement; noise removal; image restoration to mention a few. Image Analysis is the next in the hierarchy going from low to

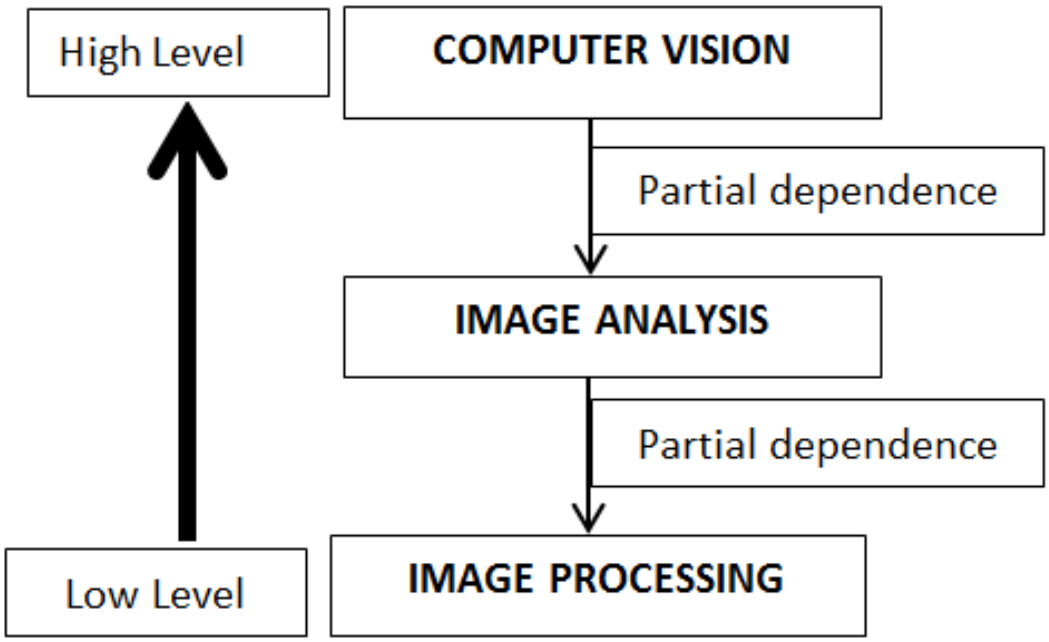

Figure 2.10: Classification and interdependence between digital image operations.

higher level operations. It has to do with obtaining/identification of features on the image, image segmentation, registration, and matching all fall under this category. The highest level and main goal of image processing is Computer Vision, aimed at extraction and visualisation of analysed features.

Notably, each category is independent. However, there is a partial dependency going from high to low operations, where lower operation serves as a preprocessing step for the higher in all cases. Hence image segmentation is sometimes (although confusing) also been referred to as a "preprocessing" technique [31, 177] if the problem at hand falls in Computer Vision category. Segmentation is also the most critical among the image processing techniques, and also the most challenging as it is considerably easier to quantify the performance of Computer Vision algorithms at recognition than at segmentation [110]. Figure 2.10 shows a summary of the classification and the direction of dependency among the various operations that can be performed on a digital image.

Consequently, mapping the dependence illustrated above (figure 2.10 to a real-life situation, it appears similar. For example, assuming a stormy or night scene (as it is not clear and poses

obstruction) is almost the same as an image corrupted by noise. This scenery usually requires some measures to be taken to clear the view or adapt to the situation, possibly by the use of glasses or night vision goggles. Accordingly, these measures in imaging terms are referred to as image processing techniques. Moving to segmentation, it is the most critical because that is where the decision of identifying boundary or grouping the scene in view into regions takes place. This grouping is done by identifying the boundaries of objects using the concept of perceptual grouping.

Furthermore, in some cases, knowledge about the scene or field of view assists in correctly grouping the scene and knowing where to navigate. This prior knowledge of the scene is similar to prior knowledge of the data that improves the performance of segmentation algorithms. Finally, Computer Vision has to do with classification and visualisation. If the boundaries have not been appropriately identified, it is apparent that the classification or recognition of the object will be unsuccessful as well. It is also to be noted that for image processing there is no universal approach for performing such, as strongly emphasised in literature and proven by experimental results to date, the technique that works on one set of data might fail on another (which leads to the discussion of the knowledge used in developing algorithms in chapter 2). Moreover, segmentation is about similarities and differences, continuity or discontinuity, as thus a point of classification from this higher (perceptual) perspective is relevant, thereby reducing the time taken to choose a technique for the problem at hand. As there is no universal algorithm for segmentation, narrowing down the options into a sub-category could enhance the efficiency and computational time for segmenting an image. The problem of segmenting two boundaries (i.e. background and foreground) is a minor and straight forward problem; most of the current researches are focused on multiple regions or objects. The low-level segmentation algorithms can handle the two region problem easily and faster, except it is to be noted they are susceptible to noise.

Image segmentation algorithms also referred to as segmentation algorithms or techniques are step by step ways or procedures of grouping or clustering an image into various regions with similar characteristics [50, 65, 177]. Haralick [65] raised some of the issues on what the representation of a good segmentation algorithm should entail, which includes the following.

1. Uniformity and homogeneity concerning grayscale or texture. 2. Region interiors should be simple and without many small holes. 3. Adjacent regions of segmentation should have significantly different values to the characteristic on which they are uniform. 4. Boundaries of each segment should be simple, not ragged, and must be spatially accurate.

Segmentation algorithms are broadly categorised into three [10, 50] based on the level of information at which they operate (i.e. Pixel-based methods; edge Based Methods; and Region-Based Methods), and into five as in [177]. The basic idea and some views on the low-level methods are given below, with more emphases on the medium and high (edge and region) methods, respectively. More emphasis is given to these two as most of the current researches are based on these methods. Hence they present more opportunities for further research.

We briefly revisit these three categories of image segmentation methods to highlight some of the useful concepts we have taken from the mechanisms of these methods that were relevant to this thesis. Additionally, this overview will also lay emphasis on how some of the previous methods were based on the idea of similarity and differences, i.e. perceptual grouping, which is among the primary basis of this research.

2.5.1 Pixel Based Methods

The low-level segmentation methods or techniques are called the pixel or threshold based methods or data clustering algorithms [50, 169]; they are relatively automatic by nature. In these techniques, one inserts the image and let the algorithm perform the computation (segmentation/analysis) based on a threshold set by the user. These algorithms are simple and straight forward in implementation, with almost no opening for users to discontinue or manipulate once it starts. Some slight exceptions might be the threshold that the user could set or the number of clusters in the case of clustering algorithms. K-means or fuzzy C-means (FCM) [87] algorithms may require a bit more knowledge of the data.

A significant difference between the methods is that K-means provides a specific result with the number of clusters and centroids produced, whereas C-means gives a probabilistic result. For clear bimodal (binary images) these techniques can be considered the best, as

they are strictly binary, keeping in mind the result of segmentation itself is binary (i.e. the foreground or the background). However, they are susceptible to noise and could only be handy with images that have apparent differences in intensity or gradient between the object and the background. Some techniques like binary masking and labelling are also used as additional constraints or final constraints step in higher methods of segmentation, and also useful in obtaining the ROI.

Consequently, in our methods, we have utilised the Fuzzy C-Means as it only offers probability. Additionally, that is why the gradient information utilised in controlling the outcomes of the Fuzzy C-means in chapters 5 and 6 is essential.

2.5.2 Edge Based Methods

As one of our approaches the higher level methods, the automation gets slightly more difficult due to the constraints to be set and the idea behind the techniques. Edge detection is an image segmentation technique based on the detection of discontinuity. An edge or boundary is the place where there is a more or less sharp change in image property [50]. The active contour started with the use of deformable models for image segmentation [85] while [128] introduced the level set Level-sets and it was made accessible for computer vision and image analysis by [108]. Level set methods are based on PDE, and image segmentation as a whole is an issue of differentiation, as thus there is some logical agreement between the two. The introduction of the PDE idea to segment images might have been highly influenced by knowledge of the data or image in place.

2.5.3 REGION BASED METHODS

2.5.3.1 Region Growing

The seeded region growing algorithm, proposed by [3] is a simple and computationally inexpensive technique for interactive segmentation of images in which the relevant regions are characterised by coherent pixels based on some predefined patterns (e.g. intensity and colour etc.) [112][10]. Region growing takes advantage of an important fact that the pixels close

together to have comparable grayscale values.

The main idea of this approach consists in the observation that the pixels belonging to one element of the object can possess similar properties. It does not have any statistical, optimisation or probabilistic mathematical foundation. With no inclusion of the global picture and suffers from other limitations. However, it has gained popularity due to its speed and simplicity of implementation. The primary drawback of the region growing approach is that it requires manual interaction to obtain the seed point [132].

This understanding of region growing has influenced our study because mainly it capitalises on the idea of differences across regions and similarity within each region. Further studies will consider region growing techniques due to the understanding of the retinal architecture, as the layering topology can be used to prevent leaks in the method.

2.5.3.2 Region Split and Merge

The split method for segmentation begins with the entire image as the initial segment. Then it successively splits each current segment into parts if the segment is not homogeneous sufficiently. Homogeneity can be easily established by determining if the difference between the largest and smallest grayscale intensities is small enough. Robertson [141] first suggested algorithms of this type and one of the disadvantages of the region merging processes is their inherently sequential nature [86]. The regions produced depend on the order in which regions merge. Almost all the region extraction algorithms use local information profoundly. There is no simple way to incorporate global information into the model unless by rigorously restricting the collection of images we are dealing with. All of the region extraction techniques iteratively process the pictures and usually involve a high expenditure in computation time and memory.

2.5.4 Incorporation Prior knowledge for Objective Image Segmentation

This section provides insight into the use of prior knowledge in improving the performance of image segmentation algorithms. It also raises some challenges associated with incorporating the prior knowledge into these algorithms.

2.5.4.1 Prior Knowledge

The use of prior knowledge enables the full automation of algorithms, to characterise the desired object and obtain beneficial results. For example, Stephanie et al. [27] were able to fully automate the segmentation of retinal layers by adding two columns to either side of the image. This automation is from the understanding that retinal layers span the image vertically, and that minimum cut approaches prefer minimum weighted paths. Also, Liu et al. [103] were able to constrain the level set method to preserve the layering topology in OCT, based on the understanding that retinal layers do not fall on one another.

There are many forms of prior information, including appearance prior, boundary information, shape models and topology, to mention a few. Appearance is one of the essential visual cues to differentiate various structures in an image, which is portrayed by studying the distribution of different features such as intensity values, colour, and texture within each object [125]. In OCT, some image traits worth considering in this direction were raised in [54], which highlights even though the thickness is an essential property of retinal layers, other properties may be useful as well. For example, the thickness values of each layer and (or) group of layers, and the average and variance of individual layer normalised intensity. Also, Haralick [65] highlighted computing variety of other traditional texture-based properties, including variance and the co-occurrence matrix feature, might be useful.

2.5.4.2 Interactive and Automatic Segmentation Techniques

Incorporating user input into a segmentation is instinctive and easy [125]. However, for most images, it is quite challenging to use completely automated segmentation approaches. Most notably, in the case of natural images and images with an unclear region of interest, such as OCT, it requires a high level of accuracy to accomplish, and interactive segmentation might be inevitable [177]. In contrast, interactive segmentation is very different from automatic segmentation to warrant a distinct approach to its evaluation. The most crucial difference between automatic and interactive segmentation algorithms is, of course, that interactive segmentation algorithms require a human operator. The interactions provided by this operator usually have a pronounced effect on the resulting segmentation: good mark-up is usually

needed to find a proper segmentation. Clearly, this is to be expected if the interactions did not have such a profound effect on the result, they could be provided automatically [112], thus eliminating the need for human supervision. The automatic segmentation algorithms are not given much priority, and most impact is given to the interactive. Hence, interactive algorithms are more efficient, as they have more practical applications. From what we observe, this is influenced by the prior knowledge held on the data.

Furthermore, the automation of the segmentation algorithms become more difficult going from the low level to the higher level segmentation methods. Taking a broader perspective of the applications of image segmentation, there is a natural transition from automated to interactive approaches, with the medium level methods usually been semi-automated. This transition is as a result of the increase in problems to be solved within the image and a better understanding of the image data. Thus, most of the recent researches are focused on optimization. Since manual segmentation of retinal layers is time-consuming and prone to bias, automatic segmentation methods are critical for full utilization of this technology [96]. While they are beneficial in most cases, limited or no attention is given to automation and simultaneousness of algorithms.

Given that computational time is an issue for some of the algorithms, exploiting the capability of GPU programming in addition to these factors will yield a better result, both in terms of efficiency and computational time. A study by [130] includes a wide range of graph cut approaches, concluding that the automatic and interactive methods were evaluated individually with approaches of its kind (automatic or interactive approaches). It also includes an experimental evaluation of segmentation algorithms based on graph theoretical approaches.

Lastly, if the ophthalmologists could estimate the size of the retina to a certain level, this will help model segmentation algorithms. This knowledge will not only help and make the work more accessible but also open up new avenues for research in image segmentation. For example, if the size of the retina is specific, region limitation can easily be applied with a high level of confidence. Also, this could help in analysing if specific sizes of the retina mark some diseases or not. These all can be incorporated to solve various issues of segmentation and evaluation of retinal images. In this thesis, we utilise intensity distribution, shape prior and topology of the

retinal in OCT images. More importantly, we show how mathematical models can be used to incorporate the prior knowledge in fully automated image segmentation algorithms efficiently. Due to the broad nature of segmentation, this thesis focuses on automatic segmentation of retinal OCT B-scan images.

2.5.5 Graph Based Methods

Graph-Cut is an optimization method used in solving many image processing and Computer Vision problems, as first reported by [148], where the problem is represented as a graph. A graph G is a pair (ν, ε) consisting of a vertex set ν (referred to as nodes in 2D or Vertex in 3D nested grid) and an edge set $\varepsilon \subset \nu \times \nu$. There are two main terminal vertices, the source s and the sink t. The edge set comprises of two type of edges: the spatial edges $e_n = (r, q)$, where $r, q \in \nu \backslash \{\text{s , t}\}$, stick to the given grid and link two neighbour grid nodes r and q except s and t; the terminal edges or data edges, i.e. $e_s = (s, r)$ or $e_t = (r, t)$, where $r \in \nu \backslash \{\text{s , t}\}$, link the specified terminal s or t to each grid node p respectively. Each edge is assigned a cost $C(e)$, assuming all are non-negative i.e. $C(e) \geq 0$. A cut partitions the image into two disjoint sets of s and t, also termed the $s - t$ cut. The cut divides the spatial grid nodes of Ω into disjoint groups, whereby one belongs to source and the other belongs to the sink, such that

$$\nu = \nu_s \bigcup \nu_t, \quad \nu_s \bigcap \nu_t = \emptyset \tag{2.1}$$

We then introduce the concept of max-flow/min-cut[46], which aims to find a flow f of the maximum value in a graph (flow network) G with source s and sink t, which can alternatively be viewed as finding a minimum cut in the flow network. This comparison is because of the max-flow min-cut theorem, which states that 'the value of the maximum flow is equal to the capacity of the minimum cut'. Distinctly, the max-flow computes the maximal flow allowed to pass from the source s to the sink t and is formulated by

$$\max_{p_s} \sum_{v \in \nu \backslash \{s,t\}} p_s(v) \tag{2.2}$$

on the other hand, for each cut, the energy is defined as the sum of the costs $C(e)$ of each edge $e \in \varepsilon_{st} \subset \varepsilon$, where its two end points belong to two different partitions. Hence the problem of min-cut is to find two partitions of vertices such that the corresponding cut-energy is minimal,

$$\min_{\varepsilon_{st} \subset \varepsilon} \sum_{e \in \varepsilon_{st}} C(e) \tag{2.3}$$

The equivalence of max-flow to min-cut can be easily understood whereby if the edges on the min-cut are removed from the graph, there will be no path from s to t, likewise, if the saturated edges of the max-flow are removed from the graph no flow with reach the sink from the source. The graph-based methods in image segmentation are focused mainly on optimisation based on network flow or pattern recognition. There are many graph-based methods, although there are two dominant methods:

Shortest-path: The shortest path algorithm seeks to find the minimum number of edges from source to sink within a graph [30]. Dijkstra's algorithm [32] is among the popular shortest path based algorithms. The algorithm is optimal from its background, as it is an extension of the breadth-first search (BFS) (that works on unweighted graphs). Dijkstra's algorithm extends the BFS to enable it to work on weighted graphs. However, the algorithm works on graphs with positive weights only and cannot perform on graphs with negative weights. Thus, the Bellman-Ford algorithm was proposed, which handles the negative weights. Dijkstra's algorithm is faster than the bellman-ford algorithm [30], although it is not clear which one is better, as each of them is optimal in solving the problem it tends to handle, just that one has a more considerable scope than the other. The technical background of this approach is discussed in chapter 3, which utilises the concept of the approach.

Max-flow and min-cut: is the dominant of the two main graph-based approaches. There are two main methods for finding the max-flow, namely the augmenting paths [46] and push-relabel [58]. The difference between the two categories is that the first method searches for a path where it can send a positive weight, such that it saturates at least one edge on the path. It repeats the procedure until no augmenting path can be found

in the graph from source to sink. Also, the outflow from a node cannot exceed the inflow into the node. In the push-relabel method, a pre-flow to find shortest paths between nodes from source to sink it repeats the process until no path can be found from source to sink and in this case, the outflow can exceed inflow. The technical background of max-flow/min-cut is further discussed in chapter 6, which utilises the concept.

Graph cut was first introduced to Computer Vision by [148], to minimise the maximum cut, by reducing the maximum flow between the small segments (sub-graph) for binary image restoration. The algorithm had a problem of voxel isolation as it was a local optimisation approach and did not have a global picture. It was then extended in 2000 by [150] with the normalised cuts, this attempt to solve the problem of voxel isolation in the previous work, which it did, however, it also did not have a global image in its approach. This was then further extended and optimised by [16], since its introduction it has gained high acceptance and applicability in various medical imaging applications. Following certain conditions, a cut on a graph can be perceived as a hypersurface in N-D space enclosing the corresponding graph [15]. As it is a matter of energy optimisation, it is also vital to know the type of constraints to set. The region of interest and data structure should, therefore, determine the constraints set in an algorithm to perform on. The pattern on which the algorithm follows in segmenting an image is accordingly essential. Graph cut methods are further discussed in chapters 3 and 6 utilising variants of the method. Graph-Cut has been an active area of research since its introduction to image processing, in particular some popular methods utilising its concept includes [16, 92, 179].

2.5.6 Conclusion on Image Segmentation

It is important to note that the same algorithms are used in other aspects of image operations, some using the same constraints while it varies slightly in others. Taking the graph cut method as an example to clarify and justify the point made earlier herein, it has been used in image segmentation [16], image restoration [148], computing stereo [17, 18] and in object reconstruction. The graph cut constraints imposed on edges is proof of optimisation. With single objects or problem, most algorithms perform well, taking the region growing, level

sets, active contours, selecting a seed will obtain the desired object; however, they have been applied to solve multiple region problems, and they have performed well. The main addition or difficulties have been handled by recent researches tend to stabilise or improve how they handle the issue of multiple regions or objects and speckle noise even though that is reducing with improvement in imaging technology. As some layers are obtained simultaneously, what is the possibility of obtaining all layers simultaneously? Keeping in mind that $w(i, j)$ is different from $w(j, i)$. This, in turn, is similar to the idea of thresholdingi.e. instead of setting the threshold as I ≥ 0, it can be in the reverse case of setting the threshold as I ≤ 0. This is important to highlight however beyond the scope of this thesis, considering the vast research carried on The split and merge are thus some worth related to the k-means in their approach as they both work on intensities. Split and merge, active contour, level sets, are better for models and shapes segmentation. The graph cut was introduced to Computer vision almost about the same time as the active contour.

2.6 Retinal Layers Segmentation

There have been numerous attempts to segment the various layers of the retina, each attempt with varying level of success and efficiency. Existing methods in the literature focus on the number of layers segmented, accuracy, constraints, and others on optimization. The various methods, challenges and success of previous segmentation methods for retinal OCT analysis are briefly discussed in the next few paragraphs. To start with, Koozekanani [93] developed a 1-D edge detection algorithm using a Markov boundary model, but the algorithm was prone to error due to speckle noise. The filtering algorithm was unable to denoise the image properly, and also introduced its own errors by erasing small image features and blurring others. Boyer et al. [14] later extended this to obtain the optic nerve head and RNFL. Baroni et al. [9] developed a multi-step approach for quantifying structural changes in the retina by a combination of edge search at different (High and Low) intensities and use of prior knowledge. However, the results were highly dependent on the image quality and the variations caused by retinal pathologies.

Moreover, the peak search approach was used to obtain 3 retinal layers by Shahidi et

al. [149], in which the algorithm searched peaks corresponding to high and low intensities. Likewise, Cabrera [21] segmented 7 layers using peak search interactive boundary detection based on local coherence of the retinal structure. Also, the active contour approach is an avenue explored by [116] to obtain the RNFL thickness, were a method based on anisotropic noise suppression deformable splines was developed. However, the algorithm was prone to leaking in boundaries, and the anisotropic filter did not thoroughly smooth the images. The level set method has been used for retinal OCT image analysis [55, 64, 126, 170, 182], which have reported successful results. However, computational time and leakage is the main challenge of these methods.

Not only in humans, Yazadapanah et al. [174] proposed a method to segment five intra-retinal layers in OCT images from 4 rats by adopting the Chan-Vese energy-minimizing active contours without edges. However, despite the algorithm's ability to handle the noise, it has quite a costly computational time, due to the set of constraints it operates. As well, seven retinal layers of a rodent were segmented by [115] using a method that employs an external force derived from the image gradient through an adaptive vector-valued kernel function. The algorithm was aimed at addressing the issue of sensitivity to speckle noise in previous approaches. However, due to the variance in the anatomical structure of human and rodents retina, it is quite difficult to rate its robustness directly compared to other approaches, even though speckle noise is a major issue faced by all segmentation algorithms and these algorithms present a way of handling the leak in active contour.

On other notes, segmentation of other features of the retina for diagnosis also exists, such as the segmentation of the blood vessels from the optic disc [25, 42, 48, 76, 97, 144], identifying fluid-filled regions of the retina [45, 135], and the Optic Nerve Head [14]. While segmenting these features are still important alternative measures for the diagnosis of the aforementioned ocular diseases, they are beyond the scope of the discussion of this thesis. Also the same algorithms but bounded and influenced by different constraints and prior knowledge as in [14] or the same parameters as in [116]. For this reason, previous works in segmenting retinal layers are discussed in chapters 4 to 6 to outline relevant works to the individual chapters.

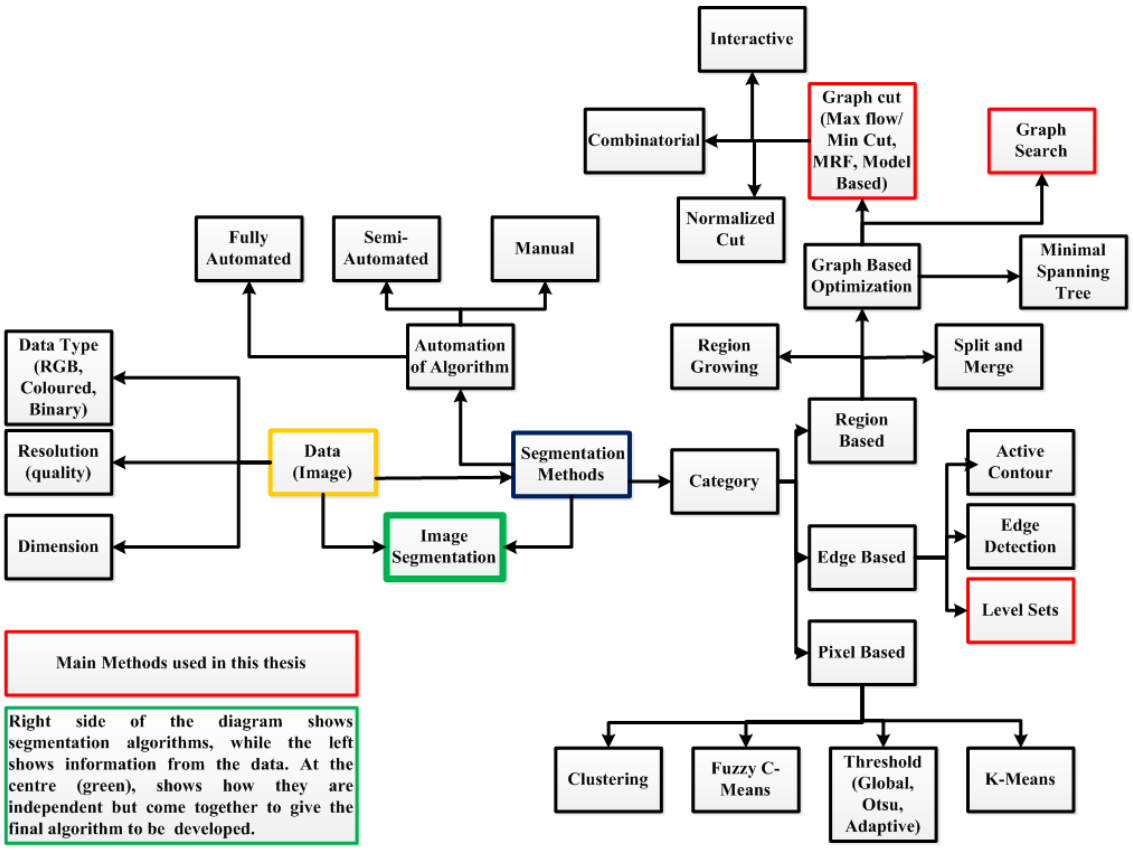

Figure 2.11: Image segmentation methods and information from data that determines how the algorithm is developed.

2.7 Background Summary

The main reason for much research in automated intraretinal layer segmentation is to enable the development of more plausible quantitative tools to help clinicians diagnose and monitor eye diseases. The potential impact of automated segmentation applications is high due to the vast amounts of information contained in OCT images. For example, It is possible that the thickness of the ganglion cell layer in macular OCT scans can indicate ganglion cell loss at an earlier stage in cases of optic nerve swelling. Therefore, to better understand what quantitative features on OCT images indicate eye diseases such as diabetic retinopathy, AMD, and glaucoma, intraretinal layer segmentation is necessary to extract individual layer thickness.

Figure 2.11 provides an overview of the discussed literature and image segmentation. Each

box represents a specific area of research with substantial literature, although directly or indirectly dependent on one another. The right side of the diagram shows segmentation algorithms (blue), while the left shows information from the data (yellow), and at the centre (green) it shows how they are independent but come together to give the final algorithm to be developed. Specifically, all the segmentation methods have a mathematical background, with the exception of region growing. The information (prior knowledge [1]) derived from the data determines the constraints set in the algorithm. Combining these two elements ensures a robust and objective algorithm is developed. It is essential to understand the data, as it plays a crucial role in how the segmentation problem is approached and which algorithm to use.

In this thesis, we use the prior knowledge of the retinal OCT image and a selection of segmentation methods to segment different retinal layers, which provides crucial information to clinicians for diagnosing and monitoring prevalent eye diseases. Although the thesis focuses on retinal image analysis, it addresses some of the challenges of image segmentation in the broader perspective.

[1] Prior knowledge - refers to the layer reflectivity on an OCT image and the retina topology. To avoid terminological confusion, the prior knowledge should not be confused with the prior probability in Bayesian image analysis [124, 125]

Chapter 3

Graph-Cut Segmentation

This chapter presents a comprehensive and fully automatic method for segmentation of retinal layers in OCT images, which is comprised of fuzzy histogram hyperbolisation and graph cut methods to segment 7 layers of the retina across 8 boundaries. One of the main ideas behind this chapter is based on the fact that graph-cut method depends on the assignment of appropriate weights. Therefore, this chapter uses a computationally inexpensive method to improve weight calculation. Specifically, the method utilises normalised vertical image gradients [1], and their inverse [2] to represent image intensity in calculating two adjacency matrices. Then the weights in these adjacency matrices are reassigned to make edges along retinal boundaries have a low cost. The integration of the enhanced adjacency matrices from gradient information, which captures the unique characteristics of retinal structures, into the graph cut framework allows the method to find the actual minimum paths. Finally, the weight calculation is followed by a sequential segmentation process based on individual layer characteristics.

3.1 Introduction

Medical images are an integral part of health care for diagnosis, clinical studies, research, and learning [113]. Medical images are highly complex to handle and analyse, for many reasons

[1] re-scaling to [0 1]

[2] multiply the normalised gradient by $\times -1 + 1$

including, the obstruction of speckle noise, managing large volumes of data and extracting useful information from the data [153]. In particular, ophthalmic imaging technologies have witnessed an ever-growing scale of retina images, both in volume and variety. Nowadays, the 2D fundus images are widely available in the high-street opticians, while the recent 3D Optical Coherence Tomography (OCT) [77] images have gradually become a standard imaging modality in clinical practice. However, this vast amount of imaging data are stored mainly in their raw format. Even after diagnosis and treatment, the relevant medical information provided by the clinical experts, if any, is typically recorded separately from the images. The lack of high-level information on the retinal image, e.g. labels, tags, markers and measures, has hindered the development of new methods of diagnosis and treatment. To a greater level, this has also presented a significant challenge to healthcare analytics. Furthermore, the severity of various eye diseases and cardiovascular disorders have been shown to correlate with changes in retinal structures [1, 134, 176]. Hence, due to the ability of OCT to provide high-resolution images of the retina, it has become a vital tool in the diagnosis of eye diseases. An essential aspect of the diagnostic process is obtaining individual layer properties. However, manual segmentation processes are tedious. Due to the critical nature and open challenge of segmentation, many computational methods have been proposed to aid with the segmentation process.

Motivated by the challenges as mentioned earlier, this work aims to develop a comprehensive and fully automatic method for segmentation of retinal layers in OCT images. The method will provide the most basic but yet crucial structural information to the original raw data, and serve as a starting step for any further and large-scale healthcare analytics. In theory, segmentation is the separation of images into more meaningful information based on similarity or difference, continuity or discontinuity [171]. One of the well-researched methods of segmentation is Graph-based methods. Segmentation using graph cut methods depends on the assignment of appropriate edge weight. The paths obtained by the standard shortest path algorithms [32, 46] have no optimal way of handling inconsistencies (such as the irregularity in OCT images), as thus it sometimes obtains the wrong paths, which we call the "wrong short-cuts". To avoid the wrong short-cuts, we reassign the weights to promote the homogene-

ity between adjacent edges using fuzzy histogram hyperbolization. In other words, the edges with high value get higher weights, while edges with low values get lower weights. The idea behind this is that the transition between layers of OCT images which are from dark-bright or vice versa are improved. This means we can better identify the layers by searching for the changes or transitions between layer boundaries. Primarily, we take into account the transition between the layers is, in most cases very smooth, making it quite challenging to segment the layers. Now if we re-emphasise on these changes, such that they become lucid, this aids the algorithm in successful segmentation and avoiding wrong short-cuts.

In this study, we take into account the effect of promoting continuity and discontinuity, in addition to adding hard constraints based on the structure of retina to segment seven retinal layers by detecting eight layer boundaries. Distinctly, the layers are: Nerve Fibre Layer (NFL); Ganglion Cell to Layer-Inner Plexiform Layer(GCL+IPL); Inner Nuclear Layer (INL); Outer Plexiform Layer (OPL); ; Outer Nuclear Layer to Inner Segment (ONL+IS); Outer Segment (OS) and Retinal Pigment Epithelium (RPE). The locations of these layers and boundaries in an OCT image are illustrated in Figure 3.1. This chapter is organised as follows. In

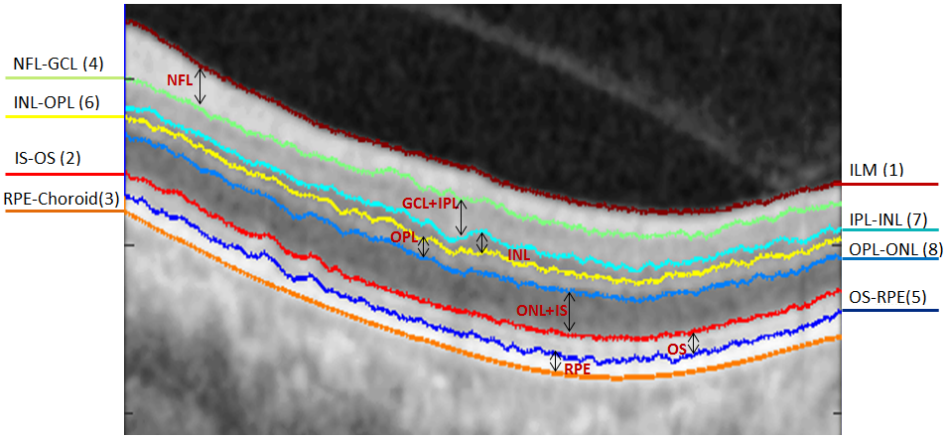

Figure 3.1: Illustration of the 8 boundaries and 7 retinal layers segmented in the study. The numbers in brackets are the sequential order of the segmentation.

Section 3.2, we review previous work on noise handling and retinal layer segmentation of OCT images. Section 3.3 describes the proposed graph cut segmentation method. Section 3.4 presents experimental results on 150 OCT images including discussion. Finally conclusions

are drawn in Section 3.5.

3.2 Background

3.2.1 Noise and Noise Handling in Retinal OCT

In OCT images, two main kinds of noise exist, i.e. the speckle noise during acquisition and the shadows of blood vessels. Speckle noise in OCT images causes difficulty in the precise identification of the boundaries of layers or other structural features in the image either through direct observation or use of segmentation algorithms [84, 115]. The noise that corrupts OCT images is non-Gaussian, multiplicative, and neighbourhood correlated. Thus, it is not easily suppressed by standard software denoising methods [111]. Since OCT images are highly corrupted by speckle noise, some pre-processing steps are usually performed to reduce the effect of noise. In most cases, even though the segmentation algorithms are designed to handle uncertainties and noise, the pre-processing is used as a first step to handling the noise, irrespective of whether the analysis is performed in 2D [21, 82, 164] or 3D [165, 167, 168], in order to remove the speckle noises and enhance the contrast between layers.

Previous attempts, including spatial and frequency compounding techniques, have been used to address the problem of speckle noise in OCT [78, 133]. However, the tolerance or adaptability of these techniques is limited, which then complicates the analysis stage. They are also quite sensitive to the choice and fine-tuning of various parameters [145, 153]. Further, the use of digital filters has been proposed to suppress the speckle noise on OCT images, such as median filtering, wavelet-based filtering that employs nonlinear thresholds, anisotropic diffusion filtering [45], and nonlinear anisotropic filtering [62].

Moreover, the median filter is one of the most popular methods used in OCT image denoising [84]. The median filter has been used solely by [94, 149], and in combination with other enhancement techniques. George et al. [56] used the median filter and image homogenization using Nagao filter. A 4 x 4 median filter was applied twice to enhance the performance of the filter in OCT denoising by [70, 93], which was later improved in combination with a Palladian of Gaussian (1D) edge detector by Boyer et al. [14]. Recently, Lu et al. [104] combined the

median filter and bilateral filter. The basic problem associated with the median filter and most denoising algorithms is their intrinsic consequence in decreasing the image resolution [31, 84]. Although some of these methods are effective in reducing speckle noise, most incline to blur the structural boundaries in the OCT image. In fact, most of these algorithms use a defined filter window to estimate the local noise variance of a speckle image and perform the individual unique filtering process. The result is generally a reduced speckle level in homogeneous areas. However, the image is either blurred or over smoothed due to losses in detail in non-homogeneous areas like edges or lines. Also, the conventional algorithms in OCT segmentation do not consider the intensity inhomogeneity in the image, which can lead to inaccurate segments and inability to detect all layers.

Clearly, the primary goal of noise reduction is to remove the noise without losing much detail contained in an image [145]. We propose a method that preserves the edge information and improves visibility by hyperbolizing the image. This improves the homogeneity of pixel values in every layer, which consequently improves the performance of the segmentation method, and makes the method applicable, for diagnosis and tracking medication progress of ocular diseases.

3.2.2 Previous Work

The segmentation of retinal layers has been an area of active research and has drawn a large number of researches, since the introduction of Optical Coherence Tomography (OCT) [77]. Various methods have been proposed, some with focus on the number of layers, others on the computational complexity and efficiency, graph formulation and mostly now optimisation approaches. Segmentation of retinal images is challenging and requires automated analysis methods [8]. In this regard, a multi-step approach was developed by [9]. However, the results obtained were highly dependent on the quality of images and the alterations induced by retinal pathologies. A 1-D edge detection algorithm using the Markov Boundary Model [93], which was later extended by [14] to obtain the optic nerve head and RNFL. Seven layers were obtained by [21] using a peak search interactive boundary detection algorithm based on local coherence information of the retinal structure. The Level Set method was reported by [126, 166, 167, 168],

which were computationally expensive compared to other optimisation methods. Graph-based methods in [55, 64, 82, 183] have reported successful segmentation results, with varying success rates. Recently, [39] proposed a method using the Fuzzy Histogram Hyperbolization (FHH) to improve the image quality, then embedded the image into the continuous max-flow to simultaneously segment 4 retinal layers.

Moreover, the use of gradient information derived from the retinal structures has in recent years been of interest to OCT segmentation researchers. Chiu et al. [27] utilised the gradient information with the Graph-Cut method, where the retinal structure is employed to limit search space and reduced computational time using dynamic programming. This method was recently extended to a 3D volumetric analysis by [156] in OCTRIMA 3D with edge map and convolution kernel in addition to hard constraints in calculating weights. They also exploited spatial dependency between adjacent frames to reduce processing time. A combination of edge detection and polynomial fitting is yet another approach proposed to derive boundaries of the retinal layers from gradient information by [105], and machine learning by [96] with the use of random forest classifier. The utilisation of gradient information on OCT images is mainly due to the changes that occur at layer boundaries in the vertical direction, thereby attracting segmentation algorithms to exploit this advantage. The method takes into account the retinal structure and gradient information. More importantly, the re-assignment of weights in the adjacency matrix, because segmentation using graph cut methods depends on the assignment of appropriate edge weight as highlighted earlier.

3.3 Methods

In this section, we provide the details of the graph-cut approach to segmenting seven layers by identifying eight retinal layer boundaries on OCT B-Scan images. A schematic representation of the method is illustrated in Figure 3.2. Some parts of this method have been published earlier in [34, 39]

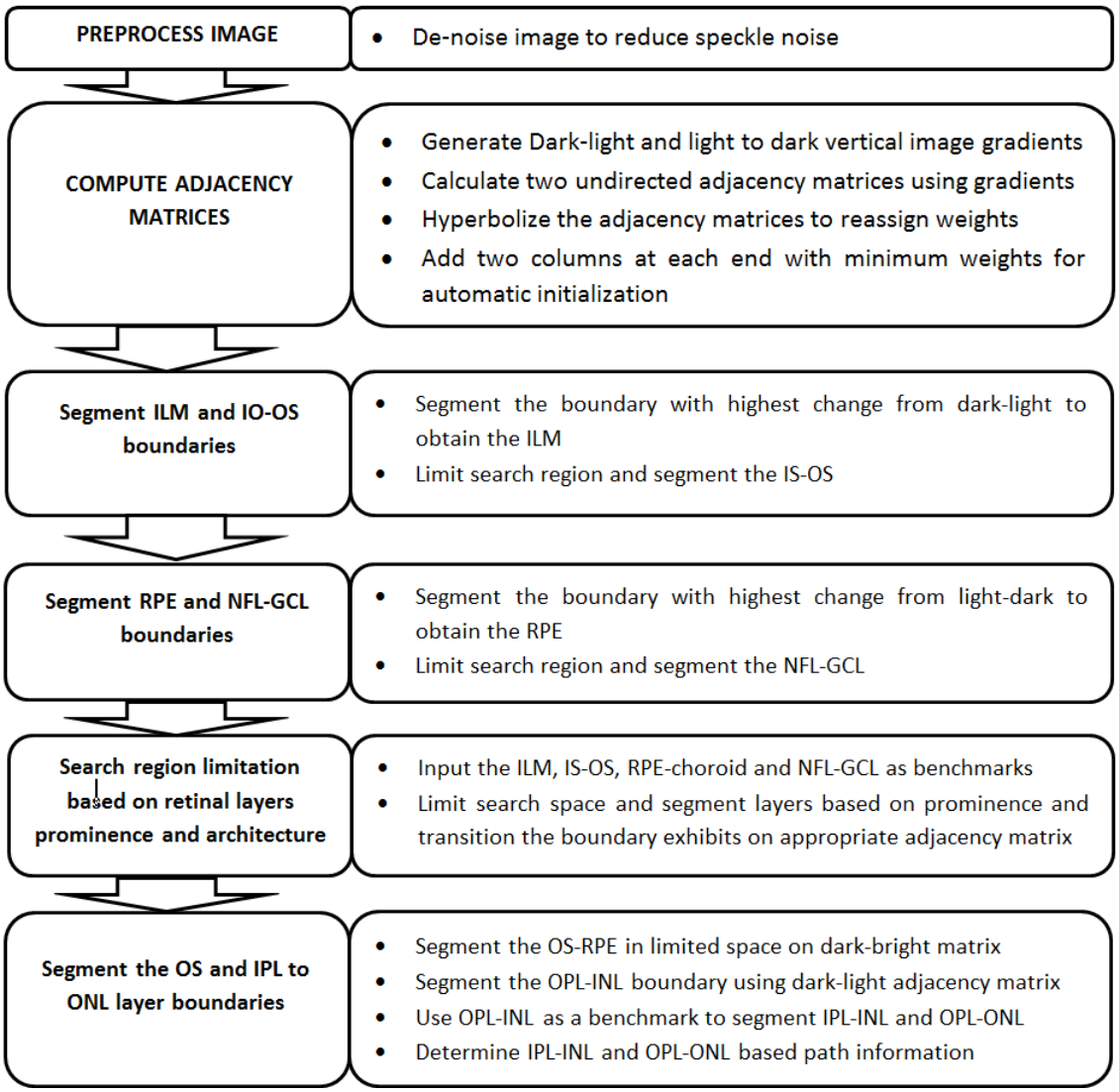

Figure 3.2: Schematic representation showing the main steps of the graph-cut segmentation algorithm.

3.3.1 Pre-Processing

Speckle noise is ubiquitous in OCT images, as elaborated in the previous section 3.2, which has negative effects on further processing. For example, the retinal OCT images have a low Signal to Noise Ratio (SNR) due to the strong amplitude of speckle noise.

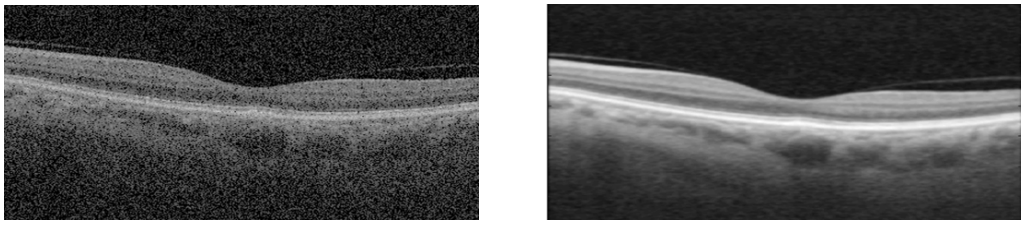

(a) (b)

Figure 3.3: Image pre-processing. (a) Original image corrupted by speckle noise, and (b) filtered image by Gaussian ($\sigma = 3$).

Various methods have been used to handle the presence of noise. Gaussian filters are commonly used for image preprocessing, and an example of a preprocessed image using Gaussian filter compared to its original is shown in Figure 3.3. The Gaussian generally is able to suppress the speckle noise and improve homogeneous regions. However it is not ideal for OCT as it requires fine tuning of the filter window and is also unable to improve the homogeneity in inhomogeneous regions. Consequently, a method for preprocessing OCT using Fuzzy histogram hyperbolization (FHH) is proposed. FHH is simple and straight forward, yet effective to a range of image and signal processing applications [106]. The method starts by representing every image I, by the following [52]:

$$I = \bigcup_{m}^{M} \bigcup_{n}^{N} \frac{\mu_{mn}}{g_{ij}} \tag{3.1}$$

Where g_{ij} represents the intensity of the ij^{th} pixel and μ_{mn} its membership value, given $m = 1, 2, 3 \ldots M$ and $n = 1, 2, 3 \ldots N$. In line with this, using the linear index of fuzziness, we calculated image fuzziness with [157] :

$$\gamma(I) = \frac{2}{MN} \sum_{i=1}^{N} \sum_{j=1}^{M} min[\mu_I(g_{ij}), \bar{\mu}_I(g_{ij})] \tag{3.2}$$

where $\mu_I(g_{ij})$ is the membership function of greylevel g_{ij} and $\bar{\mu}_I(g_{ij}) = 1 - \mu_I(g_{ij})$. This maps image greylevel intensities into a fuzzy plane using membership functions. The membership functions are modified for contrast enhancement, and the fuzzy plane is mapped back to image grey level intensities. The aim is to generate an image of higher contrast than the original image by giving larger values to the greylevels that are closer to the mean greylevel of the image than to those that are farther from the mean.

Using the concept of fuzzy histogram hyperbolisation described in [158, 159], we calculate membership (re-scale the image to [0,1]) value for each grey-level as:

$$\mu(g_{ij}) = \frac{g_{ij} - g_{min}}{g_{max} - g_{min}} \tag{3.3}$$

where the maximum and minimum intensity values are represented by g_{max} and g_{min} respectively. Then the parameter β acts as a fuzzifier, which determines the level of transformation and the desired grey level value L. These parameters, β and L are used to calculate the new grey values of image using the following transformation [159]:

$$g_{ij} = (\frac{L-1}{e^{-1}-1}) \times [e^{-\mu(g_{ij})^{\beta}} - 1] \tag{3.4}$$

The value of β determines a number of operations that could be performed with membership modification [158]. The main idea behind equation 3.8 is to transform the values of the image, such that brighter layers become brighter, while the darker layers become darker. This makes the edges clearer, and enhances the outcome of the segmentation process. The outcome of the equation 3.8 is shown in figure reffig:enhanca. As the value of β approaches 0, the results are similar to that of histogram equalization, whereas if β approaches values 5 and above, it tends to provide result similar to segmentation. We therefore take two issues into consideration: 1) Most image de-noising processes are sensitive to the choice of various parameters [145]. 2) The fuzzifier β modifies the membership values additionally, and so, the gray level dynamics of the resulting image can be changed [158]. Consequently, the value of β from equation (3.4)

is constrained to arbitrate within a specified window by the following conditions:

$$\begin{aligned} \beta &= \beta + C \\ \beta &= \beta_{min} \qquad if \quad \beta + C < \beta_{min} \\ \beta &= \beta_{max} \qquad if \quad \beta + C > \beta_{max} \end{aligned} \tag{3.5}$$

where β_{min} and β_{max} are the minimum and maximum acceptable values of β. To achieve the above, we introduce a constant C, called the stabiliser. The stabiliser keeps the value of β within the set threshold. This allows the method to set a suitable value for the image based on the membership information without the need for user input. Of course, the threshold values can always be adjusted easily, for the method to adapt to a wider range of images and applications. However, we limit the study to the enhancement of retinal OCT images to suppress and handle speckle noise and blood vessel interference. After the transformation, the image is enhanced, and this has a positive effect in calculating the flow. Examples of image transformations with various values of β are shown in Figure 3.4. For this image, β is set to 2.2 in the experiment and will vary depending on the image.

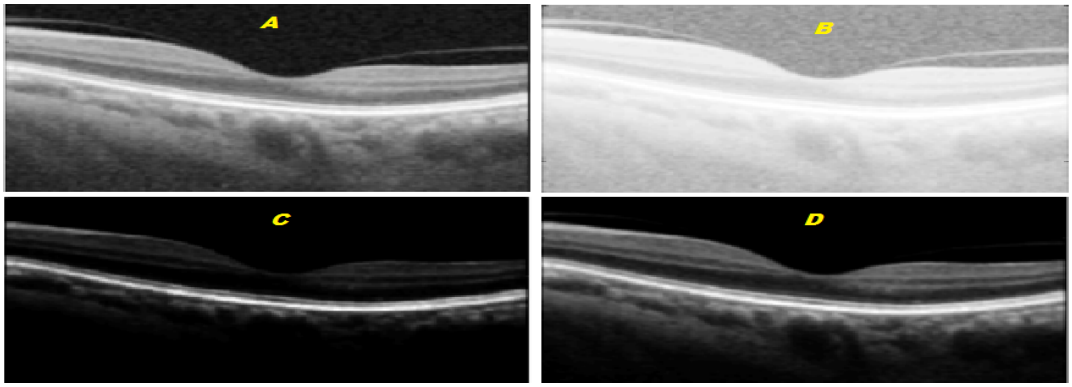

Figure 3.4: Image Enhancement from equation 3.8. A - unprocessed image; B - transformed images with β= 0.3; β =5; and D - transformed images with β = 2.2 (the computed value for this image).

Unlike other preprocessing methods, which reduce image quality or leads to loss of data, this method preserves edge information and adapts to OCT inconsistencies as the value is computed based on each image. This allows the method to adapt to different OCT images. The use of fuzzy histogram hyperbolisation is further discussed in chapter 6.

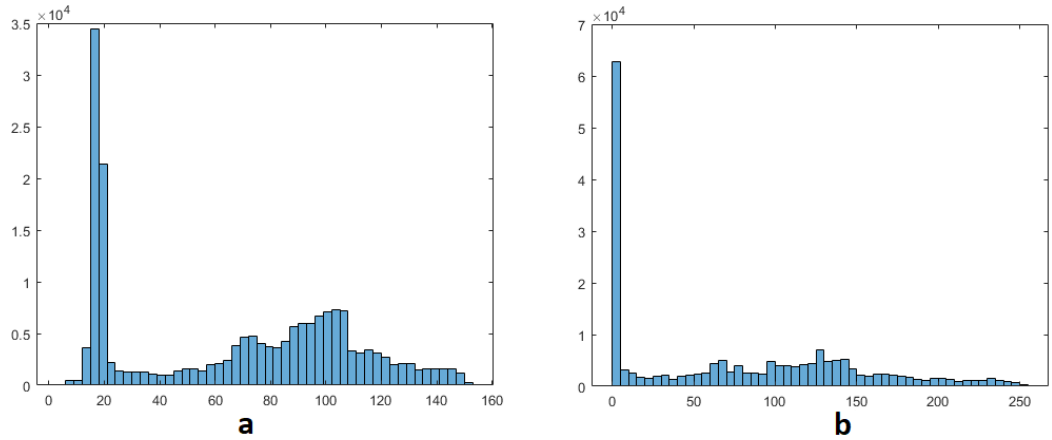

Figure 3.5: Sample histogram of images: a - Histogram of Figure 3.4A and b - Histogram of Figure 3.4D

3.3.2 Graph formulation and Weight Calculation

In formulating the graph, we consider the fact that there is always a transition from bright-dark or dark-bright at layer boundaries in the vertical direction [26, 27, 156]. Hence, it is befitting that we use two adjacency matrices to represent these transitions. To achieve this, we obtain the vertical gradient of the image, normalise the gradient image to values in the range of 0 to 1, and then obtain the inverse of the normalised image gradient as shown in Figure 3.6. These two normalised gradient images are then used to obtain two separate undirected

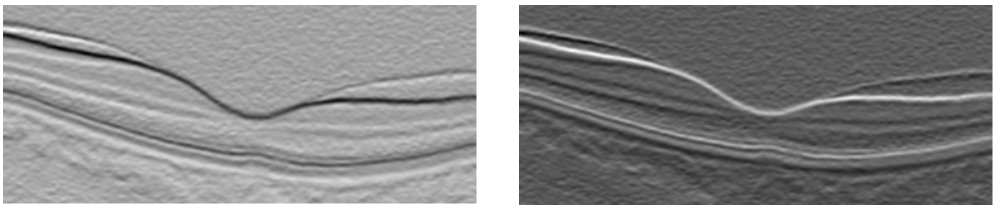

(a) (b)

Figure 3.6: Image gradients used in generating adjacency matrices: (a) - normalised vertical image gradient computed by rescalling vertical image gradient to [o 1] containing dark-bright layer information and (b) - inverse computed by multiplying figure 3.6a(a) by $\times -1+1$ containing bright-dark adjacency matrix.

adjacency matrices, where Figure 3.6 (a) contains information of bright-dark layer transitions while Figure 3.6 (b) contains information for layer transitions from dark-bright. Perhaps second derivatives might capture the layer information and improve the segmentation results.

The adjacency matrices are formulated with the following equation adapted from [27]:

$$w_{ab} = 2 - g_a - g_b + w_{mw} \tag{3.6}$$

where w_{ab}, g_a, g_b and w_{mw} are the weights assigned to the edge connecting any two adjacent nodes a and b, the vertical gradient of the image at node a, the vertical gradient of the image at node b, and the minimum weight added for the graph stabilisation. The resulting adjacency matrices are weighted undirected acyclic graphs. To improve the continuity and homogeneity in the adjacency matrices they are hyperbolized, firstly by calculating the membership function with the fuzzy sets equation (3.7) [159] and then transformed with equation (3.8).

$$w'_{ab} = \frac{w_{ab} - w_{ij}}{w_{max} - w_{min}} \tag{3.7}$$

where w_{min} and w_{max} represents the maximum and minimum values of the adjacency matrix respectively. The adjacency matrices are then transformed with the following equation:

$$w''_{ab} = (w'_{ab})^{\beta} \tag{3.8}$$

where w'_{ab} is the membership value from equation (3.7), and β, the fuzzifier is a constant. Considering the number of edges in an adjacency matrix, we use a constant β instead of calculating the fuzziness. The main reason is to reduce computational time and memory usage. The resulting adjacency matrices are such that the weights are reassigned, and the edges with high weights get higher values while those with low values get lower edge weights. The motive here is that, if continuity or discontinuity is re-emphasised the algorithm will perform better. Where in this case we improve both, the region of the layers get values close to each other, while that of the background gets lower along the way, this is more realistic and applicable in this context (as the shortest path is a greedy search approach), because at the boundary of each layer there is a transition from bright to dark or dark to bright, and therefore improving it aids the algorithm in finding correct optimal solutions that are very close to the actual features of interest.

The weight calculation is followed by several sequential steps of segmentation that will be addressed in the next few subsections. We adopt layer initialisation from [27], where two columns are added to either side of the image with minimum weights (w_{mw}), to enable the cut to move freely in those columns. This initialisation is based on the understanding that each layer extends from the first to last column of the image, i.e. dividing the image horizontally at each layer boundary, and that the Graph-Cut method prefers paths with minimum weights. We use Dijkstra's algorithm [32] in finding the minimum weighted path in the adjacency matrix, which corresponds to layer boundaries (other optimisation methods utilising sparse adjacency matrices might be used in finding the minimum path). Graph-Cut methods are optimal at finding one boundary at a time, and therefore to segment multiple regions in most cases, requires an iterative search in limited space. Limiting the region of search is a complex task, as it requires prior knowledge and is dependent on the structure of the features (regions of interest). Some additional information on automatic layer initialisation and region limitation are discussed in [27, 34, 82].

3.3.3 ILM (B1) and IS-OS Segmentation (B2))

It is commonly accepted that the NFL, IS-OS and RPE exhibit high reflectivity in an OCT image [27, 105, 156]. This is also evident from previously conducted studies [39], where we segmented the two most reflective layers. Taking into account this reflectivity and the dark-bright transition, we segment the ILM (B1) and IS-OS (B2) boundaries using Dijkstra's algorithm [32]. The ILM (vitreous-NFL) boundary (B1) is segmented by searching for the highest change from dark-bright, this is because there is a sharp change in the transition, additionally it is amidst extraneous features, above it is the background region in addition to no interruption of the blood vessels, as can be seen in the gradient image. All of the above reasons make it easier to segment the ILM than other layers. We then limit the region below ILM and search for the next highest change from dark-bright in order to segment the IS-OS boundary. In most cases the ILM is segmented, but to account for uncertainties, i.e. to differentiate or confirm which layer was segmented, we use the mean value of the vertical axis of the paths to determine the layer segmented, as the ILM is above the IS-OS (similar to [27].

3.3.4 RPE (B3) and NFL-GCL (B4) Segmentation

As mentioned in the previous subsection, RPE is one of the most reflective layers. On the bright-dark adjacency matrix, the RPE-Choroid (B3) boundary exhibits the highest bright-dark layer transition as can be seen in Figure 3.6 (a). Additionally based on experimental results, it is better to search for the transition from bright-dark for the RPE, due to the interference of blood vessels and the disruption of hyper-reflective pixels in the choroid region. Therefore searching for the bright-dark transition is ideal for the RPE most especially to adapt to noisy images. To segment the NFL-GCL (B4) boundary, we limit the search space between ILM (B1) to IS-OS (B2) and utilise the bright-dark adjacency matrix to find the minimum weighted path. The resulting path is the NFL-GCL (B4) boundary, as it is one of the most hyper-reflective layers. On other notes, the NFL-GCL (B4) and IS-OS (B2) boundaries exhibit the second highest bright-dark and dark-bright transition, respectively in an OCT image. If we limit the search space to regions below the ILM and above the RPE, the resulting bright-dark and dark-bright minimum paths are the NFL-GCL and IS-OS respectively. It is also significant to note we use the paths obtained from one adjacency matrix to limit the region on either of the matrices. This path utilisation is feasible because the paths are (x, y) coordinates and the matrices are of the same size. For example, in finding the NFL-GCL boundary on the bright-dark adjacency matrix, we use paths of the ILM and IS-OS obtained from the dark-bright matrix to limit the search region.

3.3.5 OS (B5) and IPL to ONL (B6-B8) Segmentation

To segment the OS-RPE (B5) and three other boundaries (IPL-INL, INL-OPL, and OPL-ONL (B6-B8)) from IPL to ONL, we use the prior segmented layer boundaries (B1-B4) as benchmarks for search space limitation. We obtain the OS-RPE (B5) boundary by searching for the dark-bright shortest path between IS-OS (B2) and the RPE-Choroid (B3). For the remaining boundaries, INL-OPL (B6) is segmented first, because it exhibits a different transition among the three. Thus, the INL-OPL (B6) is obtained by searching for the shortest path between NFL-GCL (B4) and IS-OS (B2) on the dark-bright adjacency matrix. Consequently, by utilising the bright-dark adjacency matrix, the IPL-INL (B7) and OPL-ONL (B8) boundaries are

obtained by limiting the region of path search between INL-OPL (B6) and NFL-GCL (B4), and INL-OPL (B6) and IS-OS (B2) boundaries respectively. The order in which these layer are segmented and the boundaries used for search region limitation are shown in Figure 3.7.

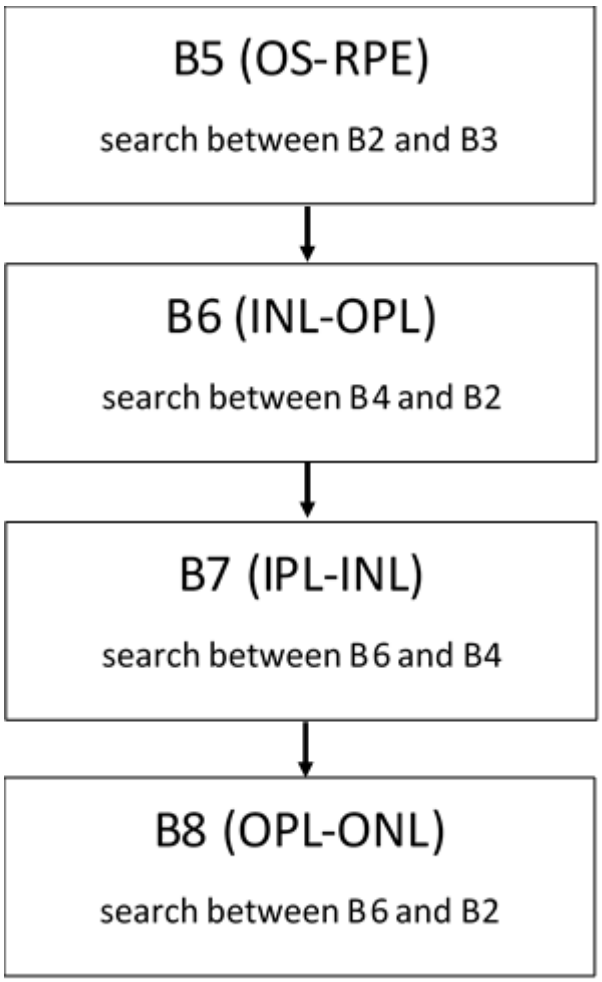

Figure 3.7: Order of segmentation of boundaries OS (B5) and IPL to ONL (B6-B8)

3.3.6 Avoiding the Cortical Vitreous

The vitreous cortex depicts a layer-like structure, just above the ILM (B1), which lures the algorithm into finding unintended boundaries as illustrated in Figure 3.8. To handle this issue, we impose a hard constraint to restrict all paths to lie between the ILM(B1) to RPE (B3) boundaries exclusively. This constraint is ideal because the ILM exhibits the highest transition

from dark-bright, while the RPE exhibits the highest transition from bright-dark. Thus, the constraint helps the algorithm in avoiding features that imitate the retinal structures and are not of interest.

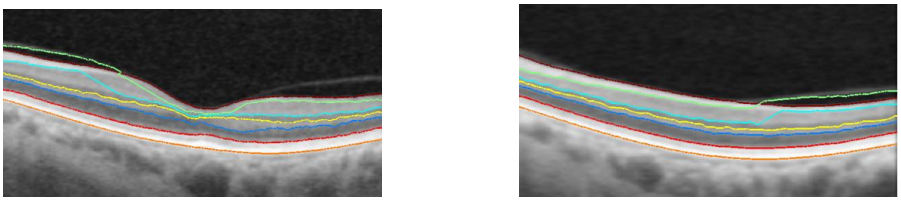

Figure 3.8: Error in Segmentation caused by Vitreous Cortex at temporal region (left) and Nasal region (right).

3.4 Results and Discussion

We evaluated the performance of the proposed method on a set of 150 B-scan OCT images centred on the macular region. The data set was collected in Tongren Hospital with a standard imaging protocol for retinal diseases such as glaucoma. The resolution of the images is 512 pixels in depth and 992 pixels across section with 16 bits per pixel. Before segmenting the images, 15% per cent of the image height was cropped from the top to remove regions with low signal and no features of interest. We segment seven retinal layers automatically using MATLAB 2016a software [3]. The average computation time was 4.25 seconds per image on a PC with Intel i5-4590 CPU, clock of 3.3GHz, and 8GB of RAM. The method obtains the boundaries in the order from ILM (Vitreous-NFL), IS-OS, RPE-Choroid, NFL-GCL, OS-RPE, INL-OPL, IPL-INL to OPL-ONL respectively. As indicated earlier, the locations of these boundaries and the sequential order of the segmentation are shown in Figure 3.1.

Sample results of the 8 retinal layer boundaries and the underlying 7 layers are depicted in Figure 3.9. Taking a close look at figure 3.9 (middle right) merging at the foveal region is usually a challenge. Our method is able to avoid layer merging as shown in figure 3.10. To evaluate the performance of proposed method we calculate the Root Mean Squared Error (RMSE), and Mean Absolute Deviation (MAD) by equation (3.9). Table 3.1 shows the mean

[3] combines a desktop environment tuned for iterative analysis and design processes with a programming language that expresses matrix and array mathematics directly. https://uk.mathworks.com/products/matlab.html

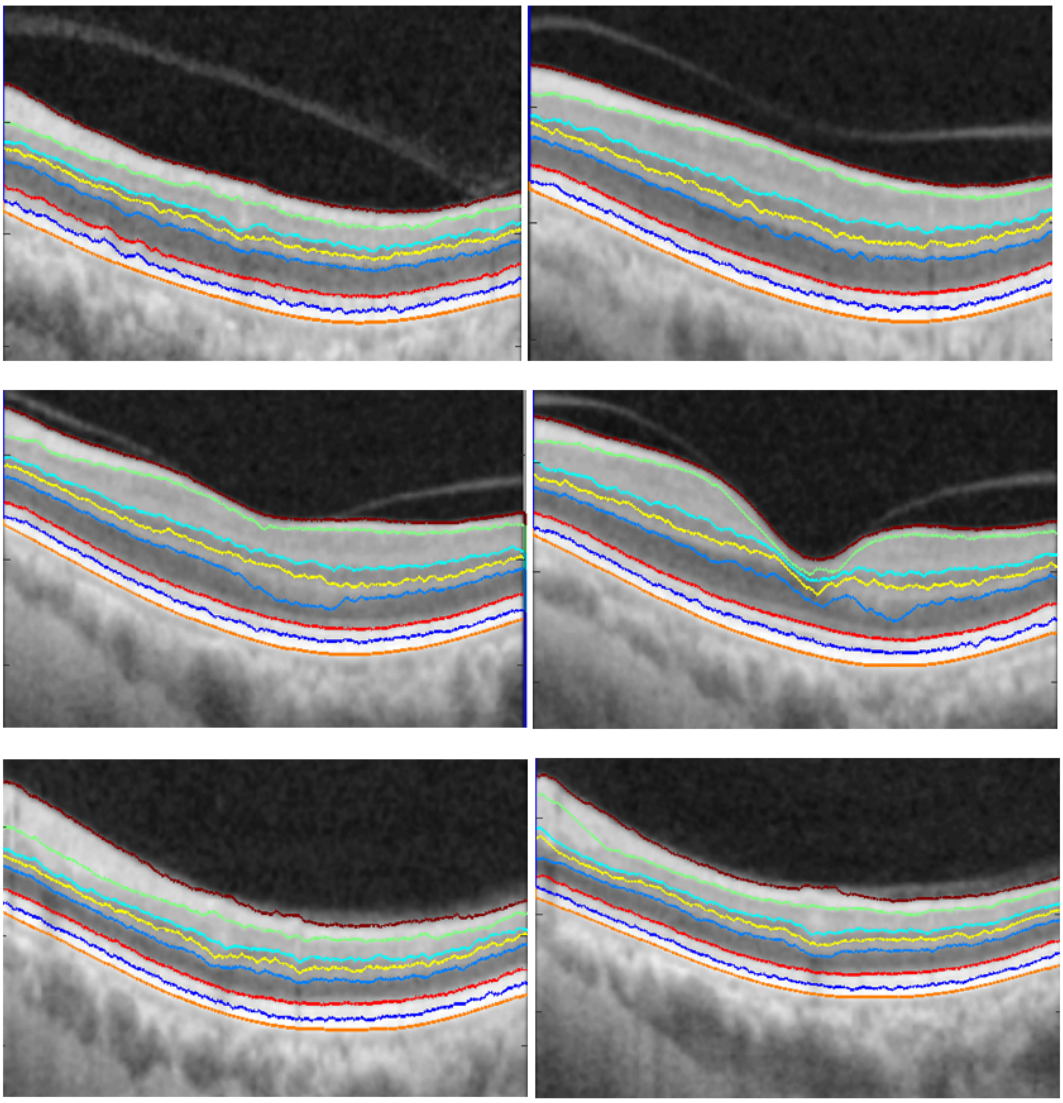

Figure 3.9: Segmentation results of 8 boundaries and 7 layers. Boundaries from top to bottom, the segmented boundaries are ILM, NFL-GCL, IPL-INL,INL-OPL, OPL-ONL, IS-OS, OS-RPE and RPE-Choroid.

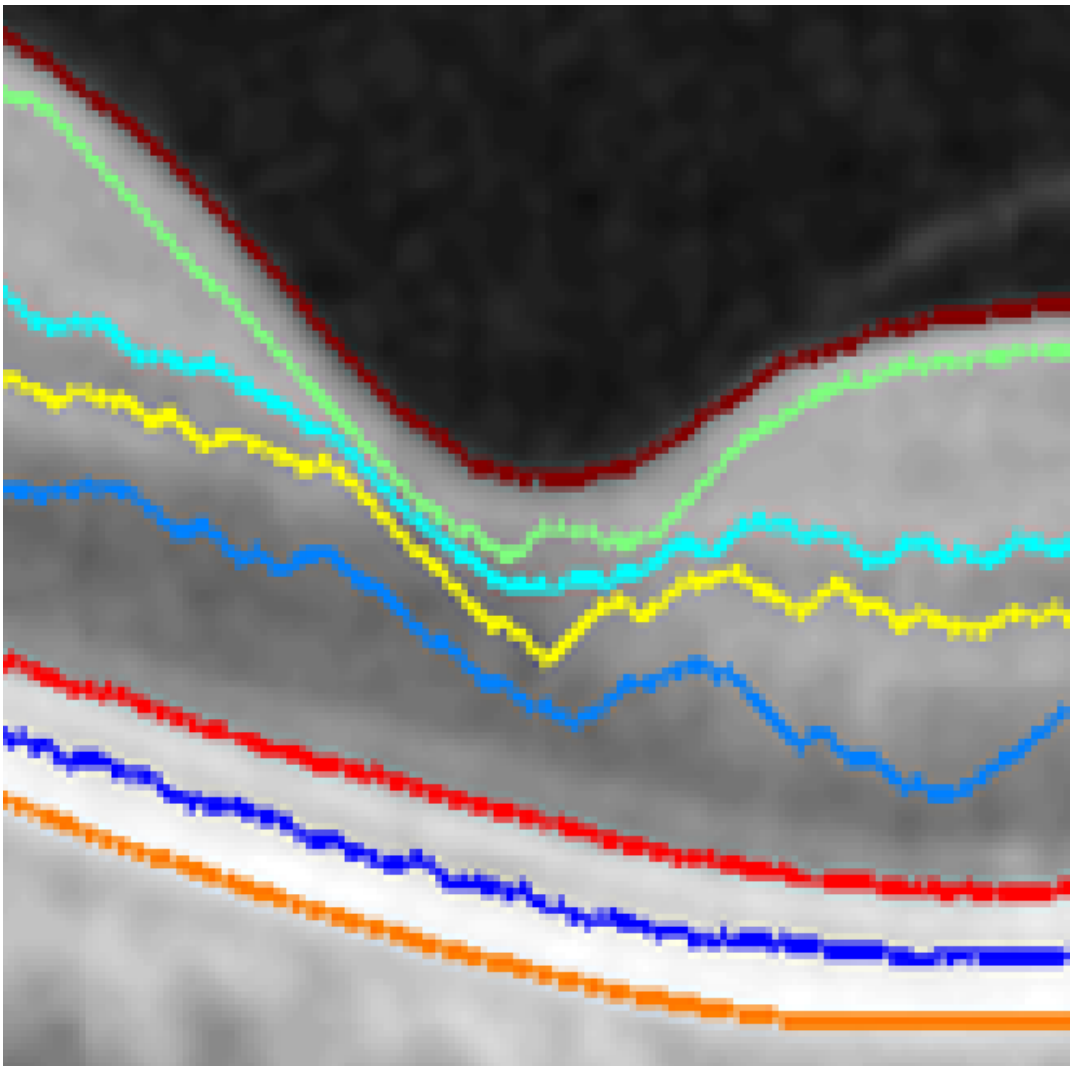

Figure 3.10: Zoomed view of figure 3.9 (middle right).

and standard deviation of both MAD and RMSE, for the seven layers targeted in this study. The evaluation matrices are computed by [81, 124, 163]

$$\begin{aligned} &MAD(GT, SEG) = \\ &0.5 \times \left(\frac{1}{n} \sum_{i=1}^{n} d(pt_i, SEG) + \frac{1}{m} \sum_{i=1}^{m} d(ps_i, GT) \right) \\ &RMSE = \sqrt{\frac{1}{n} \sum_{i=1}^{n} (SEG_i - GT_i)^2} \\ &Dice \qquad\qquad = \frac{2 \mid GT_i \cap SEG_i \mid}{\mid GT_i \mid + \mid SEG_i \mid} \end{aligned} \tag{3.9}$$

where SEG_i is the pixel labelled as retinal Layer by the proposed segmentation method and GT_i is the true retinal layers pixel in the ground truth image. The terms pt_i and ps_i represent the coordinates of the images, while $d(pt_i, SEG)$ is the minimum distance of pt_i to the set of pixels on SEG with the same segmentation label, and $d(ps_i, GT)$ is the minimum distance of ps_i to the set of pixels on GT with the same segmentation label. n and m are the number of points on SEG and GT respectively. For all layers the method has performed well. Especially considering the low value of NFL for both MAD and RMSE. The high value in ONL+IS is due to the presence of high noise and lower reflectivity of the boundaries within the region, however, this is still considerably low.

Table 3.1: Performance evaluation with mean and standard deviation (SD) of RMSE and MAD for 7 retinal boundaries. 150 SD-OCT B-Scan images (Units in pixels).

$RetinalLayer$	$MAD(SD)$	$RMSE(SD)$
NFL	0.2688 (0.0185)	0.0165 (0.0121)
GCL+IPL	0.5762 (0.0590)	0.0415 (0.0378)
INL	0.6307 (0.0785)	0.0373 (0.0612)
OPL	0.4839 (0.0410)	0.0446 (0.0335)
ONL+IS	0.6596 (0.0823)	0.0592 (0.0329)
OS	0.4401 (0.0362)	0.0328 (0.0156)
RPE	0.4369 (0.3291)	0.0311 (0.0142)

Furthermore, We evaluated the retinal nerve fibre layer thickness (RNFLT) (the area between ILM (B1) and NFL-GCL (B4)) with additional criteria, due to its high importance in

Table 3.2: Mean for accuracy, sensitivity, error rate and Dice coefficient of the Retinal Nerve Fibre Layer Thickness (RNFLT) and their respective standard deviation (STD) [34].

Criteria	*Mean*	*STD*
Accuracy	0.9816	0.0375
Sensitivity	0.9687	0.0473
Error Rate	0.0669	0.0768
Dice	0.9746	0.0559

the diagnosis of ocular diseases, including glaucoma. The NFL evaluation is conducted using four criteria, namely, accuracy [4], sensitivity (true positive rate (TPR)), error rate (FPR) and the Dice score (coefficient/index). The measurements are computed with the following equations while the Dice is computed from equation (3.9):

$$\begin{aligned} Accuracy &= \frac{TP+TN}{(TP+FP+FN+TN)} \\ Sensitivity(TPR) &= \frac{TP}{(TP+FN)} \\ ErrorRate(FPR) &= \frac{FP}{(FP+TN)} \end{aligned} \tag{3.10}$$

where TP, TN, FP and FN refers to true positive, true negative, false positive and false negative respectively. TP represents the number of pixels which are part of the region that are labelled correctly by both the method and the ground truth. TN represents the number of pixels which are part of the background region and labelled correctly by both the method and the ground truth. FP represents the number of pixels labelled as a part of the region by the method but labelled as a part of the background by the ground truth. Finally, FN represents the number of pixels labelled as a part of the background by the system but labelled as a part of the region in the ground truth. The Mean and Standard Deviation of applying the above criteria on the achieved results for the RNFLT are shown in Table 3.2, and the distribution of these values in Figure 3.11. Some of the conclusions we draw from the results in Table 3.2 and their distribution Figure 3.11 are as follows:

1. The method achieves more than 95% accuracy in most image.

[4]The percentage of pixels in the image which were correctly classified.

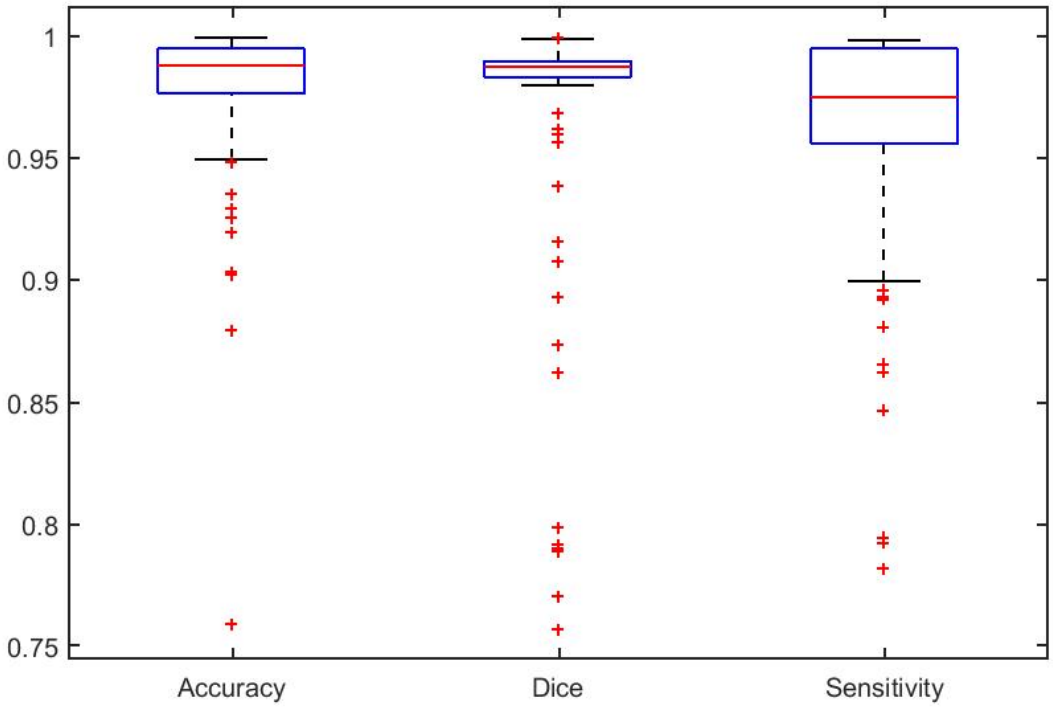

Figure 3.11: Box plot for values distribution of Accuracy, Dice coefficient and Sensitivity of RNFLT from Table 3.2.

2. The method obtain paths very close to the actual retinal boundaries by achieving a mean sensitivity of $\approx 97\%$ over 150 images, which portrays adaptability to contours of the retinal layers.

3. The distribution of the dice score from Figure 3.11 further attests to the statements in 2 above, i.e. there is a high overlap between the manual segmentation and results obtained by the method.

Furthermore, the proposed method achieves a dice coefficient (STD) of 0.9746 ($\pm$0.0559). This is a better performance Compared to algorithms reported in [22] with 0.903 ($\pm$.028) and RF+Graph [96] with 0.877 ($\pm$0.053). The method also outperforms the two algorithms N and C [103] with 0.900 ($\pm$0.027) and 0.903 ($\pm$0.026) respectively. However, it is noteworthy that the methods were tested on a larger dataset compared to the dataset used in the evaluation. Similarly, [67] utilised a larger dataset of 490 B-scan to evaluate the performance of the SNet and SNet + T-Net algorithms. The dice coefficient for the machine learning algorithms

were 0.898 and 0.904 for SNet and SNet + T-Net algorithms, respectively. Machine learning algorithms perform better with larger training dataset, which is a challenge as highlighted in [173].

Full automation of methods has to do mainly with the use of prior knowledge, enabling the use of a compromise to replace user input. For example, works presented in [27, 34] relies on the fact retinal layers spread across the image horizontally, which enabled the addition of two columns to either side of the image, such that the cut can traverse within these columns easily. Additionally, there has been increased interest around the performance of fully automatic and interactive methods of segmentation. From the study, we can infer that the performance can be traced to the use of prior knowledge e.g the brightness of the layers on OCT and unchanging layer locations. This observation can be confirmed by looking at the progression trend of segmentation methods. In the early days of computer vision, the interactive segmentation method, for example, [16] was proposed mainly to handle the challenges faced by automatic segmentation methods. However, recently, due to better insight and knowledge of the datasets and better imaging modalities, fully automatic methods are available, with performance similar or even better than semi-automatic methods.

3.5 Conclusion

Unlike other clinical data that are recorded usually with their inherent and abstract structure, medical images such as the OCT images are usually acquired in the large, raw format. This lack of structured and high-level information in retinal images has limited their potential in clinical practice and healthcare analytics. As a way forward, this chapter has presented a comprehensive and fully automatic method for segmentation of retinal layers in OCT images by integrating an advanced method of weight calculation into the graph-cut framework. The introduction of stabiliser enables the method to adapt to intensity inhomogeneity of OCT images in the preprocessing step, while the reassignment of weight aids the method in avoiding wrong paths, which consequently improves the accuracy of the method in identifying actual layer boundaries. The method is capable of segmenting seven retinal layers with eight boundaries.

The core of the method is a Graph-Cut segmentation using Dijkstra's algorithm [32]. More importantly, the adjacency matrices from vertical gradients and a sequential process of segmentation, as two critical elements of the study, are integrated into the Graph-Cut framework. The proposed method was evaluated on a dataset of 150 OCT images, with promising segmentation results. Further quantitative evaluation indicates that the segmentation measurement is very close to the ground-truth. The main contributions of this work are as follows:

1. This chapter has presented a method to identify seven retinal layers across eight layer boundaries automatically, so far one of the most comprehensive studies in this area;

2. The adjacency matrices are effectively integrated into the Graph-Cut framework with better weight calculation;

3. Based on the unique characteristics of reflectivity of different retinal layers and their changes across layers, a sequential process of segmentation has been developed.

Moreover, it is evident that the use of prior knowledge has the potential to improve segmentation algorithms. Having automatic methods that could extract this knowledge will play a vital role in how OCT image analysis evolves. This method addresses the need for algorithmic frameworks that could be adapted to large applications of OCT images. Also, continuously integrating images with EHR will be an ideal way to progress towards personalised healthcare. In summary, promising experimental results have been achieved, but the segmentation of the less prominent layers depends on the accuracy of the more prominent layers. This sequential process affects the segmentation of the less prominent layers. Therefore simultaneous segmentation might improve the results of the segmentation. Consequently, a level set method to segment seven layers from an OCT image simultaneously is explored in the next chapter.

Chapter 4

Level Set Segmentation

This chapter presents a simultaneous method for segmenting retinal layers in OCT images using a level set method. The method starts by establishing a specific Region of interest, which is vital in the segmentation process. This is because the evolution of contours in the level set method depends on forces derived from the contour and image characteristics. Hence, if this evolution is solely based on the real feature of the layers and image under observation, without the interference of background noise, the performance of the method will be improved. The method segments seven layers simultaneously by constraining the evolution of the layer boundaries based on the layers topology in the OCT image.

4.1 Introduction

Current research in retinal OCT segmentation focuses on improving various aspects ranging from computational time, the number of layers segmented, use of prior knowledge and computational complexity to mention a few. In general, segmentation is partitioning based on some image characteristics. How these characteristics are defined determines the computation burden of the algorithm. In some cases, this computational burden is reduced through dynamic programming [27] or topology modification [103]. The number of questions (conditions) an algorithm has to check or satisfy is, therefore, a crucial factor. Some previous works in OCT segmentation include the Markov Boundary Model [93], which was later extended by

[14], geodesic distance [41], level sets [126, 165], graph-based methods [27, 34, 39, 53], and recently machine learning [96]. Taking the level set method, although the method has automatic topological handling, the steps can be computationally expensive [151], while adding complex constraints in the segmentation process usually increases the complexity of an algorithm. This chapter presents a method to handle this challenge by incorporating a simple yet efficient topological constraint to the evolution process of the level set method.

Particularly, the method proposed in this chapter is based on the following considerations: 1. The edges from image gradients are used to initialise curves in order to handle under-segmentation and over-segmentation of the image; 2. The evolution of a curve is explicitly based on layer arrangements and implicitly based on OCT topology. This means for each image the initial contours are specific to the image under investigation, while the forces in the normal direction and the topology constrains guide the contours towards layer boundaries.

The method segments an OCT image into 7 segments, relating to Nerve Fibre Layer (NFL); Ganglion Cell Layer + Inner Plexiform Layer + Inner Nuclear Layer (GCL+IPL+INL); Outer Plexiform Layer (OPL); Outer Nuclear Layer to Inner Segment (ONL+IS), Outer Segment (OS) and Retinal Pigment Epithelium (RPE). Locations of these layers on an OCT image are shown in Figure 4.1. The rest of the chapter is organised as follows. Section 4.2 discusses the proposed method in details. Experimental results and discussions are treated in Section 4.3. Finally, conclusions are drawn in Section 4.4.

4.2 Methods

This section describes the level set approach for segmenting retinal OCT images. A schematic representation of the method is illustrated in Figure 4.2, and details of each step are elaborated in the ensuing subsections.

4.2.1 Preprocessing

The preprocessing steps are illustrated in Figure 4.3. Each OCT B-scan image I is first enhanced with a Gaussian filter to reduce the image noise. The layers targeted by this study

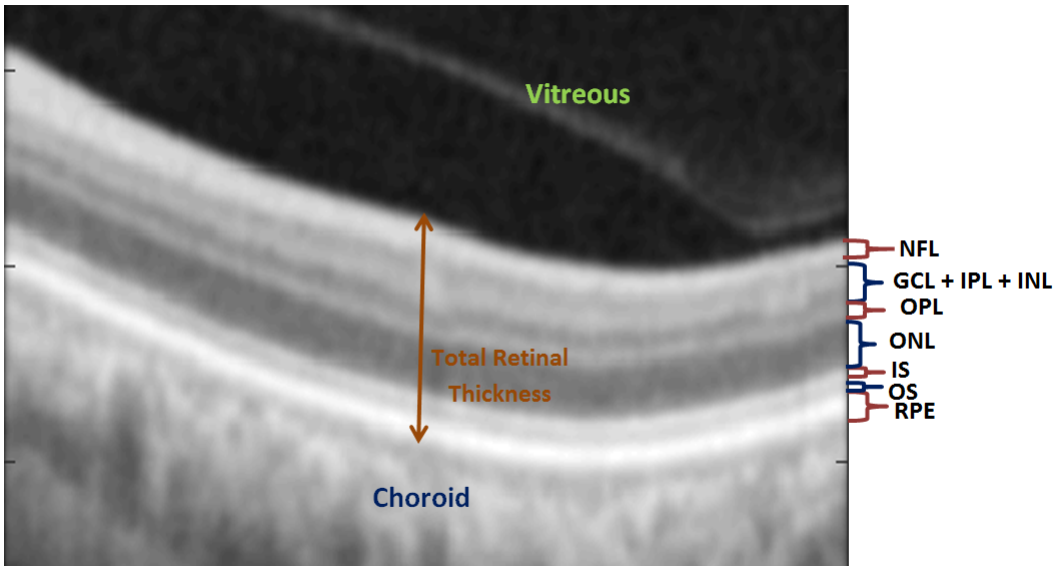

Figure 4.1: Location of Nerve Fibre Layer (NFL); Ganglion Cell Layer + Inner Plexiform Layer + Inner Nuclear Layer (GCL+IPL+INL); Outer Plexiform Layer (OPL); Outer Nuclear Layer to Inner Segment (ONL+IS), Outer Segment (OS) and Retinal Pigment Epithelium (RPE) on an OCT image as targeted in this chapter.

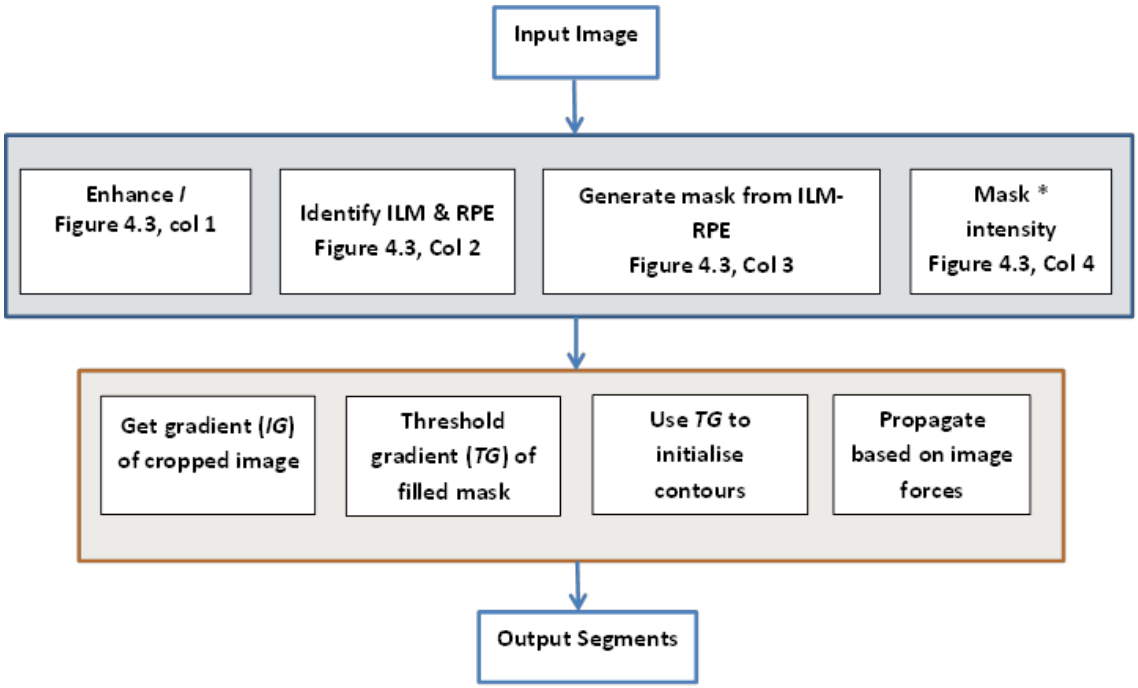

Figure 4.2: Schematic representation of the proposed level set approach.

lies within the total retinal thickness (TRT), which starts from the Internal Limiting Membrane (ILM) to the posterior boundary of the Retinal pigment epithelium (RPE), i.e. the boundary between the retinal nerve fibre layer and the vitreous, and the boundary between the RPE and the choroid regions respectively. It is commonly accepted that the NFL, IS-OS and RPE exhibits high reflectivity in an OCT image [27, 105, 156], based on experiments the ILM and RPE exhibits the highest transitions from dark-bright and bright-dark, respectively [34]. Based on this understanding of the retinal structure, the ILM and RPE are identified using the shortest path [32], by searching for the highest transitions on two separate adjacency matrices [27].

Using the identified ILM and RPE points the image is cropped to $I_{cropped}$, such that only the Region of interest (ROI) with useful layer information is remaining. This helps in dealing with layer-like structures outside the ROI and the computational cost associated with handling image background in segmentation. The pre-processing is vital in the segmentation process because only the actual layer properties impact the evolution of the curve. The next operation on the image is to generate a mask I_{mask} of the cropped image, and then multiply it by the original image I to get the intensity values within the mask. The examples of resulting images from this step are shown in figure 4.3, column 4, and expressed by the equation below:

$$I_{processed} = I_{mask} \times I \tag{4.1}$$

The process in this subsection is essential because only the layer structures are obtained when the gradient of the image is acquired. One of the significant roles of the preprocessing is to eliminate the need for handling background as depicted in figure 4.4 and further discussed in the next few subsections 4.2.2 and 4.2.3. The size of the cropped image is used to reduce computational time further and to eliminate the need for storing idle points [1]

[1] the pixels within the image that are produced when switching pixels between the lists during evolution.

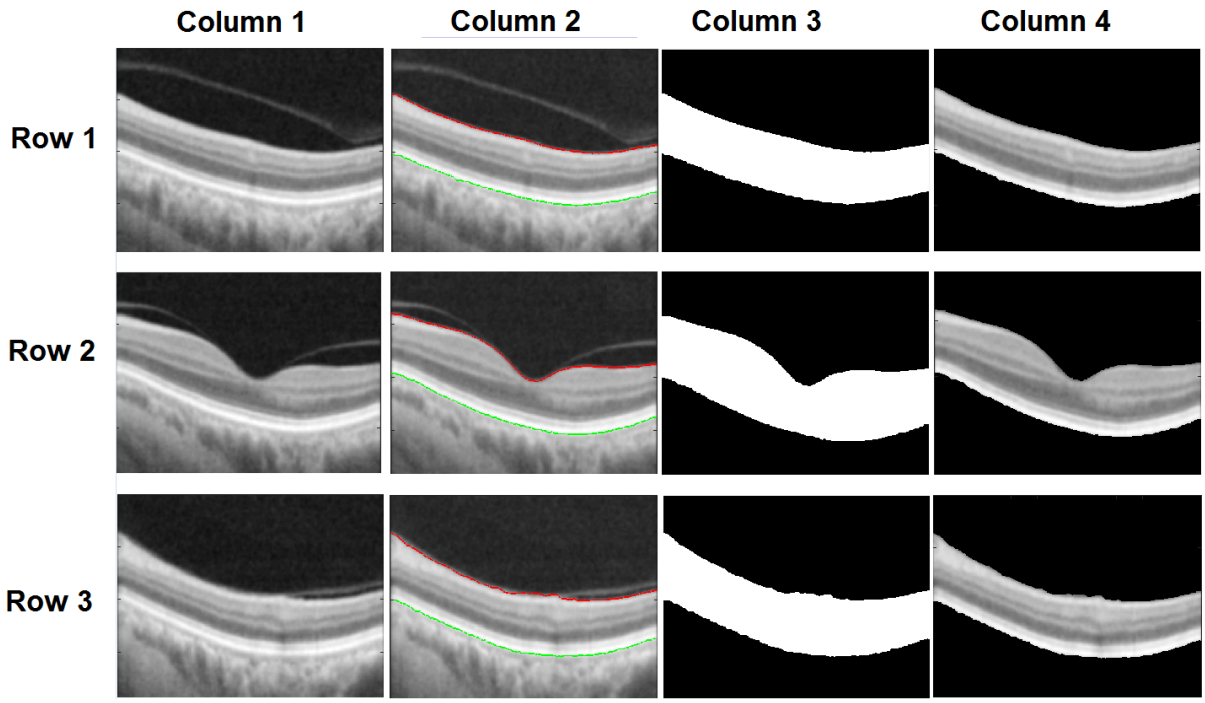

Figure 4.3: Preprocessing steps showing: Column 1 - Enhanced images; Column 2 - identified ILM (red) and RPE (Green); Column 3 - image masks I_{mask}; and Column 4 - Cropped images $I_{cropped}$. Row 1 - Nasal region; Row 2 - Foveal Region; and Row 3- Temporal Region.

4.2.2 Boundary Initialisation

To initialise contours of the level set method, the vertical gradient $\nabla I_{processed}$ of the processed image obtained and threshold by a constant T, in this case $T = 0.0018$. The edges of the thresholded gradient TG, is then refined to remove small objects from the image (most especially the GCL to IPL regions), such that only complete layers are initialised, figure 4.5. This is an essential factor, which further ensures accurate segmentation, i.e. only the initial curves are evolved, and no merging or splitting of boundaries is allowed. Without losing context, the refinement step can be ignored, if the layers from the GCL to INL are individual targets of the method. However, this will require a condition for handling the splitting and merging of boundaries or an alternate measure to correctly identify which layers are segmented. Moving further, the edges of the refined edges serve as initial curves such that the number of identified regions in the final output cannot exceed the number of the regions in TG. Therefore, each

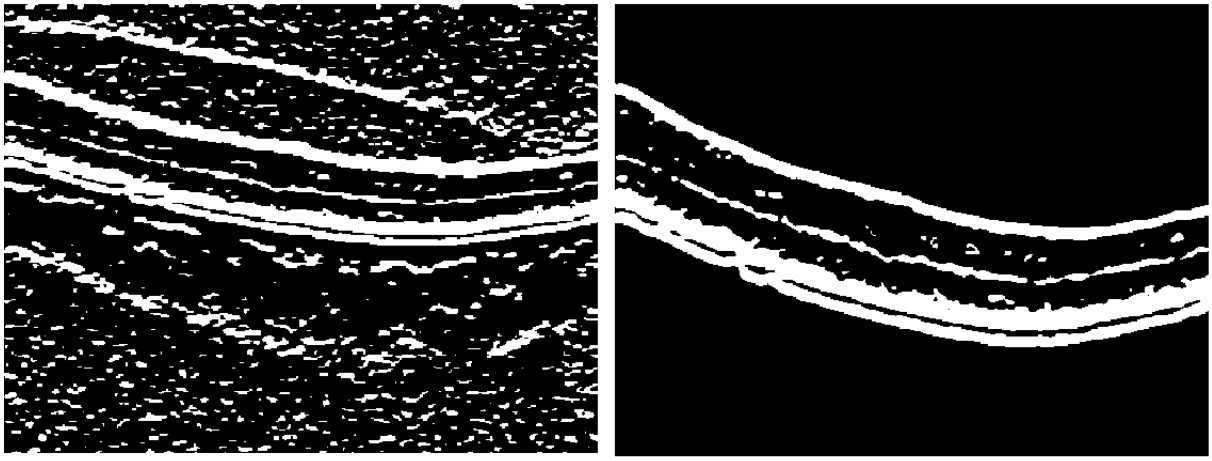

Figure 4.4: Gradient of full image with background with layer-like structures (a), and thresholded gradient of preprocessed image TG (thresholded by $T = 0.0018$) with ROI only (b).

boundary curve C_b is represented by a collection of $C_b(x, y)$ on the image.

4.2.3 Level Set Segmentation of OCT

We start by defining a level set function $\phi(x)$ at pixel x, where each point (x, y) in level set function is defined in relation to the curve C_b as follows [151]:

$$\phi(x,y) = \begin{cases} 3, & \text{if } x,y \text{ is outside } C_b \text{ and x, y} \notin L_{out}; \\ 1, & \text{if } x,y \in L_{out}; \\ -3, & \text{if } x,y \text{ is inside } C_b \text{ and } x,y \notin L_{in}; \\ -1, & \text{if } x,y \in L_{in}. \end{cases} \tag{4.2}$$

where L_{in} and L_{out} are two generated lists defining points inside and outside of C_b, respectively. Adapting from [151] the lists are defined as:

$$L_{out} = \{x | \phi(x) > 0 \text{ and } \exists y \in N(x) : \phi(y) < 0\}$$
$$L_{in} = \{x | \phi(x) < 0 \textit{ and } \exists y \in N(x) \text{: } \phi(y) > 0\}$$

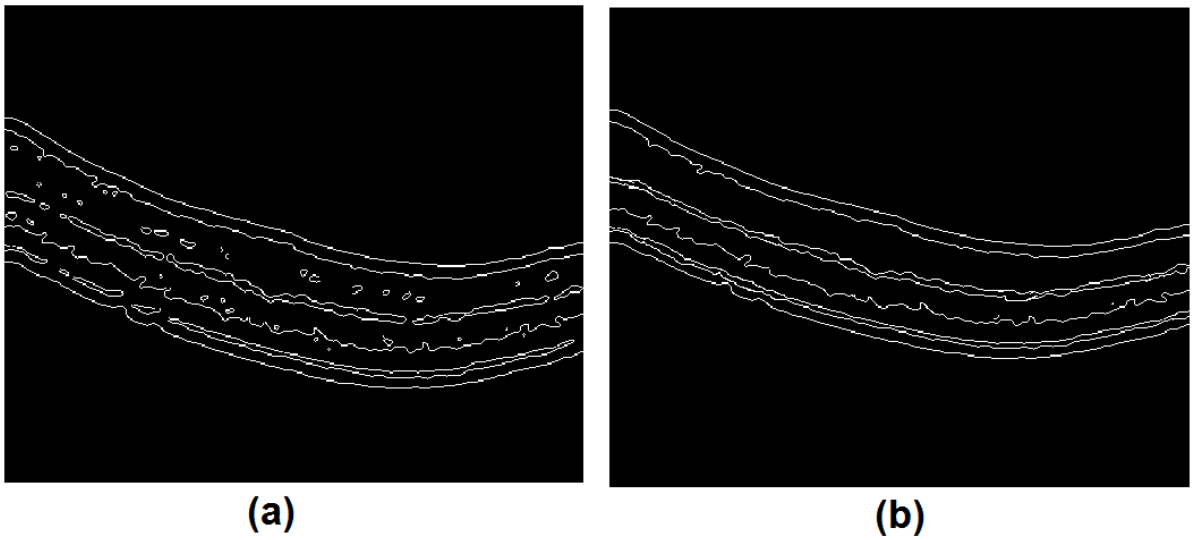

Figure 4.5: Edges before refinement (a), and refined edges used for contour initialisation (b).

where $N(x)$ is a distinct neighbourhood of x, We use a 2D list to represent boundaries, to save the positions for easy mapping in generating the final image output. Alternatively, a 1-D list can be used to capture the boundaries at position $\phi(x)$, as suggested in [103].

Based on the above representations, a boundary position $C_b(x, y)$ of $\phi(x, y)$, can either expand or shrink based on:

$$\begin{cases} \text{Expand}(x,y): & C_b(x,y) := C_b(x,y) + 1 \\ \text{Shrink}(x,y): & C_b(x,y) := C_b(x,y) - 1 \end{cases} \tag{4.3}$$

Next, each initial boundary curve C_b is evolved depending on a speed field F based on the following differential equation [151] :

$$\frac{dC_b}{dt} = F\vec{N} \tag{4.4}$$

Where $\vec{N} = \nabla\phi$ is the normal of the curve pointing outward. The speed field F is made of an external speed derived from the image data and a characteristic speed based on C_b [98]. The evolution is therefore associated with a gradient descent solution. This means a boundary C_b will evolve until it gets to a minimum of the energy C_{bmin}, i.e. a static point

of the dynamic equation (4.4). The curve C_{bmin}, at such stationary points, must satisfy two optimality conditions: one for continuity and the second for discontinuity regarding the speed field F. In summary, the evolution of each point is influenced by various forces (equation (4.4)) and the topology constrains to be described in the next subsection 4.2.4.

4.2.4 Topology Constrains

As highlighted earlier in subsection 4.2.1 the ordering of the layers must be preserved. Taking into account the architecture of the OCT image, boundary C_{b2} is always below C_{b1} for any given boundary points C_{b1} and C_{b2}, i.e. a point $C_b(x, y)$ on the curve will neither Shrink nor Expand if $C_{b1}(x, y) \leq C_{b2}(x, y)$. Hence, with the appropriate initialisation, we enforce the topology requirement by carrying out this simple topology validation before either shrinking or expanding a boundary. Finally, we employ an intuitive approach to ensure this topology is preserved, by additionally refining the topology constraint in the vertical direction:

1. Because each layer boundary spans the image horizontally (one boundary point per column) we add a condition for evolving a boundary point $C_b(x, y)$ to a new boundary point $C_{bmin}(x, y)$. We restrict $Expand(x, y)$ if its neighbour points are u consecutive points above it; do not $Shrink(x, y)$ if its neighbour points are u consecutive points below it;

2. Looking at the sample of initial layer boundaries in figure 4.5, a boundary point $C_b(x, y)$ is limited to a maximum of v operations (either $Expand$ or $Shrink$) consecutively in the vertical direction).

The parameters u and v are two prior constants, in the experiments u and v are set to 3 and 20 respectively. The parameter u aids with boundary smoothness and avoiding peaks for $Expand(x, y)$ or valleys $Shrink(x, y)$ on the boundaries, while v further ensures the layered architecture is preserved. Additionally, this is why the layer initialisation is ideal because the starting points are based on the individual image. The topology constraints facilitate the evolution because the validation is performed before expanding or shrinking a boundary. Perhaps, this might not be ideal for abnormal structures. However, considering the ordering

of the layers where C_{b2} will always be below C_{b1} the layers will move together even in the case of abnormal retinal structure.

4.3 Results and Discussion

The same dataset as chapter 3 is used for evaluating the performance of the proposed method. However, 200 images are used in this chapter, as opposed to 150 in the previous chapter because more ground truth labellings were acquired. In the experiments, $N(x) = 8$, i.e 8 neighbouring pixels, mainly, because only the layers are remaining in the cropped image and the effect of inhomogeneity is reduced. Experimental results show that the method successfully segments seven layers of the retina. Samples of the method output are shown in figure 4.6.

The performance of the proposed method was compared to mean shift segmentation algorithm [29], which involves the repeated movement of data points to their sample means [51]. A B-scan image is typically a 2-dimensional lattice of r-dimensional vectors (pixels), where r is 1 in the grey level case, 3 for colour images or r >3 in the multispectral case. The space of the lattice is identified as the spatial domain while the grey level, colour, or spectral information is represented in the range domain. Nevertheless, after a proper normalization with σ_s and σ_r, global parameters in the spatial and range domains, the location and range vectors can be concatenated to get a spatial-range domain of dimension d = r+2 [29]. The evaluation was carried out using the mean shift algorithm [29] implemented by Vantigodi [161].

The algorithm requires three parameters, i.e σ_s, σ_r, and a threshold, M for pixels to be eliminated during computation. Moreover, σ_s has no significant effect on the segmentation results, while M facilitates convergence and influences the number of clusters as can be deduced from figures 4.7 and 4.8.

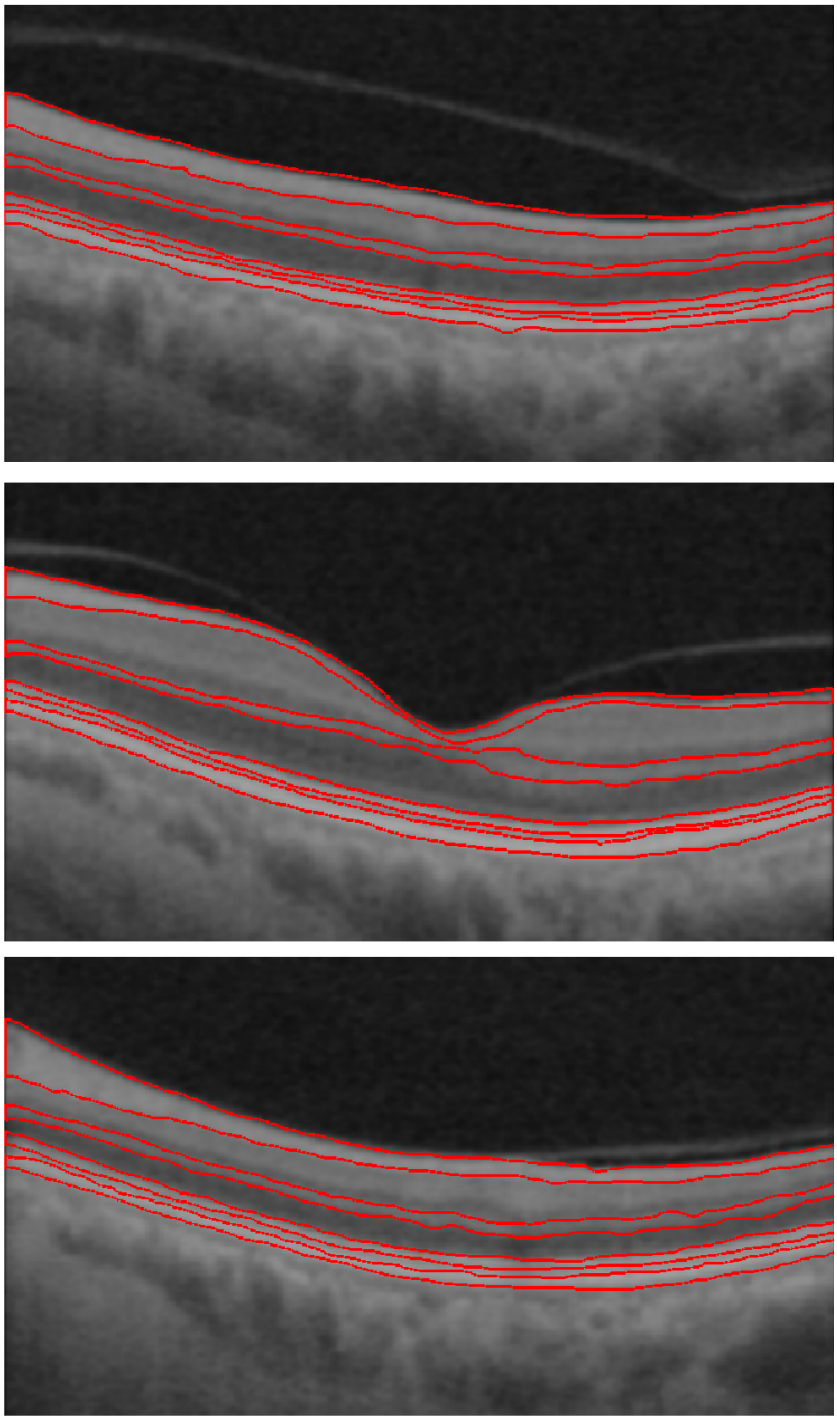

Figure 4.6: Results of Level Set Segmentation. From top to Bottom: Sample results from Nasal, Foveal and Temporal regions respectively.

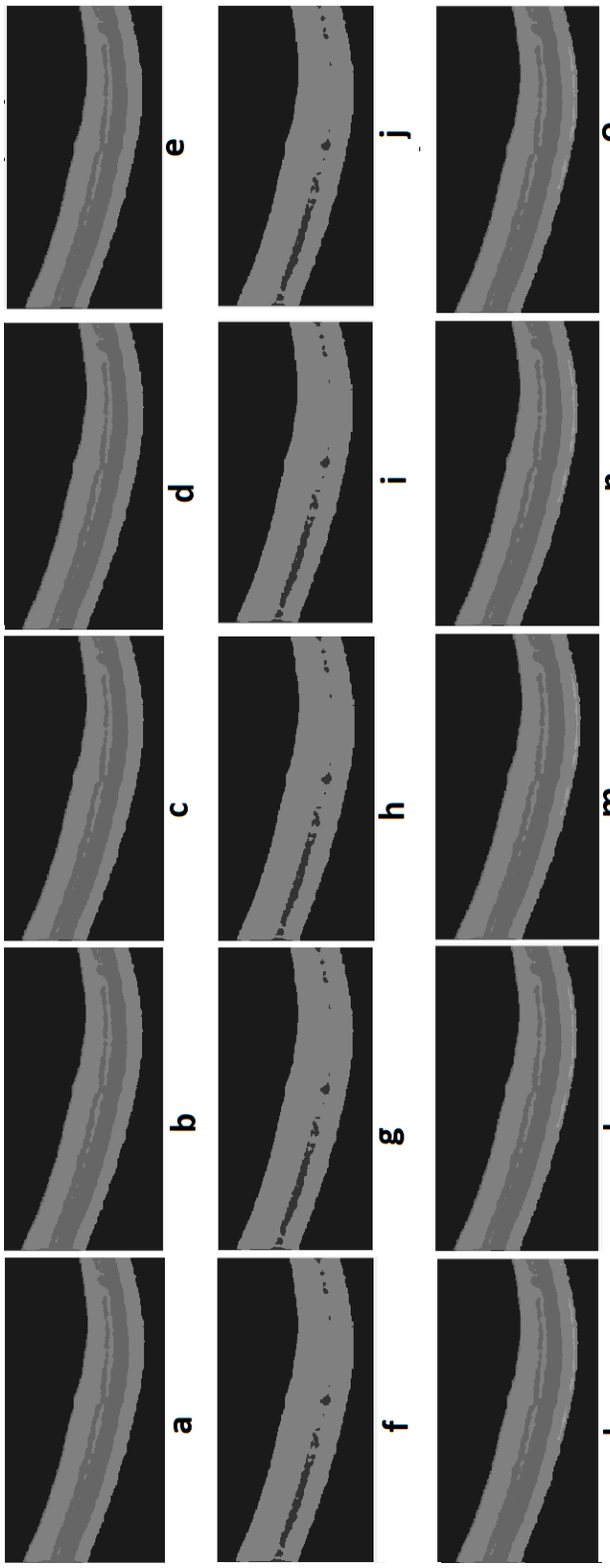

Figure 4.7: Mean shift segmentation results: (a - e) - fixed $\sigma_r = 1$, M =1, while σ_s = 10,20,30,40,50, respectively; (f -j) - fixed $\sigma_r = 2$, M =1, while σ_s = 10,20,30,40,50, respectively; (k - o) - fixed $\sigma_r = 1$, M =2, while σ_s = 10,20,30,40,50, respectively;

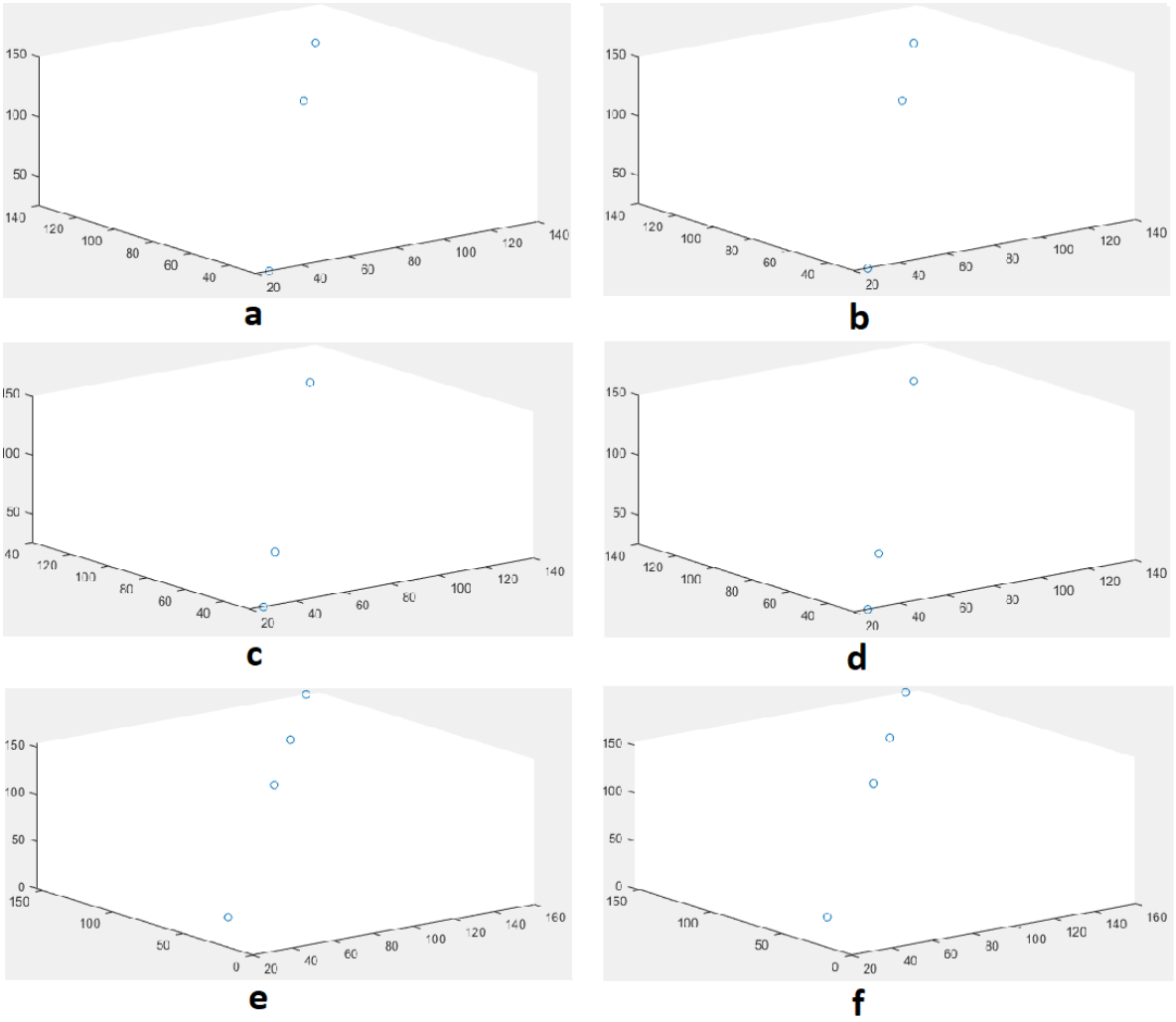

Figure 4.8: Colour distribution of mean shift segmentation results: a - figure 4.7a; b - figure 4.7b; c - figure 4.7f; d - figure 4.7g; e - figure 4.7k; f - figure 4.7l.

On the other hand better results are achieved with $\sigma_r = 3$ as shown in figure 4.9. Experiments with $\sigma_r = 4$ requires continuous tuning of the other parameters to achieve under-segmented images, whereas a blank image is returned as the segmentation result with value of $\sigma_r > 5$ (similar to value of 4). Hence in our experiments the value of $\sigma_r = 3$, while $\sigma_s = 40$ and $M = 3$.

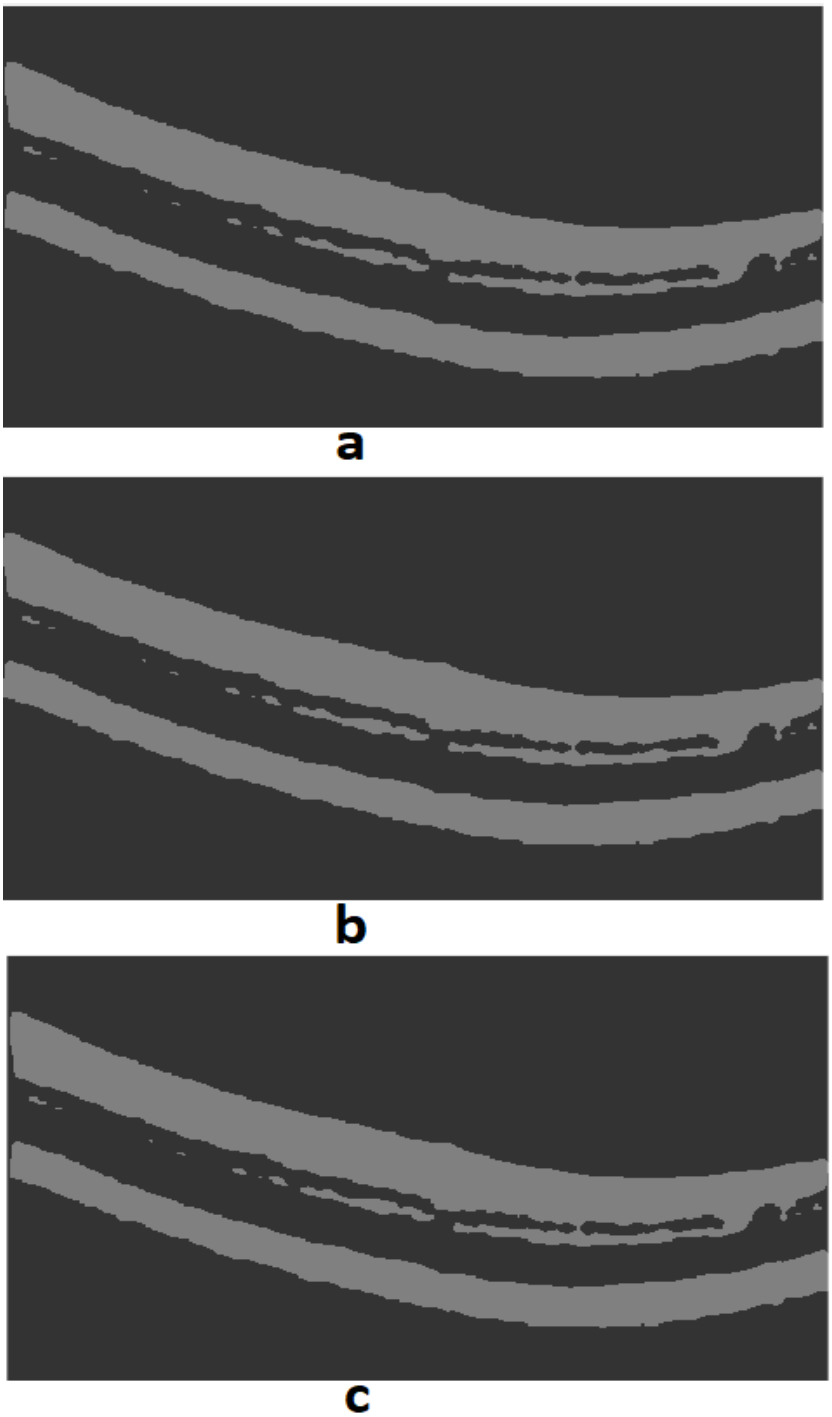

Figure 4.9: Mean shift segmentation result: a - $\sigma_r = 10$, $\sigma_s = 3$, $M = 1$; b - $\sigma_r = 30$, $\sigma_s = 3$, $M = 1$; c - $\sigma_r = 90$, $\sigma_s = 3$, $M = 1$

Table 4.1: Performance evaluation of proposed method and mean shift segmentation [29] showing mean (Standard Deviation) of Dice Coefficient on 200 B-Scan images (Units in pixels).

$RetinalLayer$	$ProposedMethod$	$MeanShift$ [29]
NFL	0.951 (± 0.022)	0.41 (± 3.2)
GCL+IPL+INL	0.879 (± 0.031)	-
OPL	0.892 (± 0.032)	-
ONL	0.907 (± 0.030)	-
IS	0.932 (± 0.017)	-
OS	0.920 (± 0.028)	-
RPE	0.934 (± 0.021)	0.53 (± 2.31)

Table 4.1 shows the mean and standard deviation for the performance of the proposed method and mean shift algorithm [161] compared to the labelling of manual graders. The proposed method outperforms the mean shift algorithm [29] in terms of the evaluation matrices and number of layers successfully segmented. Mean shift is able to segment only two layers, which are over segmented as seen in figure 4.9. The values show the promising performance of the proposed method in converging at curves C_{bmin} very close to the actual layer boundaries. Notably, the RNL thickness is used for diagnosing major eye diseases such as glaucoma, and the mean (0.951) and standard deviation (±0.022) of dice coefficient for this layer is reassuring. Moreover, it can be deduced that the method is consistent in identifying the layer boundaries from the distribution of the values in figure 4.10. Considering the second quartiles of the NFL, IS and RPE begin at ≥ 0.900 further attests to the good performance of the method, except for few instances in the GCL+IPL+INL and OPL layers, where the dice score is below 0.800.

4.4 Conclusion

This chapter has presented a fully automated and simultaneous level set method for retinal OCT segmentation. The proposed method separates retinal OCT images into seven non-overlapping layers. This approach has explored image segmentation using level set from the initialisation and evolution perspective. Specifically, the contributions of this chapter can be summarised as follows.

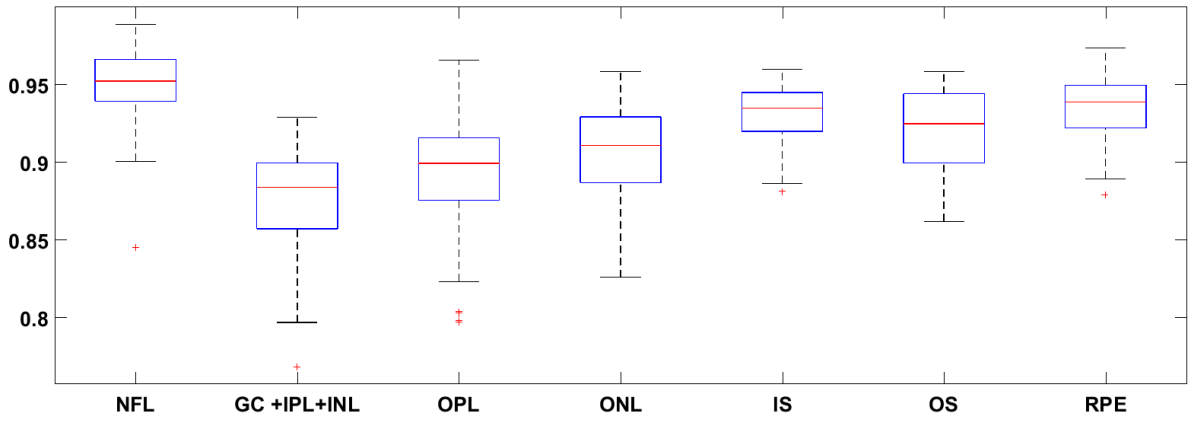

Figure 4.10: Box plot of mean Dice Coefficient distribution for the seven layers.

1. Based on the OCT image understanding, all image background is removed to aid in handling under- and over-segmentation.

2. An appropriate level set initialisation technique to ensure the initial contours for each layer and image are unique is proposed by using refined edges from gradient images.

3. Based on the topological architecture of the retinal layers in OCT, the evolution process is constrained to guide the initial curves to the actual layer boundaries.

The combination of these components ensure the boundaries obtained by the method are close to the true features of interest. Experimental results show that the proposed approach successfully segmented the target layers from OCT images, and the segmentation results are close to the manually labelled ground-truth.

Although constraints based on the layer topology aid in achieving good segmentation results as explored in this chapter and the previous (chapter 3), it may not be ideal for diseased images. Segmentation methods that do not heavily rely on the architecture of the layers might perform better. In the next chapter, we explore segmentation of OCT by modelling the method to cater for the inconsistency rather than heavily relying on the image features.

Chapter 5

Fuzzy Region Competition and Level Set Methods

This chapter presents a fully automated and simultaneous level set method for segmenting 9 retinal layers in OCT images. The method takes into account that although level set methods have a fundamental way of handling topological changes, the weak boundaries and noise in addition to inhomogeneity in OCT images make it difficult to segment the layers accurately. Similar to the previous chapter, the method establishes a specific region of interest. More importantly, inspired by the concept of region competition, fuzzy C-Means is used to select components of hyperreflective layers for initialisation. The clustering in the initialisation stage is also used to guide the evolution through; a Mumford-Shah (MS) selective region competition force and a Hamilton-Jacobi (HJ) balloon force . Finally, the convergence of the method is based on a HJ object indication function influenced by fuzzy membership to prevent leakages at weak boundaries.

5.1 Introduction

Segmentation is one of the most vital steps in computer vision, as it facilitates the delineation of various objects or Regions of interest (ROI) within an image. One of the inherent problems of existing methods for OCT analysis is the use of constants to represent inhomogeneous

or dynamic intensity values. Although the level set is appealing for its automatic topology handling [151], the performance of the level set method is subject to initialisation and configuration of controlling parameters [99]. Also, the implementation of zero level sets is based on partial differential equations that require reinitialisation [103], which are known for their computational burden [151].

This study is inspired by the work of [100], which illustrates the possibility of combining the Hamilton-Jacobi (HJ) and Mumford-Shah (MS) level set methods to achieve better solutions. Hence, the proposed method avoids reinitialisation by regularising the evolution process. More importantly, we capitalise on the flexibility of the Fuzzy image processing to express prior knowledge of the OCT image to guide the segmentation process of a selective level set method. By utilising the prior knowledge in the initialisation, evolution and convergence steps, it ensures the segmentation processes are exclusively based on image features. This formulation is essential to allow the method to identify multiple layers simultaneously. It also improves the method's adaptability, rather than the limited window given by rigid methods that usually complicates the segmentation process.

The proposed method segments an OCT image into nine segments corresponding to Nerve Fibre Layer (NFL); Ganglion Cell Layer (GCL); Inner Plexiform Layer (IPL); Inner Nuclear Layer (INL); Outer Plexiform Layer (OPL); Outer Nuclear Layer (ONL); Inner Segment (IS); Outer Segment (OS) and Retinal Pigment Epithelium (RPE). Locations of these layers on an OCT image are shown in Figure 5.1. The rest of the chapter is organised as follows. Section 5.2 gives an overview of the two level set methods, while, Section 5.3 discusses the proposed method in details. Experimental results and discussions are treated in Section 5.4. Finally, we draw conclusions in Section 5.5.

5.2 Level Set Method

Segmentation using level set methods models an image as a closed interface that separates the image into regions. It labels pixels inside or outside the interface. This labelling in relation to

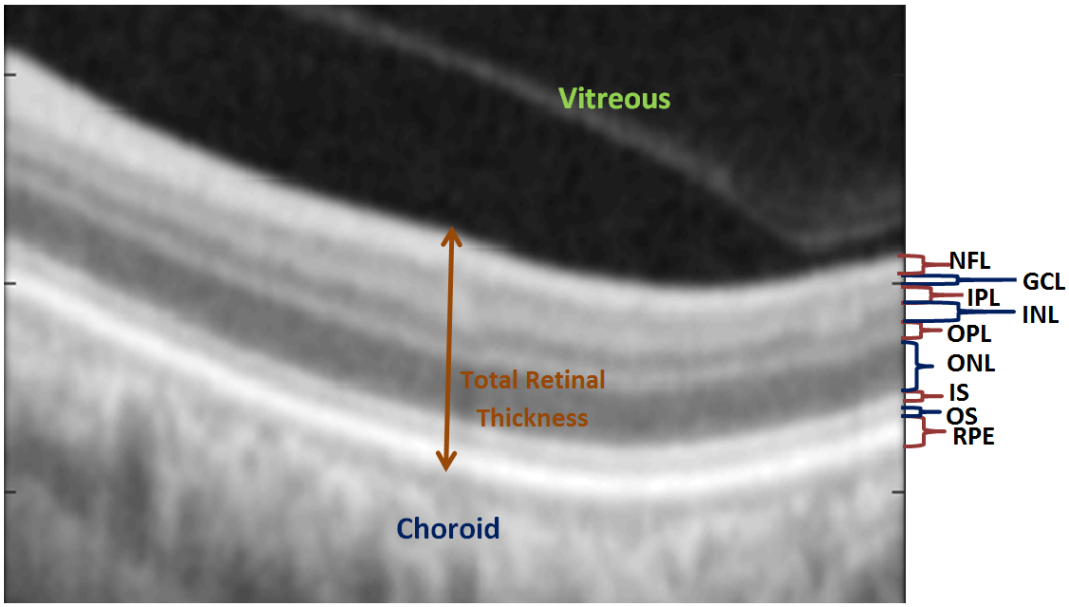

Figure 5.1: Location of Nerve Fibre Layer (NFL); Ganglion Cell Layer (GCL); Inner Plexiform Layer (IPL); Inner Nuclear Layer (INL); Outer Plexiform Layer (OPL); Outer Nuclear Layer (ONL); Inner Segment (IS); Outer Segment (OS); Retinal Pigment Epithelium (RPE) and total retinal thickness, on an OCT image. The brown colour is for the bright layers while blue colour is for the dark layers.

the interface is usually modelled into a higher dimensional space [100]:

$$\phi(x,y,t)\begin{cases} < 0 \quad if\ (x,y) \in \Omega^- \\ = 0 \quad if\ (x,y) \in \Phi \\ > 0 \quad if\ (x,y) \in \Omega^+, \end{cases} \tag{5.1}$$

where Φ is an interface that separates an image Ω. While Ω^- and Ω^+ denotes the sub-regions inside and outside Φ respectively. With this definition of the level set, it is easy to recover the interface by looking up points where $\phi(x,y,t) = 0$. Two formulations of the level set method have become the most prominent and have been improved in various ways. A common feature between them is that the interface evolves based on different forces derived from the interface and some image features. In particular, the classic Hamilton-Jacobi (HJ) evolves based on

forces, such as [128]:

$$\phi \begin{cases} \dfrac{\partial \phi}{\partial t} + \mathrm{F}\,|\nabla \phi| = 0 \\ \phi(x, y, t = 0) = \phi_0(x, y), \end{cases} \tag{5.2}$$

where $\nabla\phi$ denotes geometric gradient directing the normal interface evolution, and the term $\phi_0(x, y)$ specifies the initial contour. The speed field F comprises of intrinsic forces derived from the dynamic interface and external forces derived from the image characteristics. The force F could also include extra generated forces, such as balloon force [1]. Alternatively, the MS methods model the segmentation as [117]:

$$\begin{aligned} F(u, \Phi) =& \mu \cdot \mathrm{Length}(\Phi) + \lambda \int |\omega - u|^2 dxdy \\ &+ \int_{\Omega \setminus \Phi} |\nabla u|^2 \, dxdy, \end{aligned} \tag{5.3}$$

where u is a piecewise approximation of the regions inside and outside the interface, while μ and λ are coordinating parameters. This formulation aims to find an optimal interface by minimising a modified cost function. The improvements include incorporating the estimates of regional homogeneity, for example [24], which optimises the classic formulation (5.3). The MS methods are vulnerable to inhomogeneity, as such, various approaches have been proposed to mitigate this limitation, such as restricting local region competition or incorporating edge information. Extensive discussion of these mitigation strategies is however beyond the scope of this study. Therefore, further details on the advantages and limitations of both HJ and MS level set methods are obtainable from [23, 24, 99, 100, 117, 128, 151].

5.3 Methods

This section provides details of the fuzzy region competition and selective level set approach to segment OCT retinal images.

[1] The balloon force is one way to speed up curve evolution and influence its direction toward the region of interest [152]

5.3.1 Preprocessing

We start by preprocessing each image $\mathcal{I}$ to establish an explicit ROI [40], which supports further processing in the ensuing subsections. The layers commonly segmented on an OCT image are between the Internal Limiting Membrane (ILM) and the posterior boundary of the Retinal pigment epithelium (RPE). As such, the ILM and RPE are identified by delineating the two highest changes on two distinct adjacency matrices [27] using the Dijkstra's shortest path [32] as illustrated in Figure 5.2a.This is based on the understanding that the NFL, IS-OS and RPE are highly reflective in an OCT image [27, 105, 156]. Also, based on experiments the ILM and RPE exhibits the highest transitions from dark-bright and bright-dark, respectively [34].

The image is cropped to $\mathcal{I}_{cropped}$ using the identified ILM and RPE paths, after which, a mask $\mathcal{I}_{mask}$ of the cropped image is generated Figure 5.2b. Lastly, the image mask is multiplied by the original image $\mathcal{I}$ to obtain the original intensity values within the masked region. This operation is expressed by:

$$\mathcal{I}_{processed} = \mathcal{I}_{mask} * \mathcal{I} \tag{5.4}$$

The effect of the multiplication is shown in Figure 5.2c. The steps we employ in pre-processing the image are essential for robust segmentation. This is because only layer characteristics, are used in the clustering, and have an impact on the evolution.

5.3.2 Initialisation

With the established RIO, two dominating intensities exist, which corresponds to the hyper-reflective and hypo-reflective layers of the retina. Considering the inhomogeneity and incompleteness of layer intensity values within an OCT image, FCM provides a measure with which we can handle this problem [100]. The initialisation of the level set is by minimising a predefined function expressed by:

$$F = \sum_x \sum_y \sum_{k=1}^{K} \mu_k^l(x,y) \left\| \zeta(x,y) - \nu_k \right\|^2 \tag{5.5}$$

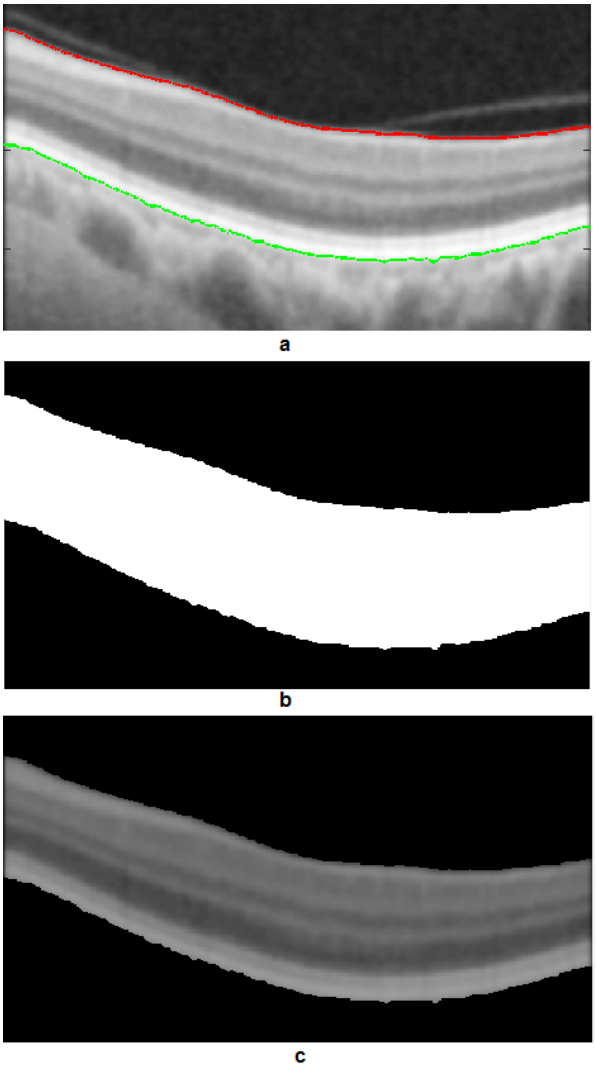

Figure 5.2: Preprocessing steps showing: a - identified ILM (red) and RPE (Green); b - image mask $\mathcal{I}_{mask}$; and c - processed images $\mathcal{I}_{processed}$. NB: black background included for better visualisation in images b and c 4.

where $\zeta(x, y)$ refers to the image intensity used as clustering trait and $\|\|$ is the Euclidean distance. The terms ν_k and $\mu_k(x, y)$ denote the estimated centroid of each cluster and the probability of each component belonging to a particular cluster, respectively. These terms are adaptively estimated using fuzzy clustering by:

$$\mu_k(x,y) = \frac{\sum_{n=1}^{K} \|\zeta(x,y) - \nu_n\|^{2/(l-1)}}{\|\zeta(x,y) - \nu_k\|^{2/(l-1)}}; \tag{5.6}$$

$$\nu_k(x,y) = \frac{\sum_x \sum_y \mu_k^l(x,y)\zeta(x,y)}{\sum_x \sum_y \mu_k^l(x,y)}, \tag{5.7}$$

The parameter l is >1 and controls the fuzziness of segmentation. Although l may be set as a constant, for example [100], we compute l using fuzzy histogram hyperbolisation [159] to fully utilise the ability of fuzzy image processing in handling uncertainties. As such, the value of l will vary between:

$$l = \begin{cases} l = \beta \\ l = \beta_{min} \qquad if \quad l < \beta_{min} \\ l = \beta_{max} \qquad if \quad l > \beta_{max}, \end{cases} \tag{5.8}$$

where β is the fuzzy membership value from [159] and β_{min} and β_{max} are two customisable priors constraining the value of l to achieve the desired transformation. This transformation optimises the segmentation performance because the intensities of image pixels close to their centroid are assigned high membership values, while those that are distinct are assigned low values. The outcome from 5.5 $\{\ \mu_k(x,y)|k = 1, 2, \ldots K\ \}$ is the possibility of each image pixel belonging to a specific fuzzy cluster ν_k. However, at this point, we are unsure of which cluster refers to the hyper-reflective layers, therefore, we threshold the outcome of the clustering to select a subset by,

$$\phi_0 = 2\left(\sum \frac{\mu_s + \nabla(\mu_s)}{2} > \theta\right) - 1, \tag{5.9}$$

which refers to the average of selected components μ_s and their gradient $\nabla(\mu_s)$ thresholded by the parameter θ to get the hyper-reflective layers. The selected hyper-reflective pixels are used for initialisation, based on the fact that a bright layer is always above a dark layer in an

OCT. The term μ_s is derived from

$$\phi_0 = 2([\upsilon_s] > \theta) - 1, \tag{5.10}$$

where θ ranges between 0 and 1, and $[\upsilon_s]$ denotes a subset originating from $\phi_0 = 2(\mu_k > \theta) - 1$. Specifically, $\{\ \upsilon_s | s \in S \quad and \quad S \subset K\}$. The level set ϕ_0 is initialised based on (5.9). The selection of the subset enables the method to evolve near the layer boundaries, which aids in better segmentation. Additionally, averaging the selected components and their gradient information allows the method to differentiate the segmented layers in the final output effectively.

5.3.3 Evolution

The evolution of the level set method determines how the interface arrives at what is perceived to be the optimal solution. The MS and HJ level set methods employ different forces to guide their evolution towards the desired optimum. Notably, the evolution of MS methods is based on the force of region competition. To prevent intensity inhomogeneity from governing the evolution process, as with classic MS methods [23], a selective region competition term is employed;

$$\mathrm{R} = \sum\nolimits_{s \in S} \mu_s - \sum\nolimits_{(j \in K) \cap (j \notin S)} \mu_j, \tag{5.11}$$

where μ_s denotes the selected components of fuzzy clustering, and μ_j denotes the unselected components. Clearly this implies $\mu_s \cup \mu_j = K$ for completeness of segmentation. The product of the fuzzy region competition force, R, varies between 1 and -1, and the boundaries will expand or shrink based on the sign of the force. This formulation allows the method to track local objects and facilitates simultaneous segmentation of multiple layers based on their distinct local properties.

On the other hand, a balloon force that capitalises on the fuzzy clustering is utilised to steer the interfaces towards the layer boundaries adaptively [99]

$$\mathrm{G} = \left[1 - \gamma \left(2 \sum \mu_s - 1\right)\right] \sigma_0, \tag{5.12}$$

where the parameter γ, $(0 \leq \gamma \leq 1)$, is a controlling element of the balloon force σ_0. The controlling influence of γ is such that:

$$\begin{cases} \sigma_0 = constant & if \quad \gamma = 0, \\ \sigma_0 = \sum \mu_s & if \quad \gamma = 1. \end{cases} \tag{5.13}$$

In other words, σ_0 is regulated by the fuzzy membership μ_s otherwise constant, depending on the value of γ. The resultant balloon force from (5.13) consists of variables with pulling or pushing force at each pixel. As it were, the dynamic interfaces are lured towards the retinal layers, regardless of they are inside, outside or lying across the layer boundaries. This definition also aids in handling shortcomings of the wrong classification in the initialisation stage.

5.3.4 Convergence

One of the connate limitations of HJ methods for image segmentation is boundary leakage. As such, an improved object indication function [100] is utilised for robust convergence:

$$\mathrm{E} = e^{-\iota \max(\eta \cdot g_i,\, (1-\eta) g_\mu)}, \tag{5.14}$$

where the parameter η regulates the influence of various object indication functions, and the parameter ι ($\iota = 10$) is a constant used to reinforce the convergence process. The second term g_μ in 5.14 originates from the selected fuzzy membership functions μ_s, while the first term g_i is a normalised edge indicator based on image gradient.

$$g_i = \frac{g - \min(g)}{\max(g)}, \tag{5.15}$$

where g is derived from the convolution of the image Θ with a Gaussian kernel ω and is expressed as:

$$g = \frac{1}{1 + |\nabla(\Theta \circledast \omega)|^2}. \tag{5.16}$$

By taking advantage of the image information and fuzzy clustering, the object indication function is capable of finding optimal boundaries. Also, with this improvement, the method can handle leakage at weak layer boundaries, e.g. the GCL-IPL region.

5.3.5 Selective Level set Segmentation of Retinal Layers

The level set components (initialisation, evolution and convergence) explained in the previous subsections are integrated for selective level set segmentation of OCT image.

$$\Phi = \begin{cases} \dfrac{\partial \phi}{\partial t} = \delta(\phi)\left[\alpha \mathrm{E} \cdot \mathrm{G} + (1-\alpha)\mathrm{R}\right] \\ \phi(x, y, t = 0) = \phi_0(x, y), \end{cases} \tag{5.17}$$

where α is a controlling parameter regularising the effect of the MS and HJ force terms, R (5.11), and E $\cdot$ G (5.14) and (5.13), respectively. The parameter δ symbolises the Dirac function of the dynamic interface ϕ. To avoid re-initialisation and effectively regularise the dynamic interfaces we use the Gaussian smoothing [11]. Therefore, we conveniently advance the interface evolution by

$$\Phi = \begin{cases} \dfrac{\partial \phi}{\partial t} = \delta(\phi)\left[\alpha \mathrm{E} \cdot \mathrm{G} + (1-\alpha)\mathrm{R}\right] \\ \phi = \Theta \circledast \phi. \end{cases} \tag{5.18}$$

The method converges if the total energy (5.18) influenced by the object indication function (5.14) is less than or equal to a constant $\mathcal{C}$ or if the method reaches the maximum number of iterations.

Table 5.1: Mean and Standard Deviation (SD) of the method's Dice score Coefficient on 200 OCT retinal images (pixels).

RetinalLayer	*Mean*	*SD*
NFL	0.9292	± 0.034
GCL	0.8562	± 0.036
IPL	0.8689	± 0.031
INL	0.8881	± 0.033
OPL	0.8839	± 0.031
ONL	0.8987	± 0.041
IS	0.9081	± 0.030
OS	0.9149	± 0.027
RPE	0.9187	± 0.028
Total Retina	0.9643	± 0.014

5.4 Results and Discussion

The method was implemented using Matlab 2016a. We set the following parameters as; β_{min} = 1.8, β_{max} = 2.3, σ_0= 1.5, γ=0.5, η = 0.6, α = 0.5 and $\mathcal{C} = 10^{-4}$. The parameter θ = 0.6, because the target is the hyper-reflective layers. The method was evaluated on 200 OCT retinal images. The outcome of the experimental evaluation is shown in Table 5.1, and the distribution of values is shown in Figure 5.5. Sample outputs are shown in Figure 5.3 It can be deduced from the Dice average values in Table 5.1 the method is consistent in identifying the actual layer boundaries. By closely observing figure 5.3 (middle), figure 5.4 shows the proposed method avoids merging at the foveal region, which is a challenge in OCT segmentation. The total retinal thickness is an important marker to the performance of the method. It reinforces the concept of prepossessing, i.e. the correct boundaries are often identified, and no layer is missing in establishing the region of interest. there were some errors in the IS to RPE region. This primarily has to do with the reflection of blood vessels and the proximity. As such some pixels of the OS were wrongly classified and added to either the IS or RPE. Because the study is limited to OCT image segmentation, the methods in [99, 100] have broader applicability.

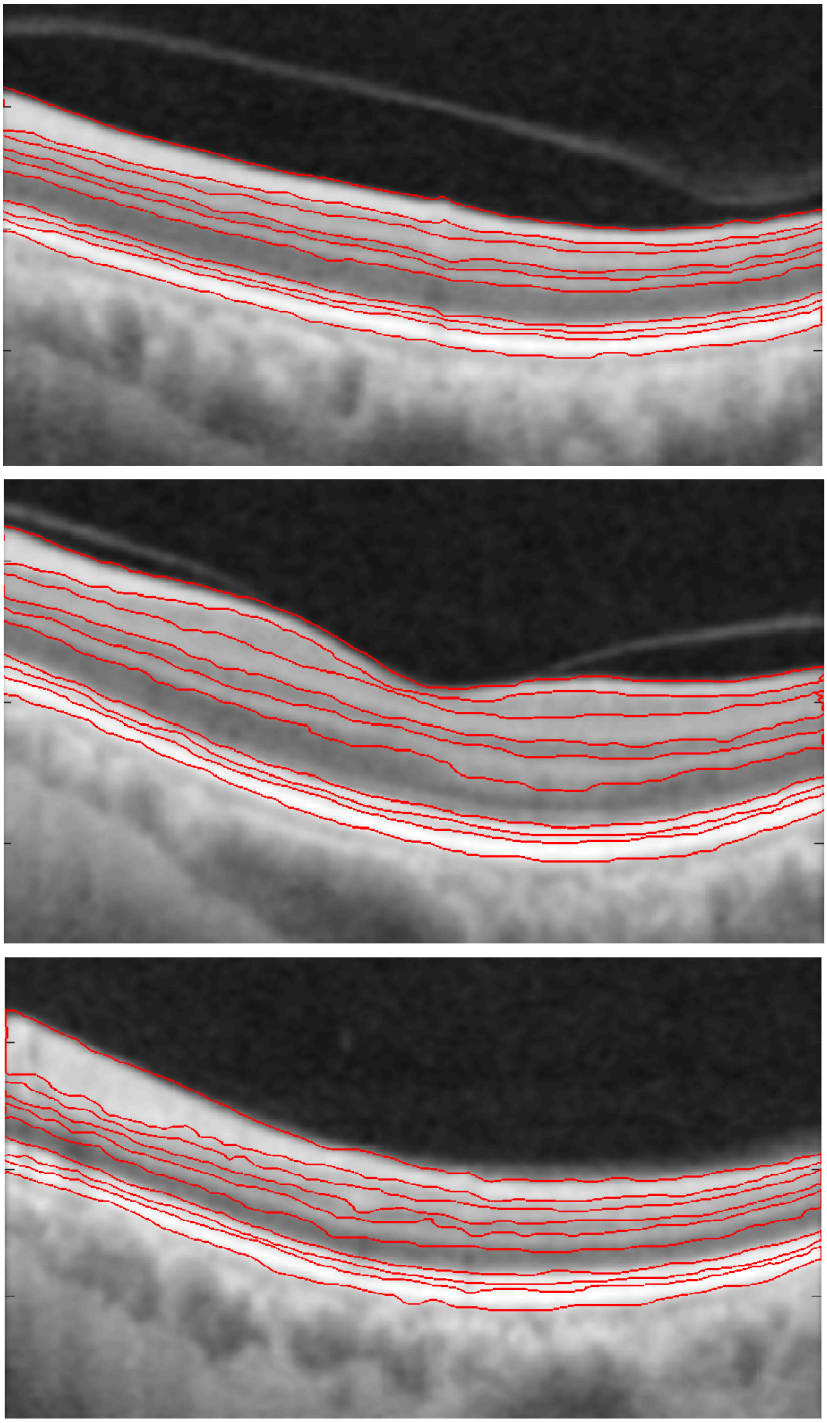

Figure 5.3: Results of Fuzzy Region Competition and Level Set Methods. From top to Bottom: Sample results from Nasal, Foveal and Temporal regions respectively.

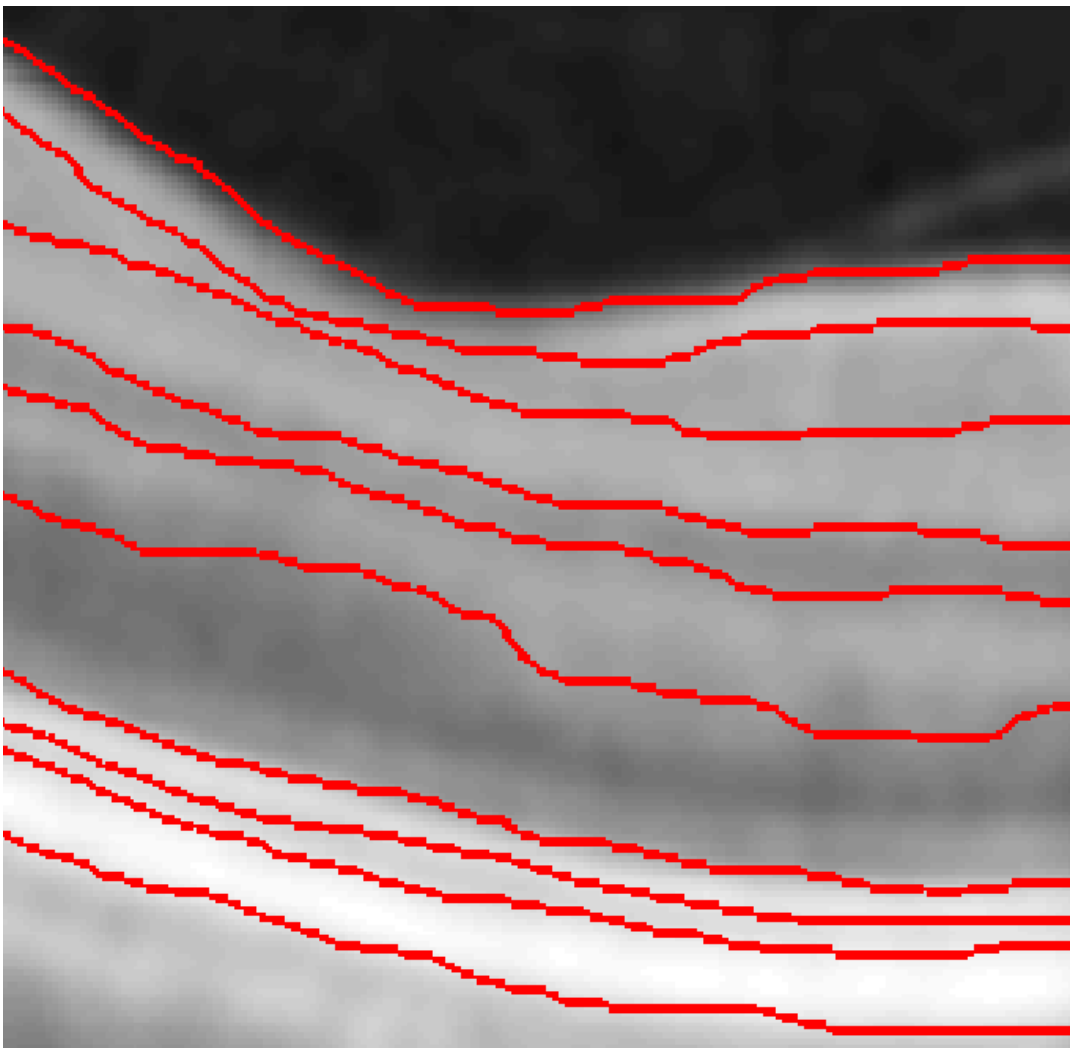

Figure 5.4: Zoomed view of figure 5.3 (middle).

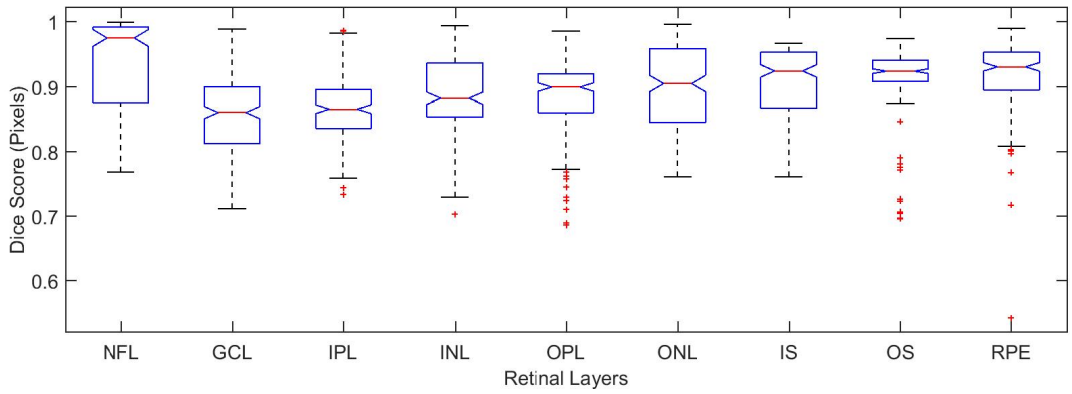

Figure 5.5: Box-plot of Dice Score for the nine retinal layers from Table 5.1.

5.5 Conclusion

The proposed method successfully segments the OCT image into nine non-overlapping layers. The method starts by establishing a specific ROI like the previous method (chapter 4). Notably, the idea behind using the preprocessing technique in this chapter is to isolate the hyper-reflective layers, which is essential for the level set segmentation process to achieve good results. The main contributions in the chapter can be summarised as follows:

1. Based on the OCT layer brightness, an exclusive subset of selected components corresponding to the hyper-reflective layers are selected for automatic and appropriate initialisation of the level set method.

2. The fuzzy membership function is incorporated into the level set method to adaptively guide the evolution of boundaries based on various image forces derived by combining the Hamilton-Jacobi and Mumford-Shah energy functions.

3. Also, the membership function is effectively integrated into the level set method to ensure robust convergence that is unique to each image without the need for adjustment.

Promising results makes the method suitable for OCT image segmentation, as it leverages the ability of FCM to handle inhomogeneity and incompleteness, which overcomes the shortcomings of OCT noise and inhomogeneity. On the other hand, although parameterisation improves the performance of most methods, it is still limited to values that need to be set manually.

Therefore, an approach for determining which method, MS or HJ, will perform better based on specific image feature will be ideal for segmentation, instead of the constant parameter $\mathcal{C}$.

Due to the promising results achieved using level set methods in chapters 4 and 5, we further explore simultaneous segmentation using the graph cut method in the next chapter. This will enable the assertion of the performance of the methods and the role of prior knowledge.

Chapter 6

Fuzzy Histogram Hyperbolization and Continuous Max-Flow

This chapter presents a method for simultaneous segmentation of OCT images using graph-cut method. The main idea behind this method is that if segmentation is based on differences and similarity, then we can find efficient computational techniques to improve these features. The method starts by establishing a distinct region of interest with all the crucial layer information, as the methods in chapters 4 and 5. It also, utilises the fuzzy C-means in a similar way to the method in Chapter 5. In addition to these, the main contributions of this chapter are as follows:

1. The transformation of the distinct ROI using fuzzy histogram hyperbolisation to improve the homogeneity within individual layers without distorting image information.

2. Building Graph-cut data terms by selecting the hyperreflective layers, which are efficiently integrated into an unsupervised continuous max-flow framework.

6.1 Introduction

Prevalence of the four major causes of blindness and visual impairments, which are age-related diseases [88], calls for efficient strategies and techniques for the prevention and treatment

of such diseases. Recent update by the World Health Organisation (WHO) highlights 285 million people worldwide fall victim of acute visual impairment and blindness [127, 181]. Older people from 50 years and above make up 65% of the visually impaired and 82% of the blind. Glaucoma, a disease that is known for its necessity of life long treatment, is lately estimated to account for 64.3 million people, a figure anticipated reaching 111.8 million by 2040 [155]. It is also projected that the number of victims people with Age-related macular degeneration (AMD), which is the third cause of blindness, will significantly rise from 196 million in 2020 to 288 million by 2040 [178]. With such overwhelming projection estimates, there is a need for robust computer-aided diagnostic (CAD) tools, should the aim to reduce this prevalence be achieved. Although the information provided by the OCT is useful, it requires further processing to extract clinically useful information. As such, segmentation is at the core of this image-based eye examination. Currently, manual segmentation is not only tedious but also impractical due to the volume and variety of data.

Owing to the motivation and challenges mentioned above, many computer-aided diagnostic (CAD) methods have been proposed to aid in OCT analysis with varying success rates. However, these methods are restrictive in their performance. Furthermore, OCT suffers from speckle noise, which causes difficulty in the precise identification of the boundaries of layers or other structural features either through direct observation or use of segmentation algorithms [115]. The noise that corrupts OCT images is non-Gaussian, multiplicative, and neighbourhood correlated. Thus, it cannot be easily suppressed by standard software denoising methods [111]. Previous attempts, including spatial and frequency compounding techniques, have been used to address the problem of speckle noise in OCT [78, 133]. However, these approaches can be too expensive to apply in practice in addition to technical issues beyond discussion in the context of this study. Additionally, digital post-processing, anisotropic diffusion filtering [45] and nonlinear anisotropic filtering [62], methods have been used for speckle noise suppression in OCT images. While these methods are effective in reducing noise, the image is either blurred or over smoothed due to loss of details (edges or lines) in non-homogeneous areas. Obviously, the purpose of pre-processing is to remove the noise without losing much detail in an image [145].

In this chapter, an efficient method for robust OCT image segmentation by utilising a combination of inexpensive methods is proposed. Distinctly, the method starts by establishing a well-defined region of interest with all the crucial layer information similar to chapters 4 and 5. The image is then transformed using fuzzy histogram hyperbolisation to improve the homogeneity within individual layers. Next, we cluster the intensity values of the transformed image into two clusters using fuzzy C-means. From the clustering outcome, we select pixels belonging to the hyperreflective layers by thresholding the average of selected components and their gradients by a parameter. These selected pixel's grey values are used to build data terms, which are integrated into an unsupervised continuous max-flow framework for computation of flow and optimisation. The method can successfully segment 5 layers of the retina in OCT images. Specifically, the layers are identified as: Nerve Fibre Layer (NFL); Ganglion Cell + Layer-Inner Plexiform + Inner Nuclear Layer Layer(GCL+IPL+INL); Outer Plexiform Layer (OPL); Outer Nuclear Layer (ONL); Inner Segment + Outer Segment + Retinal Pigment Epithelium (IS + + OS + RPE). The locations of these layers as segmented by the method in an OCT image are illustrated in Figure 6.1. This chapter is organised as follows. In section 6.2 we revisit the literature to provide insight into current studies. Section 6.3 provides details of the proposed method, while section 6.4 illustrates experimental results and accompanying discussions. Lastly, section 6.5 is reserved for concluding remarks.

6.2 Previous Works

Image segmentation is a process of partitioning an image into non-overlapping sub-regions which are similar with respect to some features such as pixel intensity or texture [129, 180]. The segmentation of retinal layers in OCT scans is not a trivial process due to the inhomogeneity, presence of vessels shadows and inherent speckle noise, variability and complexity of structures (i.e., macula, fovea and optic nerve) in pathological tissues. In recent years, several methods have been developed to detect, locate and segment different retinal layers (e.g. RNFL, GCL, IPL, etc) in OCT images [5, 6, 83, 97, 135, 139, 175]. These segmentations methods can be grouped into three main classes based on the dimensionality of the OCT images (i.e. 1D,

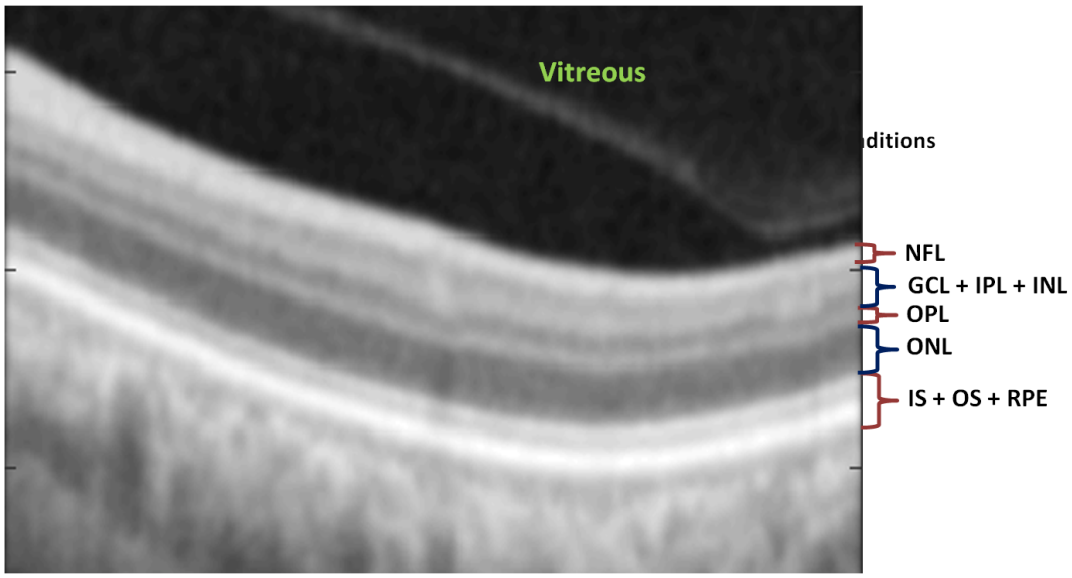

Figure 6.1: Illustration of the 5 retinal layers segmented in the study.

2D or 3D) [31]. However, the segmentation approaches of each group differ concerning the number of retinal layer features to be extracted like intra-retinal layers or fluid-filled regions in the retinal images [31].

Early segmentation methods of OCT images are based on features extraction from either conventional pixel intensity or gradient information. However, in the literature, most of the recent segmentation methods of OCT structures are based on more complex algorithms. The most popular methods include deformable-based approaches and graph-based techniques Deformable segmentation approaches such as level sets, active contours (snakes) and geodesic active contours use the regional characteristics or edge proprieties in the image to extract tissues in the OCT images. These models are either parametric or geometric depending on the contour characteristics because they perform the segmentation using a closed curve around the target tissue and execute an iterative operation. Methods such as level-set evolve toward the OCT tissues by searching in the scan either the largest gradient or using regional features in the image. A classical deformable – based retinal layers segmentation method is proposed in [174] by Yazdanpanah et al. The method adapts Chan-Vese's energy-minimising active contours using a multi-phase framework which incorporates a circular shape prior that model

the boundaries of the retinal layers in the OCT scan and estimate the shape constraints using least squares. In [170] Wang et al. proposed an automated segmentation method of intra-retinal layers in a high-resolution 3D SD-OCT images. The method combines a level set algorithm, hysteresis thresholding model and multi-region continuous max-flow algorithm to extract seven intra-retinal layers including NFL, GCL+IPL, INL, OPL, ONL+IS, OS and RPE. Dodo et. al, presented in [40] a level set segmentation method of seven intra-retinal layers. The method uses a region of interest and applies a gradient edges algorithm, which then use to initialise curves for the layers. The layer topology is used as a constraint in the algorithm evolution process. Although these deformable methods achieve good segmentation results, they need very robust pre-processing techniques to remove noise and imaging artefacts. They can produce poor results on heterogeneous images due to local minima. Often, the model's implementation can be complex as they use prior knowledge of the OCT image structures (i.e. pixel intensities, shapes, texture, colour, positions etc.) to define constraints on the algorithms evolution. These constraints could lead to segmentation inaccuracies when the methods are used to segment different OCT image modalities.

Like deformable segmentation approaches, graph-based methods use energy minimisation algorithms [15, 16, 19, 92]. They incorporate both regional and boundary regularisation proprieties in the same manner as Mumford-Shah [13, 131]. Among all the numerous energy optimisation approaches, graph cut techniques are one of the most popular methods used in OCT segmentation. The methods consist of separating a graph by a maximum flow or minimum cut optimisation algorithm [46, 148], in this model, the segmentation is performed using adjacency graph, which consists of a set of vertices (i.e. image pixels) and a set of weighted edges (i.e. weight values between two vertices) measuring the similarity between two neighbouring pixels. The segmentation is achieved by minimising a cost function which adds the values of the weights in the edges that are separated. In [34], Dodo et al. proposed an automated graph-cut segmentation method of retinal layers from OCT scans. This combines a fuzzy histogram hyperbolisation model and graph cut algorithm to segment eight (8) intra-retinal layers in high-resolution 3D SD-OCT images. Kaba et al. presented in [83] kernel graph cuts and continuous max-flow algorithm detect and segment the retinal layers including

ILM, RNFL-GCL and RPE from circular SD-OCT scans. The segmentation is performed by adopting a multi-regional graph cut segmentation technique, that includes a kernel-induced segmentation functional and a continuous multiplier based max-flow algorithm. In [6] Antony et al. proposed an automated globally optimal graph-theoretic method, which simultaneously performs the segmentation of retinal layers and the micro-cystic macular edema (MME) from volumetric OCT images.

These graph-based segmentations are very applicable in the segmentation of intra-retinal layers. They can incorporate prior information such as shapes, textures, sizes, pixels seeds and position into the graph energy algorithms guiding algorithm and achieving optimal segmentation results. While the graph-based methods generate good segmentation results, their performances depend highly both on the selection of initial seed pixels and the search parameters. Another drawback is finding the right cost functions of the graph functional that can distinguish individual tissue in the OCT the scans.

Recently, with the improvement in computing power and the availability of large volume of data, various retinal layer segmentations have been explored using deep neural networks [43, 68]. This has been very effective in medical image analysis tasks in general. A typical deep neural network for retinal layer segmentation was proposed in [43] by Fang et al. This segmentation method extracts nine (9) layer boundaries in OCT images of non-exudative AMD patients by combining both graph-cut search and deep neural network. In [68] He et al. presented a segmentation method of eight retinal layers in OCT images using a cascaded fully convolutional network (FCN) framework that guarantees the topological relationship between layers. Although deep neural networks methods achieve good results, they rely heavily on large datasets, and they are computationally expensive to perform. They are also sensitive to biases in the datasets, which can lead to segmentation errors when used in different datasets.

The method proposed in this chapter takes two significant things into account. Firstly, by establishing a defined region of interest, the chances of the algorithm finding features that are not of interest is highly reduced. Secondly, the OCT is well known for its intensity inhomogeneity; as such, using fuzzy c-means to handle the fuzzy nature of OCT is ideal. Also, using the FCM as opposed to constants in building data terms allows the method to adapt

to different images. Additionally, we capitalise on domain knowledge to reduce uncertainties in both the preprocessing and segmentation steps. Specifically, we transform the images to improve homogeneity and make each layer intensity values as similar as possible using the fuzzy histogram hyperbolisation. In the segmentation stage, we improve the graph energy function by incorporating selected components belonging to the hyper-reflective layers. This improvement enables the graph cut method to differentiate the source and sink without the need for user interaction.

6.3 Methods

This section details the proposed approach. A snapshot of the processes of the method is illustrated in Figure 6.2. The method consists of two main parts, which are detailed in the ensuing subsections.

6.3.1 Preprocessing

As highlighted in the previous sections (1 and 2) and also evident in the literature, noise affects the proper identification of features of interest and negatively impacts the performance of segmentation algorithms [111, 115]. As such, we start by establishing an explicit region of interest by cropping the original image I to a cropped image $I_{cropped}$ as illustrated in Figure 6.3. The cropping of the image is based on domain knowledge, which is always useful in any form of analysis. Specifically for OCT image, the commonly segmented layers are within the total retinal thickness (TRT), i.e. the boundary between the retinal nerve fibre layer and the vitreous, and the boundary between the RPE and the choroid regions. Additionally, it is commonly accepted that the NFL, IS-OS and RPE exhibits high reflectivity in an OCT image [27, 105, 156], and based on experiments the ILM and RPE exibits the highest transitions from dark-bright and bright-dark, respectively [34]. With these understanding of the retinal structure, we simply identify the ILM and RPE using the shortest path [32], by searching for the highest transitions on two separate adjacency matrices [27]. At this point it is fitting to crop the image I using the identified ILM and RPE points (Figure 6.1 C2) and then generate

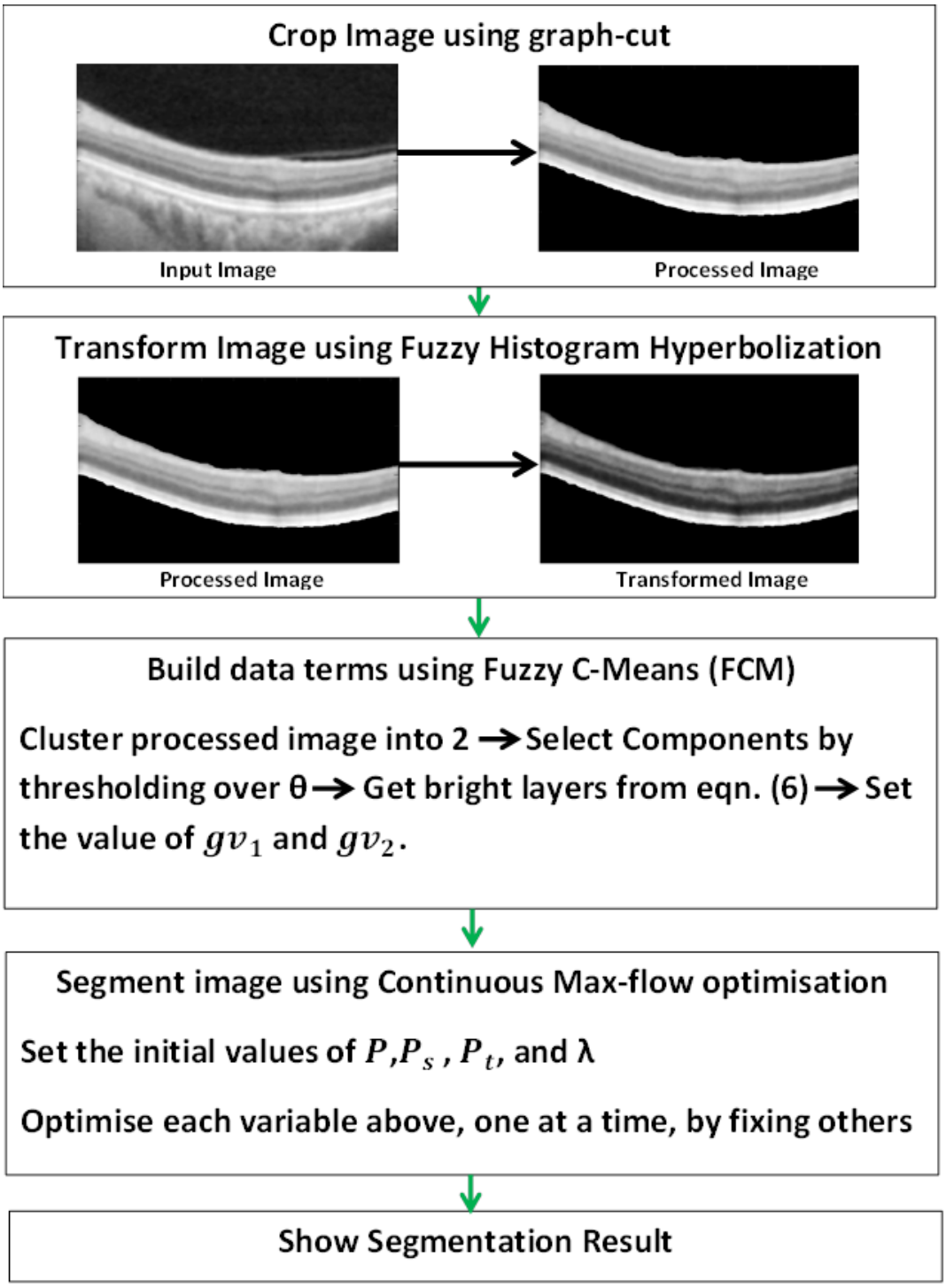

Figure 6.2: Schematic representation of the proposed OCT segmentation algorithm.

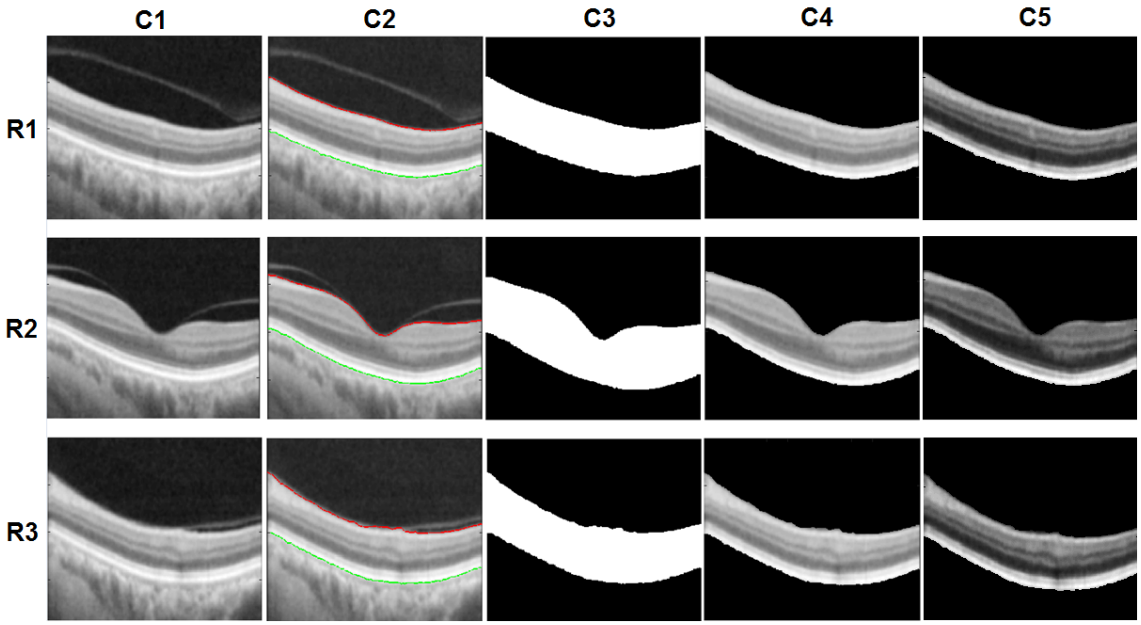

Figure 6.3: Preprocessing steps showing: R1 - Nasal region; R2 - Foveal Region; and R3- Temporal Region; C1 - Input images; C2 - identified ILM (red) and RPE (Green); C3 - image masks I_{mask}; C4 - Processed images $I_{processed}$; and C5 - Transformed images

a mask I_{mask} of the cropped image (Figure 6.1 C3). Lastly, we multiply the mask by the original image I to retrieve the pixel intensity values within the mask, which is expressed by the equation below:

$$I_{processed} = I_{mask} * I \tag{6.1}$$

The result from equation (6.1) is a processed image $I_{processed}$ containing part of the image with the layers information only as illustrated in Figure 6.3 C4. This process of cropping on its own improves the performance of the segmentation method because with the two dominating intensity values remaining, there is less interference of image noise. It also helps in dealing with layer-like structures outside the ROI and the computational cost associated with handling image background in segmentation.

Moreover, because of the intensity inhomogeneity within individual layers and across the image, we transform the processed image using fuzzy histogram hyperbolisation [158]. This transformation is such that bright layers get higher values and the value of the dark layers

becomes lower (Figure 6.1 (C5)), which enables the segmentation of seven layers as opposed to four layers in previous study [39]. It also further suppresses the image noise and make the intensity values within each layer as similar as possible, thereby differenciating it from the others. The pre-processing steps employed in the method is vital in the segmentation process as it enables computation of the flow strictly based on layer properties. It also allows us to utilise the full potential of the optimisation method, without having to employ complicated optimisation constraints that usually limit the method's performance.

6.3.2 Segmentation

Continuous max-flow unsupervised segmentation without user interaction utilises a piece-wise constant function to model the image, where two grey values gv_1 and gv_2 are chosen to build data terms [39, 179]:

$$C_s(x) = D(f(x) - gv_1(x)), C_t(x) = D(f(x) - gv_2(x)) \tag{6.2}$$

where $D(\cdot)$ is some penalty function. The problem with such formulation is that the distribution of values within the OCT is not equally distrubuted and fuzzy. In other words, the regions are inhomogeneous due to the incompleteness and fuzziness. Therefore, to compute the values of gv_1 and gv_2 it is convenient to employ FCM to cluster the image intensity values. This is because two main intensity values exist in the transformed image, which belong to either the bright or the dark layers. Consequently, we minimise a predefined function as in equation 5.5. The outcome from equation (5.5), $\{ \mu_k(x,y)|k = 1, 2, \dots K \}$, is possibility of each image pixel belonging to a specific fuzzy cluster ν_k. However, at this point, we are unsure of which cluster refers to the hyper-reflective layers, therefore, we threshold the outcome of the clustering to select a subset by,

$$GV = 2\left(\sum Avg(\mu_s + \nabla(\mu_s)) > \theta\right) - 1, \tag{6.3}$$

which refers to the average of selected components μ_s and their gradient $\nabla(\mu_s)$ thresholded by the parameter θ. The value of theta ranges between 0.5 to 1. This improves the probability

that the components selected actually belong the hyper-reflective layers. The term μ_s is derived from

$$GV = 2([\upsilon_s] > \theta) - 1, \tag{6.4}$$

where θ ranges between 0 and 1, and $[\upsilon_s]$ denotes a subset originating from $GV = 2(\mu_k > \theta) - 1$. Specifically, $\{\ \upsilon_s | s \in S \quad and \quad S \subset K\}$.

In summary, the flow will be based on the image under examination, as opposed to the chosen priors in equation (6.2). We set $gv_1(x) = GV$ (equation (6.3)), while $gv_2(x)$ is determined from the non-selected components. Averaging the selected components and their gradient enables assertion as to which cluster components belong to the bright layers. Likewise, the value of the hypo-reflective layers will also be as close to their relative values as possible.

By utilizing the augmented Lagrangian method [12], the max-flow function can be represented as follows:

$$\begin{aligned} Lc(P_s, P_t, P, \lambda) := \int_\Omega p_s dx + \int_\Omega \lambda(divp - p_s + p_t)dx \\ -\frac{c}{2}\|divp - p_s + p_t\|^2 \end{aligned} \tag{6.5}$$

Where λ is the Lagrangian multiplier introduced to optimise the flow and c is the steps in augmented Lagrangian.The spatial flow $p^*(x)$ is constrained, by imposing a condition in such a way that only saturated flows contribute to the total spatial flows and cuts, as follows:

$$C_{TV}^{\alpha} := \{p | \|p\|_\infty \leq \alpha, p_n | \partial\Omega = 0\} \tag{6.6}$$

where α is the penalty parameter to the total variation term $\partial\Omega$ and is constant throughout. In other words, at potential cut locations x $\in \Omega$ where $\nabla\lambda^*(x) \neq 0$ the spatial flow $p^*(x)$ is saturated, while at locations x $\in \Omega$ where $|p(x)| < \alpha$ is unsaturated we must have $\nabla\lambda^*(x) = 0$ and therefore the cut does not sever the spatial domain at x. This definition enables the optimisation of the flows and the labelling of potential cuts to be executed simultaneously. The various flows and the multiplier are optimised in an iterative process until convergence.

Putting everything together from equation (6.5) to begin the optimisation, we initiate the

values of $p_s^1 = min(C_s, C_t), p_t^1 = min(C_s, C_t), p^1 = 0, \lambda^1 = (C_s - C_t) > 0$, and then let k = 1 and start the k^{th} iteration,

- Optimizing p by fixing other variables

$$\begin{aligned} p^{k+1} &:= \arg \max_{\|p\|\infty \leq \alpha} Lc(p_s^k, p_t^k, p, \lambda^k). \\ &= \arg \max_{\|p\|\infty \leq \alpha} -\frac{c}{2}\|divp(x) - F^k\|^2 \end{aligned} \tag{6.7}$$

the sub-minimization problem (6.7) is solved by using a single step of the following iterative procedure computed by [179]:

$$p^{k+1} = \prod_{\alpha} p^k + c\nabla(divp^k - F^k) \tag{6.8}$$

where $\prod_\alpha$ is the convex projection onto the convex set $C_\alpha = q \mid\mid q \mid\mid \leq \alpha$ and F^k is a fixed variable. The term div is a positive divergence towards the sink, which ensures all incoming flow is to passed along since it is a directed graph.

- Optimizing p_s by fixing other variables

$$\begin{aligned} p_s^{k+1} &:= \arg \max_{p_s(x) \leq C_s(x)} Lc(p_s, p_t^k, p^{k+1}, \lambda^k) \\ &= \arg \max_{p_s(x) \leq C_s(x)} \int_\Omega p_s dx - \frac{c}{2}\|p_s - G^k\|^2 \end{aligned} \tag{6.9}$$

where G^k is a fixed variable and optimising ps we compute at each x $\in \Omega$ pointwise;

- Optimise pt by fixing other variables:

$$\begin{aligned} p_t^{k+1} &:= \arg \max_{p_t(x) \leq C_t(x)} Lc(p_s^{k+1}, p_t, p^{k+1}, \lambda^k) \\ &= \arg \max_{p_t(x) \leq C_t(x)} -\frac{c}{2}\|p_t - H^k\|^2 \end{aligned} \tag{6.10}$$

where H^k is a fixed variable and optimizing pt can be simply solved by

$$p_t(x) = \min(H^k(x), C_t(x)) \tag{6.11}$$

- then finally update λ by:

$$\lambda^{k+1} = \lambda^k - c(divp^{k+1} - p_s^{k+1} + p_t^{k+1}) \tag{6.12}$$

In the event of each iteration K^{+1} the convergence criterion is determined by

$$err^k = \|\lambda^{k+}1 - \lambda^k\|/\|\lambda^{k+1}\| \tag{6.13}$$

The method converges if the error rate $err^* < E$ or when it reaches the maximum number of iterations. Without losing context, in-depth details regarding the augmented Lagrangian, total variation and Lipschitz principles adopted in the method are obtainable from [12, 16, 17, 92].

6.4 Results and Discussion

The images utilised in this entire study were captured using the Heidelberg SD-OCT Spectralis HRA imaging system (Heidelberg Engineering, Heidelberg, Germany) in Tongren Hospital, China. Non-invasive OCT imaging centred at the macular region was performed on 13 subjects between 20 to 85 years of age. Manual ground truth labels of the layers were provided, which serve as benchmarks for evaluation of the algorithms' performance.

To evaluate the performance of the proposed methods in this thesis experiments were carried on a set of 225 macula OCT scans, 75 each from the temporal, foveal and nasal regions. The resolution of each image is 512 pixels in depth and 992 pixels across section with 16 bits per pixel. Fifteen per cent (15%) of the image height was clipped from the top to remove regions with low signal and no features of interest. Using MATLAB 2016a software, on a PC with Intel i5-4590 CPU, clock of 3.3GHz and 8GB RAM, the average computation time was 12 seconds per image. Comparing segmentation methods can be quite challenging because various studies use different data set and a variety of statistical matrices for evaluation. Also, the evaluation depends on the dimension of the data used, the standard used for comparison, e.g. ground truth, the similarity between many experts, and so on. For the sake of readability and to reduce wordiness, the compared methods are referred to as follows:

Chapter 3 - MGCS

Chiu et al. [27] - MSTC

Chapter 4 - MLSS

Chapter 5 - MRCL

Chapter 6 - MFHM

The evaluation is carried out by standardising the number of segmented layers to five, which have been illustrated earlier in Figure 6.1. Sample visual results of the methods are shown in Fig 6.4. Generally, all the methods performed beyond average, but with varying success rates as to be expected. This performance is somewhat attributed to the preprocessing steps because it reduces the impact of image noise. Hence, the major challenge posed is in the method's ability to handle inhomogeneity. MFHM adapts better to the inhomogeneity and inconsistency of retinal OCT images, based on experimental results to be discussed in the ensuing paragraphs.

To begin with, the Root Mean Squared Error (RMSE) and Dice coefficient (DC), which are common statistical measures for evaluating segmentation algorithms, are chosen to compare the performance of the selected methods. Comparison is made between the result of the methods and the ground truth labels by computing the RMSE and DC using equation (3.9) The adaptability to the inconsistency of the retinal layers of the methods is notable. This is an important factor due to the distinct retinal architecture for each person, in addition to various imaging protocols.

What can be extracted from Table 6.1 is that MFHM segments the NFL better, which can be attributed to the preprocessing technique in isolating the layers and the optimisation ability of the max-flow algorithm. Next, with regards to the NFL is MGCS, and then MSTC. The error in step is due to the inability of standard shortest path algorithms (e.g. [32]) to handle inhomogeneity such as that of the OCT. Although MFHM achieved the highest DC for the NFL, the accompanying SD is the highest. Also, MRCL outperforms MSTC in the NFL because in some cases it converges at a local minimum. The value of the NFL for both

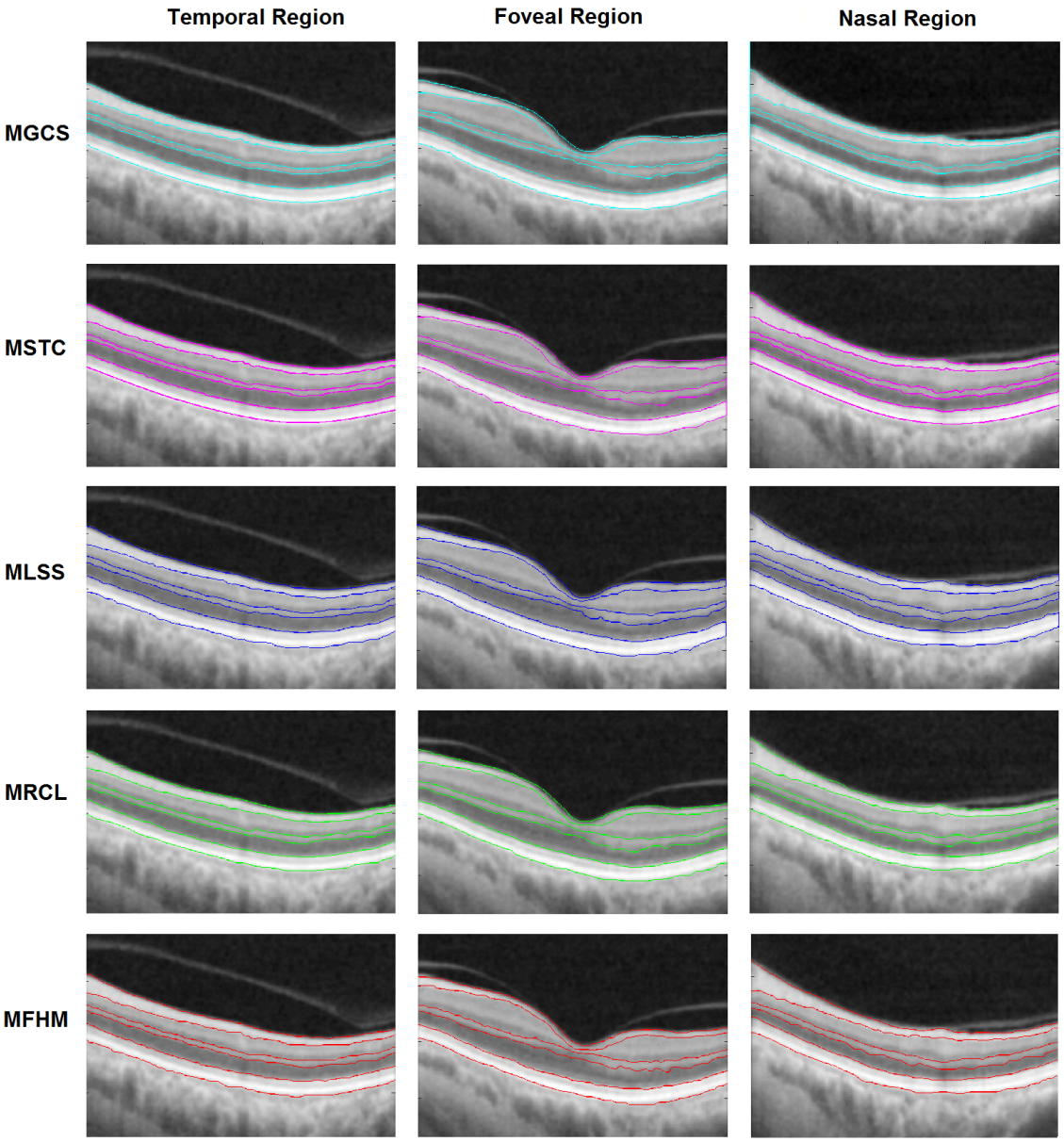

Figure 6.4: Results of the 5 compared methods. Showing results from left the temporal region, center the foveal region, and right nasal region of the reitina.

Table 6.1: Performance evaluation on 225 OCT images showing values of the Root Mean Squared Error (RMSE) and Dice Coefficient (standard deviation (SD)) in comparison to the true layer labelling (units in pixels).

Layer Name	**NFL**		**GCL - INL**		**OPL**		**ONL**		**IS - RPE**	
Methods	RMSE	Dice (SD)	RMSE	Dice (SD)	RMSE	Dice (SD)	RMSE	Dice (SD)	RMSE	Dice (SD)
MGCS [34]	0.0198	0.964 (0.026)	0.381	0.881 (0.036)	0.0380	0.836 (0.039)	0.0365	0.878 (0.045)	**0.0232**	**0.939 (0.021)**
MSTC [27]	0.0312	0.919 (0.083)	0.0442	0.879 (0.043)	0.0466	0.802 (0.040)	0.0381	0.856 (0.051)	0.0249	0.934 (0.024)
MLSS [40]	0.0286	0.933 (0.031)	0.390	0.883 (0.061)	0.0418	0.852 (0.042)	0.0379	0.884 (0.053)	0.0255	0.926 (0.023)
MRCL [37]	0.0273	0.921 (0.026)	0.0429	0.875 (0.038)	0.0402	0.867 (0.036)	0.0348	0.879 (0.049)	0.0331	0.923 (0.020)
MFHM	**0.0179**	**0.970 (0.029)**	**0.0293**	**0.890 (0.037)**	**0.0274**	**0.894 (0.048)**	**0.0283**	**0.895 (0.039)**	0.0319	0.918 (0.027)

RMSE and DC are promising to range from 0.921 to 0.970, respectively.

As for the RPE region, MGCS and MSTC segmented the RPE regions better than the others. The performance of both methods is due to the region limitation, which allows the methods to search within a specific range based on the layer characteristics. Plus, the RPE region has limited blood vessels interference. Additionally, MSTC outperforms MRCL for the same reasons. MFHM, in some cases, removes part of the RPE by cutting through the OS layer due to the proximity, which is the reason for its under-performance. Hence, the reason for the highest RMSE in RPE compared to other methods. Also, MRCL segments the RPE better than MFHM although both methods do not employ region limitation or topology constraints, but it is able to adapt to the topology, as it initially segments 9 layers as discussed in chapter 5.

MFHM segments four layers better than the other methods with better consistency as can be deduced from the values of DC and the RMSE in Table 6.1. Notably, The effect of using the FCM is influential to the performance MRCL and MFHM, which is indirectly deducible in comparison to MSTC and MGCS for the level set and graph cut methods, respectively. The FCM handles the inhomogeneity in case of image noise, by adaptively estimating values specific to the image, which aids the methods in achieving better results.

Generally, region limitation based on retinal topology aids in handling incompleteness in MGCS, MSTC and MSTC, while FCM aids in handling inhomogeneity within layers in MRCL and MFHM. This can be deduced from the NFL layer performance discussed earlier based on the performance matrix in Table 6.1. This is also portrayed in the GCL to IPL, OPL and ONL regions, except for the fact that MFHM segments these layers better. This is mainly because the transformation of the image makes the layers visible, making it straightforward for the method to identify the layers.

Due to the importance of the retinal nerve fibre layer in diagnosing eye diseases (and recently neurological and other terminal diseases), it is further assessed with the accuracy measure computer by:

$$Accuracy = \frac{TP + TN}{(TP + FP + FN + TN)} \tag{6.14}$$

Table 6.2: Performance evaluation on 225 OCT images showing values of accuracy (standard deviation (SD)) of the method in identifying the Nerve Fibre Layer (NFL) (units in pixels).

Method	**Accuracy Mean (SD)**
MGCS [34]	0.9281 (0.053)
MSTC [27]	0.8977 (0.058)
MLSS [40]	0.9045 (0.050)
MRCL [37]	0.9144 (0.052)
MFHM	**0.9440 (0.022)**

where the terms TP, TN, FP and FN refers to true positive, true negative, false positive and false negative respectively. Distinctly, TP represents the number of pixels which are part of the region in the ground truth that are labelled correctly by the segmentation methods. TN represents the number of pixels which are part of the background region in the ground truth and labelled correctly by the methods. FP denotes the pixels labelled as a part of the region by the methods but are actually part of the background in the ground truth. Lastly, the term FN represents the pixels labelled as a part of the background by the methods but are truly part of the region in the ground truth. The performance of the methods using the accuracy criteria (eqt. (6.14)) is shown in Table 6.2 while the distribution of the values is shown in Figure 6.5.

What can be deduced from Table 6.2 is that all methods are efficient in segmenting the NFL with accuracy between 0.89 and 0.94. MFHM achieves the highest accuracy of $\sim 95\%$, with accompanying adaptability to the contour variance of the OCT as may be inferred from the SD. With regards to the level set MSTC and MFHM, the superior performance of MFHM is due to MRCL converging at a local minimum in some images.

Moreover, the promising performance of these methods is further affirmed by the distribution of values in Figure 6.5. MGCS, MSTC and MRCL have the highest individual accuracy with their fourth quartiles reaching $\sim 99\%$. Notably, MGCS and MRCL have no outliers below the first quartile, which means they are more consistent in finding the retinal boundaries and with their accuracy values start from $\sim 76\%$. MSTC has the second best start of the first quartile. However, it has underperformed in identifying the NFL in few images due to some

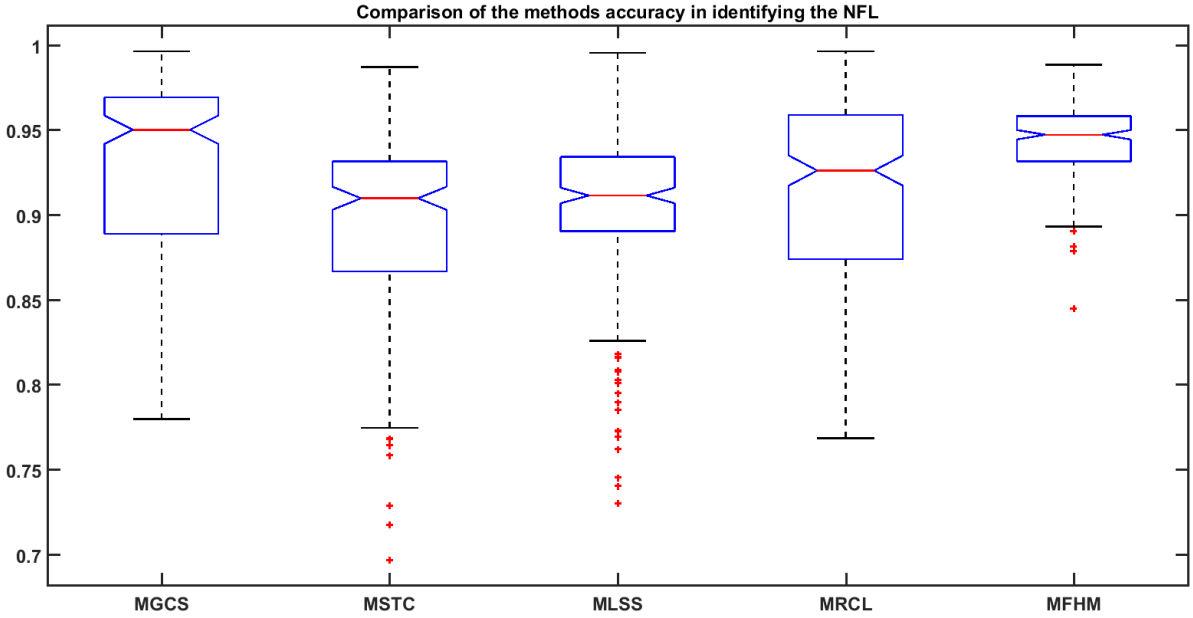

Figure 6.5: Boxplot of the distrubution of accuracy in segmenting retinal nerve fibre layer thickness results from Table 6.2.

constraints in the method as can be seen in the outliers (+ sign in red in Figure 6.5).

Further, although MFHM has the highest mean accuracy in Table 6.2 and the accuracy value starts at $\sim$ 84%, it still has few outliers in the distribution (+ sign in red in Figure 6.5). MFHM performs better because the bright layers have been isolated, which enables the appropriate location of the layers as the source and sink are adaptively assigned. In theory, MFHM is able to locate the optimal points where the change is highest, which corresponds to points with the minimum relationship between the nodes. MSTC have the lowest starting value at $\sim$ 70% due to the method falling for wrong short-cuts as hinted earlier. However, it has still achieved individual accuracy higher than MFHM.

In summary, the graph cut methods in MGCS and MFHM perform better than the level set methods in MSTC and MRCL. In particular, MFHM outperforms the others because it optimises the flow and then finds the layer boundaries. It is as if the max-flow min-cut algorithm is innate for segmentation problems, where the goal is to find the highest change from the standard layer distribution, which also refers to the point where the layers differ the most. Furthermore, the use of prior knowledge improves the performance of the methods

and enables them to achieve better results. Finally, If accuracy is desired, prior knowledge is essential in the development of the methods. Whereas computational methods for achieving good results are efficient and may segment more layers, there is always the challenge posed by image noise and inconsistency. This assertion is not generalisable as portrayed by the results, and further studies can look into balancing between both for better segmentation results.

6.5 Conclusion

This chapter has presented a fully automatic and simultaneous method to segment five layers from an OCT image by utilising domain knowledge and inexpensive computational methods. As opposed to filtering and averaging denoising methods, that usually require a filter window, we utilise domain knowledge to preprocess the image in order to reduce the effect of noise and improve homogeneity. Specifically, the cropping of the image to contain the layers only promotes accurate segmentation by aiding in convergence, while the improved FHH transformation improves segmentation results by reducing image noise and inhomogeneity. The preprocessing steps employed in this approach (and other chapters 3 to 5) can be used individually to improve the performance of other segmentation methods. This assertion is based on the understanding that the steps improve similarity and difference within the image, thereby isolating individual features of interest.

Further, the use of the reinforced fuzzy C-Means in building data terms allows the method to cater for inconsistency within the image, by computing membership value unique for each image. This process is appropriate for building the graph model for OCT segmentation, because the values of OCT vary even within each layer, depending on image noise and imaging modality.

Summatively, the experimental results of this study suggest that the methods can provide essential information necessary for the diagnosis and prevention of major eye diseases. Also, the results show the methods adapt to the inhomogeneity and pathological inconsistency of the retinal layers. These results are achieved by rigorous selection of computational methods that enable incorporation of prior knowledge.

Finally, a retrospective approach was taken in proposing this method by utilising efficient processes from previous chapters that are best suited for OCT analysis. This raises a question with regards to the dimension of machine learning approaches. Because this learning process can be facilitated through training a learning model. Machine learning models have recently been utilised and come with their challenges, which can be handled through the utilisation of prior knowledge.

Chapter 7

Conclusion

Research in computer-aided diagnostics is gaining more grounds in various aspects of healthcare. The reason for this is apparent, as it improves the diagnostic process and saves both time and effort compared to manual diagnosis. The role of medical image analysis in diagnosing diseases cannot be overemphasised as it allows the identification of various features of interest necessary for clinical examination. Notably, retinal image analysis is one of the highly researched areas due to the ability to extract useful information from retinal images used in diagnosing and preventing major eye diseases, including glaucoma, diabetic retinopathy and age-related macular degeneration. This intricacy in retinal image analysis is because the eye is one the five senses people value the most [71] and structural changes in retinal layers has been shown to correlate with the severity of the dominant eye diseases highly. As such, it is crucial to assess the changes occurring on retinal layers in OCT scans to monitor eye diseases, since the causes of these diseases are not fully known. To assess the changes in retinal layers caused by diseases requires segmentation of different retinal layers. However, this evaluation process is not only time consuming, cumbersome and subjective when done manually, but also becoming impossible due to the amount of data becoming available to clinicians for analysis.

Consequently, many automated retinal image analysis methods are being proposed due to the earlier mentioned challenges of manual image analysis and proven ability of automated analysis methods to extract the different futures necessary for a clinical eye examination. However, image noise, intensity homogeneity and other imaging artefacts significantly degrade

the performance of these automated methods. To handle these challenges, this thesis focuses on presenting robust and reliable automated techniques for retinal OCT image analysis. In this regard, four innovative methods for segmenting different retinal layers in OCT images are proposed. All the four methods achieved promising experimental results, which shows the proposed methods are efficient in segmenting the retinal layers. The proposed methods solve significant issues in OCT image analysis that are related to the lack of uniform intensity within layers in the OCT image, which hinders accurate segmentation of boundaries. These issues affect current OCT segmentation techniques such as level set, active contours, graph cut, machine learning approaches, and are also found in commercially available OCT imaging tools.

Furthermore, prior knowledge plays a vital role in image segmentation as it aids in dealing with the incompleteness of the retinal structure. Some of this knowledge is low level, such as coherence of brightness, colour, texture, but equally important is mid or high-level knowledge about consistency and topology of features or feature models. Therefore the architecture or characteristics of the image being analysed should ideally determine the set of constraints to be deployed in a segmentation algorithm. On the other hand, there is difficulty in classifying standard anatomy for all retinas due to several possible interpretations in the context. Thus difficulty then lies in specifying what constitutes prior knowledge.

Moreover, high-level segmentation methods such as graph-cut and level set provide the ability to incorporate prior knowledge, which we call modelling powers. Non-technically, these modelling powers are constraints or conditions that are imposed, usually based on prior knowledge, of how the method differentiates or separate the pixels of different regions. There is a wealth of information in Electronic health records (EHR). Harnessing knowledge from this data and integrating it with medical images will be of pivotal influence in personalising health care. The integration of this variety of data can also provide knowledge on establishing standards for clinical diagnosis and validation of segmentation methods. Additionally, it also will aid in: bridging the gap between clinicians and researchers; and establishing common standards for diagnosis and evaluation of retinal pathologies. Also, the beneficiaries of similar research work will increase by creating synergy among the different stakeholders in healthcare.

In summary, this thesis presents innovative and plausible fully automated methods for the segmentation of retinal layers from OCT images. It also provides insight into the challenges in image segmentation by raising factors that influence the performance of image segmentation algorithms. Although this thesis is by no means complete as highlighted in chapter 1, it is hoped that the contributions and findings of the research serve as a guide for future studies, as it enters the pool of literature, and therefore informs future research ideas. Similarly, a retrospective approach to the outlined limitations and the possible dimension of the study raises issues to be reflected upon for continuous improvement, which can be beneficial to the broader research community. The rest of this chapter is organised as follows. Section 7.1 summarises and recapitulates how each chapter contributes to meeting the objectives of this thesis with accompanying comparison. Beneficiaries of this research work are outlined and briefly discussed in section 7.2. Lastly, limitations and possible extensions of this thesis besides those highlighted earlier at the end of chapters 3 to 6 are discussed in Section 7.3.

7.1 Comparison of Proposed Methods

At this point, it is essential to reflect on the objectives of this thesis and highlight how each chapter contributes to achieving the objectives, as highlighted in chapter 1 b(section 1.2.

- **OBJ1**: Developing fully automated image segmentation methods.
- **OBJ2**: Combining rigorously selected image processing techniques.
- **OBJ3**: Utilising prior knowledge of the retinal layers to improve segmentation accuracy.
- **OBJ4**: Improving homogeneity in retinal OCT image.
- **OBJ5**: Preprocessing OCT images.
- **Chapter 3:** presented a sequential method for segmenting 7 layers across 8 boundaries of the retina **(OBJ1)**. The method uses image gradient and its inverse to represent image intensity values to calculate two adjacency matrices, which captures unique layer

characteristics. These adjacency matrices are transformed using fuzzy histogram hypolisation to improve the strength of connectivity amongst adjacent edges. The improved adjacent matrices are integrated into the graph-cut framework to sequentially segment 8 boundaries of the retina based on unique layer characteristics **(OBJ2), (OBJ3)**. Without losing context, the preprocessing technique in chapter 6 was the first instance fuzzy histogram hyperbolisation was explored in the entire research. The results from a preliminary study lead to one of the main ideas of this chapter, which is to say if the graph-cut method is dependent on the assignment of appropriate weight, then by improving the connectivity of adjacent edges in the adjacency matrix the performance of graph-cut methods can be improved.

Additionally, this transformation of the adjacency matrices is influenced by the understanding that if segmentation is based on similarity and differences, then making the features or regions in the images as unique as possible can improve the performance of segmentation algorithms. The method achieved promising results, but the segmentation less prominent boundaries rely on the accurate segmentation of the prominent ones. Further, the method is unable to properly segment GCL and IPl individually due to the noise and merging of layers at the foveal region. It also did not segment the IS from the OS region due to its proximity to the OS-IS boundary. Because, the method searches within a limited region, it sometimes obtains the ONL-IS boundary. Besides, the OS layer is thin, making it difficult to have a specific limit for the search space. For this reason, the method effectively identifies seven layers of the retina, which have been illustrated in 3.1. Also, this has triggered the exploration of simultaneous segmentation methods in chapters 4, 5 and 6.

- **Chapter 4:** the method proposed segments 7 layers of the retina simultaneously **(OBJ1)**. The method starts by establishing a specific region of interest **(OBJ5)**, which ensures the evolution of the initial layer boundaries is influenced by the actual layer properties solely. The method utilises edges from the OCT image gradients to represent initial layer boundary contours. Then constraints based on the OCT layer topology are deployed to

manage the evolution of the initial contours to the actual layer boundaries **(OBJ3)**. The method can handle edge leaks, which is a common challenge for standard level set methods. The method also converges quickly, as it carries out the topology checks before a boundary point expands or shrinks.

In contrast, the method in chapter 4 also segments 7 layers efficiently, but slightly different from those segmented in chapter 3. This difference in segmented layers is mainly because the topology constraints in chapter 4 differ from the region limitation in chapter 3. Mainly due to fragile boundaries within the GCL+IPl and INL region, the method converges better at the OPL region. It can handle the OS region better because the two other layers IS and RPE are the brightest. Consequently, the level set topology constraint can handle that challenge, as it evolves from the brighter part of the layers to where the layer boundaries transitions.

The constraints limit the performance of the method, as highlighted in the discussion in chapter 6.4. For this reason, the study in chapter 5 was initiated to explore level set segmentation further to segment more layers. The main additions of this chapter are the establishment of an explicit region of interest because boundary and image features influence the evolution of level set methods; the use of edge from the gradient in the initialisation phase; and the layering topology constraints imposed on the evolution process.

- **Chapter 5:** presented a fully automated simultaneous segmentation method for segmenting 9 retinal layers without imposing constraints in the segmentation process **OBJ1**. Similar to the method in chapter 4, the method starts by establishing a specific region of interest for the same reasons. This method utilises different methods including fuzzy C-means, edge detection and the graph cut all of which contributed to appropriate initialisation of the level set method **(OBJ2)**. The combination of these methods enables the selection of particular components belonging to the hyperreflective layers **(OBJ3)**. The level set method is then initialised based on a subset of the selected components and evolved adaptively to the boundaries based on various image forces. The convergence of

the method is upon reaching a criterion for optimality or reaching the maximum number of iterations.

The method leverages the ability of FCM to handle inhomogeneity and incompleteness, which overcomes the shortcomings of previous methods due to OCT noise and inhomogeneity. The method segments more layers compared to other proposed methods because it obtains the gradient of the image and then the selection of the hyperreflective layers, which allows it to differentiate each layer using the region competition. Also, the membership value has been incorporated into both the evolution and convergence function, which enables the method to distinguish between the individual retinal layers in the selective level set segmentation process. The distinct supplements of this chapter are the use of selected component in the initialisation phase; and the use of the fuzzy region competition to guide both the evolution and convergence of the selective level set method; which aids in handling the intensity inhomogeneity of OCT images.

In general, although parameterisation improves the performance segmentation methods, it is still limited to values that need to be set manually. For the sake of comparison and to further explore the graph cut method without constraints, the study in chapter 6 was initiated.

- **Chapter 6:** presented a method to segment 5 retinal layers using a combination of fuzzy image processing techniques and continuous max flow method **(OBJ1**, which is an extension of initial work [39] in this PhD research. As highlighted earlier, the preprocessing method utilised in chapter 3 was first explored in chapter 6. The proposed method starts by establishing a well-defined region of interest (ROI) with all the crucial layer information similar to methods in chapter 4 and 5. The ROI is then transformed using fuzzy histogram hyperbolisation to improve the homogeneity within individual layers **(OBJ4)**. Next, the intensity values of the transformed ROI is clustered into two (2) using fuzzy C-means. From the clustering outcome, pixels belonging to the hyperreflective layers are selected by thresholding the average of selected components and their gradients by a parameter **(OBJ3)**. These selected pixel's grey values are used to build data terms,

which are integrated into an unsupervised continuous max-flow framework to segment the retinal layers **OBJ2**.

The method segments 5 layers because no constraint is set, and the main thing taken into account is the brightness of the layers. Hence, the preprocessing steps are essential, as they isolate the layers to enable better segmentation of the targeted layers. The method takes advantage of a similar approach to the method in chapter 5 (to select components belonging to the hyper-reflective layers). Due to the foveal region merging, the method can efficiently segment 5 layers, and so far, no technique is integrated into the method to mitigate the merging of the layers. In contrast, Five (5) layers are the least to be segmented by any of the proposed methods in this thesis.

On the other hand, the method achieved the best segmentation results in four (4) out of the five (5) layers, compared to the other methods. The main additions of chapter 6 are, the transformation of images using restrained fuzzy histogram hyperbolisation; and the integration of selected components to build data terms, as opposed to constants, into the unsupervised continuous max-flow for segmentation. This combination enables the method to perform robust segmentation of OCT by handling the inhomogeneity within the images.

Discussion with regards to the individual performance of the proposed methods has been made earlier in section 6.4. The variance in the number of layers successfully segmented by each method relies on the modelling ability of the segmentation method and how the preprocessing supports the segmentation of the targeted layers effectively. Notably, promising results in segmenting the same 5 layers over 225 OCT images has been achieved by all the methods, which shows the suitability of the proposed methods for OCT segmentation. However, although the algorithms are developed based on the understanding of OCT images, they may perform differently on different dataset due to scanner resolution, disease or scanning protocol. In such cases, various parameters might require adjustment. On the other hand, this is an issue that may be handled better through machine learning algorithms.

Generally, the graph-cut methods outperformed the level set methods in OCT image seg-

mentation, which was not the expectation at the beginning of the evaluation experiments. While the level set method was able to segment more layers than the graph-based methods. It is to be noted that these observations are limited to the scope of this research, which can provide an avenue for further exploration. The full potential of the technology in retinal image analysis is yet to be fully utilised as commercial systems focus on segmenting only a few layers of the retina. Eye diseases pose a threat to the quality of life, which makes it critical to prevent them with new technology by leveraging the knowledge available.

7.2 Beneficiaries of the Thesis

Following the contributions as outlined in Chapter aims and recapitulated in Section contribution, the beneficiaries of this thesis are as follows:

1. **Eye specialists** One of the primary beneficiaries of this research work is ophthalmologists. Because the prevalence of major eye diseases and the challenges clinicians face in diagnosing and treating these diseases motivates the entire study. Other beneficiaries support in their various capacities in this endeavour to curtail vision loss and visual impairments. The methods proposed in this thesis can reduce the challenges faced by eye specialists by improving the accuracy of OCT image analysis tools and reducing the time it takes to complete an eye examination.

2. **Research community** This thesis benefits various research communities including, image preprocessing, image segmentation, data analysis and ophthalmology because it brings elements of these areas together as highlighted in the introductory section of chapter 2 (see section 2.1). The methods proposed in this thesis touches some aspects of optimisation, constraints, parameterisation and graph and statistical model based image processing in the context of image segmentation. This can benefit researchers and research groups focused on these research areas individually.

   Early stage researchers can highly benefit from this research. This is because it lays a foundation and provides supporting evidence as to why particular methods work and

also how the problems are formulated to fit into the solution. References to further literature are usually provided where necessary to enable interested parties to explore beyond the scope of this thesis. This is found to be useful because it is challenging to comprehend general ideas discussed in journals due to the vast amount of literature at the early research stage. Additionally, it will reduce the time it takes early stage researchers to familiarise with retinal image analysis, as it is well known how dwelling on literature can complicate the scoping process of research. It is a daunting process usually undertaken, and hopefully, the contents and structure of this thesis will simply and improve the process and outcome of the review process.

3. **Industry** the industry producing the OCT machines can derive useful information, for example, what makes the segmentation method restrictive, the factors that affect the accuracy of methods. In particular, the image preprocessing technique can be used as a first step image enhancement before applying other enhancement techniques. This can highly improve the performance of the complete image analysis results. This insight into the influencing factors can, in fact, be more beneficial to the industry as they have better access to both the research community and eye care specialists. Thereby allowing the industries to leverage this link to develop better machines.

7.3 Limitation and Future Work

This section discusses the limitation of this study and elaborates on possible directions for future work. The major limitations of this research can be summarised as follows:

1. As highlighted in chapter 6, there are challenges, including difference of dataset and evaluation metrics and the number of layers segmented, in comparing segmentation methods. The proposed methods could have been compared to more methods in the literature to better ascertain the performance and stands of the methods in the state of the art retinal image analysis.

2. As a result of limited access to data, the methods are only tested on healthy eyes. It

will be ideal to test the methods on both normal and abnormal images, to implement more efficient methods that could extract both normal and diseased features from OCT images robustly. Because the build-up of the proposed methods is such that they could work on different OCT images without the need for adjustment. However, we can only infer that based on performance due to the limited access to data.

3. Due to limited accessibility to eye specialists, we are uncertain about the immediate needs of the clinics and hospitals. For example, most of the prior knowledge utilised in this research is based on the understanding of the OCT and information from the literature. We might not know very current and vital information in eye diagnosis unless published, which hinders the development of analyses tools, because algorithms capable of solving the problems in real-time would have been ideal.

4. Due to the limitation of the desktop computing capability, we were unable to fully engage in 3D retinal image analysis, which may provide more layer contextual information for diagnosing of eye diseases.

Based on some of the limitations and ever-changing nature of both eye diagnosis and computer-aided diagnostic tools, there are many avenues that research in the retinal image analysis may take. Thus, we cannot exhaust the list of possibilities, but we highlight some directions with the most potential based on findings are as follows:

1. Similar to many other imaging modalities, OCT imaging systems introduce lots of speckle-noise and artefacts during the imaging process. As such, more powerful and efficient denoising methods are necessary to filter out all noise while preserving all the layer structure information. There are many existing methods for image denoising, such as median filter, Gaussian, and anisotropic diffusion filter, to mention a few. Improving these methods can make the structure extraction more accessible and efficient.

2. Computer-aided diagnostic tools are currently used in much diagnostic decision making. For example, in classifying healthy and unhealthy eyes or the presence or absence of particular eye disease. Using segmentation results in the absence of ground truth labels

has also proven to be useful and handle the challenge of training data in machine learning techniques. We can further test the accuracy of the methods by incorporating the results into a classification problem. However, this is dependent on data availability. Also, to assess the actual performance of such methods requires monitoring of time series data is essential to monitor minor changes to the retinal structures.

Furthermore, image registration techniques for both 2D and 3D images are critically needed to monitor the longitudinal data collected. These methods will enable the efficient monitoring of eye diseases as they begin manifesting in their early stages to allow timely intervention.

3. As both data and code publishing is now on the rise, further evaluation of the methods on different datasets will be conducted, with the view to better understand the influencing factors in image segmentation. It will be essential to enable intensive view into the performance of the methods.

4. Use of machine learning techniques: When this study started the use of machine learning in computer vision is not as common as it is now. It is evident from this research that through learning more about the structure of the data and prior knowledge, we were able to improve the performance of the latter methods. Now with the machine learning framework, this learning process can be facilitated with improved accuracy and utilisation of the most relevant image traits in the image analysis process.

5. Develop interactive segmentation versions of the proposed methods to ascertain if the interactive segmentation can enable segmentation of all the retinal layers and compare the results to the fully automated methods proposed in this thesis.

Bibliography

[1] G. D. Aaker, J. S. Myung, J. R. Ehrlich, M. Mohammed, C. Henchcliffe, and S. Kiss. Detection of retinal changes in parkinson's disease with spectral-domain optical coherence tomography. *Clinical ophthalmology (Auckland, NZ)*, 4:1427, 2010.

[2] M. D. Abràmoff, M. K. Garvin, and M. Sonka. Retinal imaging and image analysis. *IEEE reviews in biomedical engineering*, 3:169–208, 2010.

[3] R. Adams and L. Bischof. Seeded region growing. *IEEE Transactions on Pattern Analysis and Machine Intelligence*, 16(6):641–647, 1994.

[4] J. Ambati, B. K. Ambati, S. H. Yoo, S. Ianchulev, and A. P. Adamis. Age-related macular degeneration: etiology, pathogenesis, and therapeutic strategies. *Survey of ophthalmology*, 48(3):257–293, 2003.

[5] B. J. Antony, M. D. Abràmoff, M. Sonka, Y. H. Kwon, and M. K. Garvin. Incorporation of texture-based features in optimal graph-theoretic approach with application to the 3D segmentation of intraretinal surfaces in SD-OCT volumes. In *Medical Imaging 2012: Image Processing*, 2012.

[6] B. J. Antony, A. Lang, E. K. Swingle, O. Al-Louzi, A. Carass, S. Solomon, P. A. Calabresi, S. Saidha, and J. L. Prince. Simultaneous segmentation of retinal surfaces and microcystic macular edema in SDOCT volumes. In *Medical Imaging 2016: Image Processing*, 2016.

[7] M. A. Atkinson, G. S. Eisenbarth, and A. W. Michels. Type 1 diabetes. *The Lancet*, 383(9911):69–82, 2014.

[8] S. Baglietto, I. E. Kepiro, G. Hilgen, E. Sernagor, V. Murino, and D. Sona. Segmentation of retinal ganglion cells from fluorescent microscopy imaging. In *Proceedings of the 10th International Joint Conference on Biomedical Engineering Systems and Technologies (BIOSTEC 2017)*, pages 17–23, 2017.

[9] M. Baroni, P. Fortunato, and A. La Torre. Towards quantitative analysis of retinal features in optical coherence tomography. *Medical engineering & physics*, 29(4):432–441, 2007.

[10] B. Basavaprasad and M. Ravi. A comparative study on classification of image segmentation methods with a focus on graph based techniques. *International Journal of Research in Engineering and Technology*, 3(03):310–314, 2014.

[11] B. Bengtsson, M. C. Leske, L. Hyman, A. Heijl, E. M. G. T. Group, et al. Fluctuation of intraocular pressure and glaucoma progression in the early manifest glaucoma trial. *Ophthalmology*, 114(2):205–209, 2007.

[12] D. P. Bertsekas. *Nonlinear programming*. Athena scientific Belmont, 1999.

[13] B. Bourdin and A. Chambolle. Implementation of an adaptive finite-element approximation of the mumford-shah functional. *Numerische Mathematik*, 85(4):609–646, 2000.

[14] K. L. Boyer, A. Herzog, and C. Roberts. Automatic recovery of the optic nervehead geometry in optical coherence tomography. *IEEE Transactions on Medical Imaging*, 25(5):553–570, 2006.

[15] Y. Boykov and G. Funka-Lea. Graph cuts and efficient N-D image segmentation. *International Journal of Computer Vision*, 70(2):109–131, 2006.

[16] Y. Boykov and M.-P. Jolly. Interactive Graph Cuts for Optimal Boundary & Region Segmentation of Objects in N-D Images. *Proceedings Eighth IEEE International Conference on Computer Vision. ICCV 2001*, 1(July):105–112, 2001.

[17] Y. Boykov and V. Kolmogorov. An experimental comparison of min-cut/max- flow algorithms for energy minimization in vision. *IEEE Transactions on Pattern Analysis and Machine Intelligence*, 26(9):1124–1137, 2004.

[18] Y. Boykov, O. Veksler, and R. Zabih. Markov random fields with efficient approximations. In *Proceedings. 1998 IEEE Computer Society Conference on Computer Vision and Pattern Recognition (Cat. No. 98CB36231)*, pages 648–655. IEEE, 1998.

[19] Y. Boykov, O. Veksler, and R. Zabih. Fast approximate energy minimization via graph cuts. *IEEE Transactions on pattern analysis and machine intelligence*, 23(11):1222–1239, 2001.

[20] G. H. Bresnick, D. B. Mukamel, J. C. Dickinson, and D. R. Cole. A screening approach to the surveillance of patients with diabetes for the presence of vision-threatening retinopathy. *Ophthalmology*, 107(1):19–24, 2000.

[21] D. Cabrera Fernández, H. M. Salinas, and C. A. Puliafito. Automated detection of retinal layer structures on optical coherence tomography images. *Optics Express*, 13(25):10200, 2005.

[22] A. Carass, A. Lang, M. Hauser, P. A. Calabresi, H. S. Ying, and J. L. Prince. Multiple-object geometric deformable model for segmentation of macular oct. *Biomedical optics express*, 5(4):1062–1074, 2014.

[23] T. F. Chan, B. Y. Sandberg, and L. A. Vese. Active contours without edges for vector-valued images. *Journal of Visual Communication and Image Representation*, 11(2):130–141, 2000.

[24] T. F. Chan and L. A. Vese. Active contours without edges. *IEEE Transactions on image processing*, 10(2):266–277, 2001.

[25] S. Chaudhuri, S. Chatterjee, N. Katz, M. Nelson], and M. Goldbaum. Detection of Blood Vessels in Retinal Images Using Two-Dimensional Matched Filters. *IEEE Transactions on Image Processing*, 8(3):263–269, 1989.

[26] S. J. Chiu, M. J. Allingham, P. S. Mettu, S. W. Cousins, J. A. Izatt, and S. Farsiu. Kernel regression based segmentation of optical coherence tomography images with diabetic macular edema. *Biomedical Optics Express*, 2015.

[27] S. J. Chiu, X. T. Li, P. Nicholas, C. a. Toth, J. a. Izatt, and S. Farsiu. Automatic segmentation of seven retinal layers in SDOCT images congruent with expert manual segmentation. *Optics express*, 18(18):19413–19428, 2010.

[28] T. A. Ciulla, C. D. Regillo, and A. Harris. *Retina and optic nerve imaging*. Lippincott Williams & Wilkins, 2003.

[29] D. Comaniciu and P. Meer. Mean shift analysis and applications. In *Proceedings of the Seventh IEEE International Conference on Computer Vision*, volume 2, pages 1197–1203. IEEE, 1999.

[30] T. H. Cormen, C. E. Leiserson, R. L. Rivest, and C. Stein. *Introduction to algorithms*. MIT press, 2009.

[31] D. C. DeBuc. A review of algorithms for segmentation of retinal image data using optical coherence tomography. *Image Segmentation*, pages 15–54, 2011.

[32] E. W. Dijkstra. A note on two problems in connexion with graphs. *Numerische mathematik*, 1(1):269–271, 1959.

[33] B. I. Dodo, Y. Li, M. I. Dodo, and X. Liu. Simultaneous segmentation of retinal oct images using level set. In *International Joint Conference on Biomedical Engineering Systems and Technologies*, pages 120–136. Springer, 2019.

[34] B. I. Dodo, Y. Li, K. Eltayef, and X. Liu. Graph-cut segmentation of retinal layers from oct images. In *Proceedings of the 11th International Joint Conference on Biomedical Engineering Systems and Technologies - Volume 2: BIOIMAGING,*, pages 35–42. INSTICC, SciTePress, 2018.

[35] B. I. Dodo, Y. Li, K. Eltayef, and X. Liu. Min-cut segmentation of retinal oct images. In *International Joint Conference on Biomedical Engineering Systems and Technologies*, pages 86–99. Springer, 2018.

[36] B. I. Dodo, Y. Li, K. Eltayef, and X. Liu. Automatic annotation of retinal layers in optical coherence tomography images. *Journal of Medical Systems*, 43(12):336, Nov 2019.

[37] B. I. Dodo, Y. Li, D. Kaba, and X. Liu. Retinal oct segmentation using fuzzy region competition and level set methods. In *2019 IEEE 32th International Symposium on Computer-Based Medical Systems (CBMS)*, page In press. IEEE, 2017.

[38] B. I. Dodo, Y. Li, D. Kaba, and X. Liu. Retinal layer segmentation in optical coherence tomography images. *IEEE Access*, 7:152388–152398, 2019.

[39] B. I. Dodo, Y. Li, and X. Liu. Retinal oct image segmentation using fuzzy histogram hyperbolization and continuous max-flow. In *2017 IEEE 30th International Symposium on Computer-Based Medical Systems (CBMS)*, pages 745–750. IEEE, 2017.

[40] B. I. Dodo., Y. Li., X. Liu., and M. I. Dodo. Level set segmentation of retinal oct images. In *Proceedings of the 12th International Joint Conference on Biomedical Engineering Systems and Technologies - Volume 2: BIOIMAGING,*, pages 49–56. INSTICC, SciTePress, 2019.

[41] J. Duan, C. Tench, I. Gottlob, F. Proudlock, and L. Bai. Automated segmentation of retinal layers from optical coherence tomography images using geodesic distance. *Pattern Recognition*, 72:158 – 175, 2017.

[42] P. Echevarria, T. Miller, and J. O'Meara. Blood Vessel Segmentation in Retinal Images. *Archives of Ophthalmology*, pages 1–13, 2004.

[43] L. Fang, D. Cunefare, C. Wang, R. H. Guymer, S. Li, and S. Farsiu. Automatic segmentation of nine retinal layer boundaries in OCT images of non-exudative AMD patients using deep learning and graph search. *Biomedical Optics Express*, 2017.

[44] A. F. Fercher, C. K. Hitzenberger, G. Kamp, and S. Y. El-Zaiat. Measurement of intraocular distances by backscattering spectral interferometry. *Optics communications*, 117(1-2):43–48, 1995.

[45] D. Fernandez. Delineating fluid-filled region boundaries in optical coherence tomography images of the retina. *IEEE Transactions on Medical Imaging*, 24(8):939–945, 2005.

[46] L. R. Ford and D. R. Fulkerson. Maximal flow through a network. *Journal canadien de mathématiques*, 8:399–404, 1956.

[47] G. R. Foundation. Types of glaucoma, 2019 (accessed June 1, 2019). `https://www.glaucoma.org/glaucoma/types-of-glaucoma.php`.

[48] M. Fraz, R. Welikala, A. Rudnicka, C. Owen, D. Strachan, and S. Barman. QUARTZ: Quantitative Analysis of Retinal Vessel Topology and size – An automated system for quantification of retinal vessels morphology. *Expert Systems with Applications*, 42(20):7221–7234, 2015.

[49] D. S. Friedman, B. J. O'Colmain, B. Munoz, S. C. Tomany, C. McCarty, P. De Jong, B. Nemesure, P. Mitchell, J. Kempen, et al. Prevalence of age-related macular degeneration in the united states. *Arch ophthalmol*, 122(4):564–572, 2004.

[50] K. Fu and J. Mui. A survey on image segmentation. *Pattern Recognition*, 13(1):3–16, 1981.

[51] K. Fukunaga and L. Hostetler. The estimation of the gradient of a density function, with applications in pattern recognition. *IEEE Transactions on Information Theory*, 21(1):32–40, 1975.

[52] K. G., H. R. Tizhoosh, T. Lilienblum, C. J. Moore, and B. Michaelis. Fuzzy Image Enhancement and Associative Feature Matching in Radiotherapy. In *IEEE international Conference on Neural Networks*, page 1490, 1997.

[53] M. K. Garvin. Automated 3-D segmentation and analysis of retinal optical coherence tomography images. *PhD thesis - The University of Iowa*, 2008.

[54] M. K. Garvin, M. D. Abràmoff, R. Kardon, S. R. Russell, X. Wu, and M. Sonka. Intraretinal layer segmentation of macular optical coherence tomography images using optimal 3-D graph search. *IEEE Transactions on Medical Imaging*, 27(10):1495–1505, 2008.

[55] M. K. Garvin, M. D. Abràmoff, X. Wu, S. R. Russell, T. L. Burns, and M. Sonka. Automated 3-D intraretinal layer segmentation of macular spectral-domain optical coherence tomography images. *IEEE transactions on medical imaging*, 28(9):1436–1447, 2009.

[56] A. George, J. Dilienseger, M. Weber, and A. Pechereau. Optical coherence tomography image processing. In *Investigative Ophthalmology & Visual Science*, volume 41, pages S173–S173. ASSOC RESEARCH VISION OPHTHALMOLOGY INC 9650 ROCKVILLE PIKE, BETHESDA, MD, 2000.

[57] S. Gibson. An eye examination, 2015, (accessed 10 October 2015). `http://www.sgoeyecare.co.uk/abouteyes.htm#glaucoma`.

[58] A. V. Goldberd and R. E. Tarjan. A New Approach to the Maximum-Flow Problem. *Journal of the Association for Computing Machinery*, 35(4):921–940, 1988.

[59] F. Gómez-Ulla, M. I. Fernandez, F. Gonzalez, P. Rey, M. Rodriguez, M. J. Rodriguez-Cid, F. F. Casanueva, M. A. Tome, J. Garcia-Tobio, and F. Gude. Digital retinal images and teleophthalmology for detecting and grading diabetic retinopathy. *Diabetes Care*, 25(8):1384–1389, 2002.

[60] B. I. Gramatikov. Modern technologies for retinal scanning and imaging: an introduction for the biomedical engineer. *Biomedical engineering online*, 13(1):52, 2014.

[61] C. D. Green. Classics in the History of Psychology. *Classics in the History of Psychology*, 15(1960):1–7, 2002.

[62] G. Gregori and R. Knighton. A Robust Algorithm for Retinal Thickness Measurements using Optical Coherence Tomography (Stratus OCT). *Investigative Ophthalmology Visual Science*, 45(13):3007, may 2004.

[63] L. Guariguata. Contribute data to the 6th edition of the idf diabetes atlas. *Diabetes research and clinical practice*, 100(2):280, 2013.

[64] M. Haeker, X. Wu, M. Abràmoff, R. Kardon, and M. Sonka. Incorporation of regional information in optimal 3-d graph search with application for intraretinal layer segmentation of optical coherence tomography images. In *Biennial International Conference on Information Processing in Medical Imaging*, pages 607–618. Springer, 2007.

[65] R. M. Haralick and L. G. Shapiro. Image segmentation techniques. *Computer Vision, Graphics, and Image Processing*, 29(1):100–132, 1985.

[66] V. Harjutsalo, R. Sund, M. Knip, and P.-H. Groop. Incidence of type 1 diabetes in finland. *Jama*, 310(4):427–428, 2013.

[67] Y. He, A. Carass, Y. Yun, C. Zhao, B. M. Jedynak, S. D. Solomon, S. Saidha, P. A. Calabresi, and J. L. Prince. Towards topological correct segmentation of macular oct from cascaded fcns. In *Fetal, Infant and Ophthalmic Medical Image Analysis*, pages 202–209. Springer, 2017.

[68] Y. He, A. Carass, Y. Yun, C. Zhao, B. M. Jedynak, S. D. Solomon, S. Saidha, P. A. Calabresi, and J. L. Prince. Towards topological correct segmentation of macular OCT from cascaded FCNs. In *Lecture Notes in Computer Science (including subseries Lecture Notes in Artificial Intelligence and Lecture Notes in Bioinformatics)*, 2017.

[69] A. Heijl, M. C. Leske, B. Bengtsson, L. Hyman, B. Bengtsson, and M. Hussein. Reduction of intraocular pressure and glaucoma progression: results from the early manifest glaucoma trial. *Archives of ophthalmology*, 120(10):1268–1279, 2002.

[70] A. Herzog, K. L. Boyer, and C. Roberts. Robust extraction of the optic nerve head in optical coherence tomography. In *Computer vision and mathematical methods in medical and biomedical image analysis*, pages 395–407. Springer, 2004.

[71] M. E. Hospital. Anatomy of the eye, 2017 (accessed June 1, 2019). `https://www.moorfields.nhs.uk/content/anatomy-eye`.

[72] M. E. Hospital. Age-related macular degeneration (amd), 2019 (accessed June 1, 2019). https://www.moorfields.nhs.uk/condition/age-related-macular-degeneration-amd.

[73] M. E. Hospital. Diabetic retinopathy, 2019 (accessed June 1, 2019). https://www.moorfields.nhs.uk/condition/diabetic-retinopathy.

[74] M. E. Hospital. Glaucoma, 2019 (accessed June 1, 2019). https://www.moorfields.nhs.uk/condition/glaucoma.

[75] S. T. Hospital. Diabetic eye, 2019 (accessed June 1, 2019). https://www.southtees.nhs.uk/services/diabetic-eye-screening/diabetic-eye/.

[76] Z. Hu, M. Niemeijer, M. D. Abràmoff, and M. K. Garvin. Multimodal retinal vessel segmentation from spectral-domain optical coherence tomography and fundus photography. *IEEE Transactions on Medical Imaging*, 31(10):1900–1911, 2012.

[77] D. Huang, E. A. Swanson, C. P. Lin, J. S. Schuman, W. G. Stinson, W. Chang, M. R. Hee, T. Flotte, K. Gregory, and C. A. Puliafito. Optical coherence tomography. *Science (New York, N.Y.)*, 254(5035):1178–81, 1991.

[78] N. Iftimia, B. E. Bouma, and G. J. Tearney. Speckle reduction in optical coherence tomography by "path length encoded" angular compounding. *Journal of Biomedical Optics*, 8(2):260–263, 2003.

[79] R. Inzelberg, J. A. Ramirez, P. Nisipeanu, and A. Ophir. Retinal nerve fiber layer thinning in parkinson disease. *Vision research*, 44(24):2793–2797, 2004.

[80] G. J. Jaffe. OCT of the Macula: An expert provides a primer on useful scans, identifying artifacts and time domain vs. spectral domain technology. *Reinal Physician*, pages 10–12, 2012.

[81] D. Kaba. *Computational models for stuctural analysis of retinal images*. PhD thesis, Brunel University London, 2014.

[82] D. Kaba, Y. Wang, C. Wang, X. Liu, H. Zhu, a. G. Salazar-Gonzalez, and Y. Li. Retina layer segmentation using kernel graph cuts and continuous max-flow. *Optics express*, 23(6):7366–84, 2015.

[83] D. Kaba, Y. Wang, C. Wang, X. Liu, H. Zhu, A. G. Salazar-Gonzalez, and Y. Li. Retina layer segmentation using kernel graph cuts and continuous max-flow. *Optics Express*, 23(6):7366–7384, 2015.

[84] R. Kafieh, H. Rabbani, and S. Kermani. A review of algorithms for segmentation of optical coherence tomography from retina. *J Med Signals Sens*, 3(1):45–60, 2013.

[85] M. Kass, A. Witkin, and D. Terzopoulos. Snakes: Active contour models, 1988.

[86] R. L. Kettig and D. Landgrebe. Classification of multispectral image data by extraction and classification of homogeneous objects. *IEEE Transactions on geoscience Electronics*, 14(1):19–26, 1976.

[87] R. I. Kitney and N. Smith. Image segmentation method, Jan. 4 2005. US Patent 6,839,462.

[88] R. Klein and B. E. K. Klein. The Prevalence of Age-Related Eye Diseases and Visual Impairment in Aging: Current EstimatesPrevalences of Age-Related Eye Diseases. *Investigative Ophthalmology & Visual Science*, 54(14):ORSF5–ORSF13, 12 2013.

[89] D. C. Klonoff and D. M. Schwartz. An economic analysis of interventions for diabetes. *Diabetes care*, 23(3):390–404, 2000.

[90] B. M. Koeppen and B. A. Stanton. *Berne and Levy Physiology, Updated Edition E-Book*. Elsevier Health Sciences, 2009.

[91] H. Kolb, E. Fernandez, and R. Nelson. Bipolar cell pathways in the vertebrate retina–webvision: The organization of the retina and visual system. 1995.

[92] V. Kolmogorov and R. Zabih. What Energy Functions Can Be Minimized via Graph Cuts? *IEEE Transactions on Pattern Analysis and Machine Intelligence*, 26(2):147–159, 2004.

[93] D. Koozekanani, K. Boyer, and C. Roberts. Retinal thickness measurements from optical coherence tomography using a Markov boundary model. *IEEE Transactions on Medical Imaging*, 20(9):900–916, 2001.

[94] R. Koprowski and Z. Wrobel. Layers recognition in tomographic eye image based on random contour analysis. In *Computer Recognition Systems 3*, pages 471–478. Springer, 2009.

[95] M. F. Kraus, B. Potsaid, M. A. Mayer, R. Bock, B. Baumann, J. J. Liu, J. Hornegger, and J. G. Fujimoto. Motion correction in optical coherence tomography volumes on a per a-scan basis using orthogonal scan patterns. *Biomedical optics express*, 3(6):1182–1199, 2012.

[96] A. Lang, A. Carass, M. Hauser, E. S. Sotirchos, P. a. Calabresi, H. S. Ying, and J. L. Prince. Retinal layer segmentation of macular OCT images using boundary classification. *Biomedical optics express*, 4(7):1133–52, 2013.

[97] K. Lee, M. Niemeijer, M. K. Garvin, Y. H. Kwon, M. Sonka, M. D. Abramoff, and M. D. Abràmoff. Segmentation of the optic disc in 3-D OCT scans of the optic nerve head. *IEEE Transactions on Medical Imaging*, 29(1):159–68, 2010.

[98] A. E. Lefohn, J. M. Kniss, C. D. Hansen, and R. T. Whitaker. A streaming narrow-band algorithm: interactive computation and visualization of level sets. *IEEE Transactions on Visualization and Computer Graphics*, 10(4):422–433, 2004.

[99] B. N. Li, C. K. Chui, S. Chang, and S. H. Ong. Integrating spatial fuzzy clustering with level set methods for automated medical image segmentation. *Computers in biology and medicine*, 41(1):1–10, 2011.

[100] B. N. Li, J. Qin, R. Wang, M. Wang, and X. Li. Selective level set segmentation using fuzzy region competition. *IEEE Access*, 4:4777–4788, 2016.

[101] G. Liew, J. J. Wang, P. Mitchell, and T. Y. Wong. Retinal vascular imaging: a new tool

in microvascular disease research. *Circulation: Cardiovascular Imaging*, 1(2):156–161, 2008.

[102] L. S. Lim, P. Mitchell, J. M. Seddon, F. G. Holz, and T. Y. Wong. Age-related macular degeneration. *The Lancet*, 379(9827):1728–1738, 2012.

[103] Y. Liu, A. Carass, S. D. Solomon, S. Saidha, P. A. Calabresi, and J. L. Prince. Multi-layer fast level set segmentation for macular oct. In *2018 IEEE 15th International Symposium on Biomedical Imaging (ISBI 2018)*, pages 1445–1448, April 2018.

[104] S. Lu, C. Y.-l. Cheung, J. Liu, J. H. Lim, C. K.-s. Leung, and T. Y. Wong. Automated layer segmentation of optical coherence tomography images. *IEEE Transactions on biomedical engineering*, 57(10):2605–2608, 2010.

[105] S. Lu, C. Yim-liu, J. H. Lim, C. K.-s. Leung, and T. Y. Wong. Automated layer segmentation of optical coherence tomography images. *Proceedings - 2011 4th International Conference on Biomedical Engineering and Informatics, BMEI 2011*, 1(10):142–146, 2011.

[106] V. Magudeeswaran and C. G. Ravichandran. Fuzzy Logic-Based Histogram Equalization for Image Contrast Enhancement. *Mathematical Problems in Engineering*, 2013.

[107] N. Mahabadi and Y. Al Khalili. Neuroanatomy, retina. In *StatPearls [Internet]*. StatPearls Publishing, 2019.

[108] R. Malladi, J. A. Sethian, and B. C. Vemuri. Shape modeling with front propagation: a level set approach. *IEEE Transactions on Pattern Analysis and Machine Intelligence*, 17(2):158–175, 1995.

[109] S. Marschall, B. Sander, M. Mogensen, T. M. Jørgensen, and P. E. Andersen. Optical coherence tomography—current technology and applications in clinical and biomedical research. *Analytical and bioanalytical chemistry*, 400(9):2699–2720, 2011.

[110] D. Martin, C. Fowlkes, D. Tal, J. Malik, et al. In *A database of human segmented natural images and its application to evaluating segmentation algorithms and measuring ecological statistics*. Iccv Vancouver:, 2001.

[111] M. A. Mayer, J. Hornegger, C. Y. Mardin, and R. P. Tornow. Retinal Nerve Fiber Layer Segmentation on FD-OCT Scans of Normal Subjects and Glaucoma Patients. *Biomedical optics express*, 1(5):1358–1383, 2010.

[112] K. McGuinness and N. E. O'Connor. A comparative evaluation of interactive segmentation algorithms. *Pattern Recognition*, 43(2):434–444, 2010.

[113] J. M. Medina, S. Jaime-Castillo, C. D. Barranco, and J. R. Campaña. On the use of a fuzzy object-relational database for flexible retrieval of medical images. *IEEE Transactions on Fuzzy Systems*, 20(4):786–803, 2012.

[114] S. Melmed, K. S. Polonsky, P. R. Larsen, and H. M. Kronenberg. *Williams textbook of endocrinology*. Elsevier Health Sciences, 2015.

[115] A. Mishra, A. Wong, K. Bizheva, and D. A. Clausi. Intra-retinal layer segmentation in optical coherence tomography images. *Optics Express*, 17(26):23719–28, 2009.

[116] M. Mujat, R. Chan, B. Cense, B. H. Park, C. Joo, T. Akkin, T. C. Chen, and J. F. de Boer. Retinal nerve fiber layer thickness map determined from optical coherence tomography images. *Optics express*, 13(23):9480–91, 2005.

[117] D. Mumford and J. Shah. Optimal approximations by piecewise smooth functions and associated variational problems. *Communications on pure and applied mathematics*, 42(5):577–685, 1989.

[118] T. Murakami and N. Yoshimura. Structural changes in individual retinal layers in diabetic macular edema. *Journal of diabetes research*, 2013, 2013.

[119] N. I. o. H. National Eye Institute. Facts about diabetic retinopathy, 2015 (Last reviewed on September 2015 and accessed June 1, 2019). `https://www.nei.nih.gov/health/diabetic/retinopathy`.

[120] N. I. o. H. National Eye Institute. Facts about glaucoma, 2017 (Last reviewed on 22/06/2017 and accessed June 1, 2019). https://www.nei.nih.gov/health/glaucoma/glaucoma_facts.

[121] N. I. o. H. National Eye Institute. Age-related macular degeneration (amd), 2019 (accessed June 1, 2019). https://www.nei.nih.gov/eyedata/amd#5.

[122] E. Y. Ng, U. R. Acharya, J. S. Suri, and A. Campilho. *Image analysis and modeling in ophthalmology*. CRC press, 2014.

[123] P. C. Ng and J. J. Oliver. Anatomy of the eye. In *Handbook of Emergency Ophthalmology*, pages 1–12. Springer, 2018.

[124] M. S. Nosrati and G. Hamarneh. Incorporating prior knowledge in medical image segmentation: a survey. *arXiv preprint arXiv:1607.01092*, 2016.

[125] S. M. Nosrati. *Prior Knowledge for Targeted Object Segmentation in Medical Images*. PhD thesis, Applied Sciences: School of Computing Science, Simon Fraser University., 2015.

[126] J. Novosel, K. A. Vermeer, G. Thepass, H. G. Lemij, and L. J. V. Vliet. Loosely Coupled Level Sets For Retinal Layer Segmentation In Optical Coherence Tomography. *IEEE 10th International Symposium on Biomedical Imaging*, pages 998–1001, 2013.

[127] W. H. Organization et al. Global data on visual impairments 2010. 2012, geneva, switzerland: Published by the world health organization. Technical report, WHO/NMH/PBD/12.01 (http://www. who. int/about/regions/en/index. html).

[128] S. Osher and J. A. Sethian. Fronts Propagating with Curvature Dependent Speed: Algorithms Based on Hamilton-Jacobi Formulations. *Journal of Chemical Information and Modeling*, 53(9):1689–1699, 1988.

[129] N. R. Pal and S. K. Pal. A review on image segmentation techniques. *Pattern recognition*, 26(9):1277–1294, 1993.

[130] B. Peng, L. Zhang, and D. Zhang. A survey of graph theoretical approaches to image segmentation. *Pattern Recognition*, 46(3):1020–1038, mar 2013.

[131] J. Petitot. An introduction to the mumford–shah segmentation model. *Journal of Physiology-Paris*, 97(2-3):335–342, 2003.

[132] D. L. Pham, C. Xu, and J. L. Prince. Current Methods in Medical Image Segmentation. *Annu Rev Biomed Eng*, 2:315–337, 2000.

[133] M. Pircher, E. Go¨tzinger, R. Leitgeb, A. F. Fercher, and C. K. Hitzenberger. Speckle reduction in optical coherence tomography by frequency compounding. *Journal of Biomedical Optics*, 8(3):565–569, 2003.

[134] V. Polo, M. Satue, M. J. Rodrigo, S. Otin, R. Alarcia, M. P. Bambo, M. I. Fuertes, J. M. Larrosa, L. E. Pablo, and E. Garcia-Martin. Visual dysfunction and its correlation with retinal changes in patients with parkinson's disease: an observational cross-sectional study. *BMJ Open*, 6(5), 2016.

[135] G. Quellec, K. Lee, M. Dolejsi, M. K. Garvin, M. D. Abràmoff, and M. Sonka. Three-dimensional analysis of retinal layer texture: Identification of fluid-filled regions in SD-OCT of the macula. *IEEE Transactions on Medical Imaging*, 29(6):1321–1330, 2010.

[136] H. A. Quigley and A. T. Broman. The number of people with glaucoma worldwide in 2010 and 2020. *British journal of ophthalmology*, 90(3):262–267, 2006.

[137] R. Raftopoulos and A. Trip. The Application of Optical Coherence Tomography (OCT) in Neurological Disease. *Advances In Clinincal Neuroscience and Rehabilitation*, 12(2):30–33, 2012.

[138] R. M. Rangayyan, X. Zhu, F. J. Ayres, and A. L. Ells. Detection of the optic nerve head in fundus images of the retina with gabor filters and phase portrait analysis. *Journal of digital imaging*, 23(4):438–453, 2010.

[139] F. Rathke, S. Schmidt, and C. Schnörr. Probabilistic intra-retinal layer segmentation in 3-D OCT images using global shape regularization. *Medical Image Analysis*, 2014.

[140] L. A. Remington and D. Goodwin. *Clinical anatomy of the visual system E-Book*. Elsevier Health Sciences, 2011.

[141] T. Robertson. Extraction and classification of objects in multispectral images. *LARS Symposia*, 1973.

[142] S. Saidha, O. Al-Louzi, J. N. Ratchford, P. Bhargava, J. Oh, S. D. Newsome, J. L. Prince, D. Pham, S. Roy, P. Van Zijl, L. J. Balcer, E. M. Frohman, D. S. Reich, C. Crainiceanu, and P. A. Calabresi. Optical coherence tomography reflects brain atrophy in multiple sclerosis: A four-year study. *Annals of Neurology*, 78(5):801–813, 2015.

[143] P. J. Saine and M. E. Tyler. *Ophthalmic photography: retinal photography, angiography, and electronic imaging*, volume 132. Butterworth-Heinemann Boston, 2002.

[144] A. Salazar-Gonzalez, D. Kaba, Y. Li, and X. Liu. Segmentation of Blood Vessels and Optic Disc in Retinal Images. *IEEE Journal of Biomedical and Health Informatics*, 2194(c):1–1, 2014.

[145] H. M. Salinas and D. C. Fernandez. Comparison of PDE-based nonlinear diffusion approaches for image enhancement and denoising in optical coherence tomography. *IEEE Transactions on Medical Imaging*, 26(6):761–771, 2007.

[146] H. I. Salti, R. S. Antonios, S. S. Haddad, R. N. Hamam, Z. F. Bashshur, and N. G. Ghazi. Combined nonmydriatic spectral-domain optical coherence tomography and nonmydriatic fundus photography for the detection of age-related macular degeneration changes. *Ophthalmic Surgery, Lasers and Imaging Retina*, 46(5):531–537, 2015.

[147] J. S. Schuman. Spectral domain optical coherence tomography for glaucoma (an aos thesis). *Transactions of the American Ophthalmological Society*, 106:426, 2008.

[148] A. Seheult, D. Greig, and B. Porteous;. Exact Maximum A Posteriori Estimation For Binary Images. *Journal of the Royal Statistical Society*, Vol. 51(No. 2):271 –279, 1989.

[149] M. Shahidi, Z. Wang, and R. Zelkha. Quantitative thickness measurement of retinal layers imaged by optical coherence tomography. *American Journal of Ophthalmology*, 139(6), 2005.

[150] J. Shi and J. Malik. Normalized Cuts and Image Segmentation. *Ieee Transactions on Pattern Analysis and Machine Intelligence*, 22(8):888–905, 2000.

[151] Y. Shi and W. C. Karl. A fast level set method without solving pdes [image segmentation applications]. In *Proceedings. (ICASSP '05). IEEE International Conference on Acoustics, Speech, and Signal Processing, 2005.*, volume 2, pages ii/97–ii100 Vol. 2, March 2005.

[152] S. Srinivasan. Extracting structure from optical flow using the fast error search technique. *International Journal of Computer Vision*, 37(3):203–230, 2000.

[153] A. S. Suganya, R and Rajaram, S and Abdullah. *Big Data in Medical Image Processing*. CRC Press, 2018.

[154] Y.-C. Tham, X. Li, T. Y. Wong, H. A. Quigley, T. Aung, and C.-Y. Cheng. Global prevalence of glaucoma and projections of glaucoma burden through 2040: a systematic review and meta-analysis. *Ophthalmology*, 121(11):2081–2090, 2014.

[155] Y.-C. Tham, X. Li, T. Y. Wong, H. A. Quigley, T. Aung, and C.-Y. Cheng. Global prevalence of glaucoma and projections of glaucoma burden through 2040: A systematic review and meta-analysis. *Ophthalmology*, 121(11):2081 – 2090, 2014.

[156] J. Tian, B. Varga, G. M. Somfai, W. H. Lee, W. E. Smiddy, and D. C. DeBuc. Real-time automatic segmentation of optical coherence tomography volume data of the macular region. *PLoS ONE*, 10(8):1–20, 2015.

[157] H. R. Tizhoosh. Fuzzy Image Processing: Potentials and State of the Art. *International Conference on Soft Computing*, 1(February):321–324, 1998.

[158] H. R. Tizhoosh and M. Fochem. Fuzzy histogram hyperbolization for image enhancement. *Proceedings EUFIT*, 95(January 1995), 1995.

[159] H. R. Tizhoosh, G. Krell, and B. Michaelis. Locally adaptive fuzzy image enhancement. In *International Conference on Computational Intelligence*, pages 272–276. Springer, 1997.

[160] A. C. v. Trigt. *Dissertatio ophthalmologica inauguralis de speculo oculi*. PW van de Weijer, 1853.

[161] S. Vantigodi. Meanshift(), 2019, (Retrieved 19 December, 2019). `https://www.mathworks.com/matlabcentral/fileexchange/44401-meanshift`.

[162] U. Vision Express. Short and long sighted, 2019 (accessed June 1, 2019). `https://www.visionexpress.com/eye-health/eye-conditions/myopia-hypermetropia/`.

[163] C. Wang. *Level set segmentation of retinal structures*. PhD thesis, Brunel University London, 2016.

[164] C. Wang, D. Kaba, and Y. Li. Level set segmentation of optic discs from retinal images. *Journal of Medical Systems*, 4(3):213–220, 2015.

[165] C. Wang, Y. Wang, D. Kaba, Z. Wang, X. Liu, and Y. Li. Automated layer segmentation of 3d macular images using hybrid methods. In *Proc. International Conference on Image and Graphics. Tianjing, China.*, volume 9217, pages 614–628, 2015.

[166] C. Wang, Y. Wang, D. Kaba, Z. Wang, X. Liu, and Y. Li. Automated Layer Segmentation of 3D Macular Images Using Hybrid Methods. *Image and Graphics*, 9217:614–628, 2015.

[167] C. Wang, Y. Wang, D. Kaba, H. Zhu, Z. Wang, X. Liu, and Y. Li. Segmentation of intra-retinal layers in 3d optic nerve head images. In *Proc. International Conference on Image and Graphics. Tianjing.*, volume 9219, pages 321–332, 2015.

[168] C. Wang, Y. X. Wang, and Y. Li. Automatic choroidal layer segmentation using markov random field and level set method. *IEEE journal of biomedical and health informatics*, 21(6):1694–1702, 2017.

[169] Y.-H. Wang. Tutorial: Image segmentation. *National Taiwan University, Taipei*, pages 1–36, 2010.

[170] Z. Wang, M. Jenkins, G. Linderman, H. Bezerra, Y. Fujino, M. Costa, D. Wilson, and A. Rollins. 3-D Stent Detection in Intravascular OCT Using a Bayesian Network and Graph Search. *IEEE transactions on medical imaging*, 0062(c):1–14, 2015.

[171] M. Wertheimer. Laws of organization in perceptual forms. *A source book of Gestalt psychology*, (1923), 1938.

[172] World Health Organisation. Prevention of blindness and visual impairment report, 2010, (assessed October 12 2015). `http://www.who.int/blindness/causes/priority/en/`.

[173] R. T. Yanagihara, C. S. Lee, D. S. W. Ting, and A. Y. Lee. Methodological challenges of deep learning in optical coherence tomography for retinal diseases: a review. *Translational Vision Science & Technology*, 9(2):11–11, 2020.

[174] A. Yazdanpanah, G. Hamarneh, B. Smith, and M. Sarunic. Intra-retinal layer segmentation in optical coherence tomography using an active contour approach. *Medical Image Computing and Computer-Assisted Intervention*, 12(Pt 2):649–656, 2009.

[175] A. Yazdanpanah, G. Hamarneh, B. R. Smith, and M. V. Sarunic. Segmentation of intra-retinal layers from optical coherence tomography images using an active contour approach. *IEEE Transactions on Medical Imaging*, 30:484–496, 2011.

[176] L. Yeung, V. C. Lima, P. Garcia, G. Landa, and R. B. Rosen. Correlation between spectral domain optical coherence tomography findings and fluorescein angiography patterns in diabetic macular edema. *Ophthalmology*, 116(6):1158–1167, 2009.

[177] F. Yi and I. Moon. Image segmentation: A survey of graph-cut methods. In *2012 International Conference on Systems and Informatics (ICSAI2012)*, pages 1936–1941. IEEE, 2012.

[178] A. P. Yow, D. Wong, H. Liu, H. Zhu, I. J. Ong, A. Laude, and T. H. Lim. Automatic visual impairment detection system for age-related eye diseases through gaze analysis.

In *2017 39th Annual International Conference of the IEEE Engineering in Medicine and Biology Society (EMBC)*, pages 2450–2453, July 2017.

[179] J. Yuan, E. Bae, X.-C. Tai, and Y. Boykov. A study on continuous max- flow and min-cut approaches. *2010 IEEE Conference*, 7:2217–2224, 2010.

[180] N. M. Zaitoun and M. J. Aqel. Survey on Image Segmentation Techniques. In *Procedia Computer Science*, 2015.

[181] M. Zetterberg. Age-related eye disease and gender. *Maturitas*, 83:19 – 26, 2016.

[182] L. Zhang, W. Zhu, F. Shi, H. Chen, and X. Chen. Automated Segmentation Of Intraretinal Cystoid Macular Edema For Retinal 3D OCT Images With Macular Hole School of Electronics and Information Engineering , Soochow University , Suzhou , China Joint Shantou International Eye Center , Shantou University an. *IEEE*, pages 1494–1497, 2015.

[183] T. Zhang, Z. Song, X. Wang, H. Zheng, F. Jia, J. Wu, G. Li, and Q. Hu. Fast retinal layer segmentation of spectral domain optical coherence tomography images. *Journal of Biomedical Optics*, 20(9):096014, 2015.